

Thermomechanical characterization of advanced ceramic breeder beds for fusion blankets

Zur Erlangung des akademischen Grades
Doktor der Ingenieurwissenschaften
der KIT-Fakultät für Maschinenbau
Karlsruher Institut für Technologie (KIT)

genehmigte

Dissertation

von

Ing. Simone Pupleschi

Tag der mündlichen Prüfung: 13 Dezember 2017

Hauptreferent: Prof. Dr.-Ing. Marc Kamlah
Karlsruher Institut für Technologie (KIT)

Korreferent: Prof. Dr.-Ing. Robert Stieglitz
Karlsruher Institut für Technologie (KIT)

Disclaimer

Parts of this work have been carried out within the framework of the EUROfusion Consortium and have received funding from the Euratom research and training programme 2014-2018 under grant agreement No 633053. Other Parts were supported by Fusion for Energy under the Specific Grant Agreement F4E-FPA-380-A3: SG01. The views and opinions expressed herein do not necessarily reflect those of the European Commission or Fusion for Energy. Fusion for Energy is not liable for any use that may be made of the information contained herein.

Abstract

A tritium Breeding Blanket (BB), ensuring tritium breeding self-sufficiency, is a compulsory component for the demonstration power reactor (DEMO), the next-step after ITER (International Thermonuclear Experimental Reactor [1]). Six mock-ups of so called Test Blanket Modules (TBMs), will be tested in ITER in order to test six different breeding blanket concepts. ITER will provide the first experimental data on the performance of the BBs.

Presently, two European tritium breeder concepts (solid breeder blanket and liquid metal breeding blanket) are considered to be tested in ITER. In the solid breeder blanket concept, the ceramic breeding material (lithium orthosilicate) and the neutron multiplier (beryllium) are in the form of packed pebble beds. A thorough understanding of the thermal and mechanical properties of the ceramic pebble beds under fusion relevant conditions is essential for the design of the breeder blanket modules of future fusion reactors. Even if the ceramic beds have no structural function, the beds have to withstand stresses induced by the blanket operating conditions. A blanket module will experience a cyclic loading due to the burn pulses of the plasma, temperature gradients and the mismatch of the thermal expansion coefficients between the beds and the structural materials result in cyclic compressive load acting on the breeder beds. Due to their granular nature, pebble bed materials show a dependence of thermal conductivity on the mechanical state (packing factor, stress/strain state) as well as the filling gas type and pressure.

The current European reference breeding material consists of a two-phase material fabricated by the melt-spraying method. The two phases are lithium orthosilicate and lithium metasilicate, respectively. This material is well characterized, however, due to process related defects of the pebbles the rupture strength gives cause for some concerns. To improve the mechanical performances, a new, but also melt-based production facility has been put into operation at KIT for the production of Advanced Ceramic Breeder (ACB) pebbles. By the introduction of lithium metatitanate as a second phase instead of lithium metasilicate the mechanical stability of lithium orthosilicate pebbles is further enhanced.

This doctoral thesis work consists in both experimental and numerical characterization of the thermal and mechanical properties of ACB ceramic pebble beds under fusion relevant

conditions. An experimental set-up based on the transient Hot Wire Method has been designed. The influence of temperature, compressive load and filling gas type/pressure on the effective thermal conductivity of pebble beds is investigated. The influence of the chemical composition (lithium metatitanate content) is examined as well. Uniaxial compression experiments are conducted along with Discrete Element Method numerical simulations to investigate the influence of cyclic loading on the macro and micro mechanical behaviour of packed beds.

Kurzfassung

Ein Tritium-Brutblanket (BB) ist ein unverzichtbares Bauteil für den Fusionsdemonstrationsreaktor (DEMO), um die Selbstversorgung des Reaktors mit erbrüetem Tritium sicherzustellen. DEMO stellt die nächste Entwicklungsstufe nach ITER (Internationaler Thermonuklearer Experimenteller Reaktor [1]) dar. In ITER sollen sechs Modelle der sogenannten Testblanketmodule (TBMs) getestet werden, um sechs unterschiedliche Brutblanketkonzepte zu erproben. ITER wird erste experimentelle Daten zur Durchführbarkeit der BBs liefern.

Gegenwärtig werden zwei europäische Tritium-Brutkonzepte (Feststoff-Brutblanket und Flüssigmetall-Brutblanket) für einen Test in ITER in Betracht gezogen. Im Feststoff-Brutblanket liegen das keramische Brutmaterial (Lithiumorthosilikat) und der Neutronenvervielfacher (Beryllium) in Form von dicht gepackten Kugelschüttbetten vor. Eine umfassende Kenntnis der thermischen und mechanischen Eigenschaften keramischer Kugelschüttbetten unter fusionsrelevanten Bedingungen ist wesentlich für die Konzeption der Brutblanketmodule zukünftiger Fusionsreaktoren. Auch wenn die Keramiksüttbetten keine strukturtragende Funktion haben, so müssen sie doch den mechanischen Spannungen, die beim Betrieb des Blankets entstehen, standhalten können. Ein Blanketmodul wird einer zyklischen Belastung durch die Brennphasen des Plasmas ausgesetzt sein. Temperaturgradienten und die unterschiedlichen thermischen Ausdehnungskoeffizienten der Kugelschüttbetten und der Strukturmaterialien führen zu einer zyklischen Druckbelastung, welche auf die Schüttbetten einwirkt. Aufgrund der granularen Natur der Kugelschüttbetten, zeigt das einsetzte Material eine Abhängigkeit der thermischen Leitfähigkeit vom mechanischen Zustand (Packungsfactor, Spannungs-/Verformungszustand) sowie von der Art des Füllgases und seinem Druck.

Das europäische Referenzbrutmaterial besteht derzeit aus einem, mittels eines Schmelzsprühverfahrens hergestellten, zweiphasigen Material. Bei den zwei Phasen handelt es sich um Lithiumorthosilikat und Lithiummetasilikat. Dieses Material wurde bereits gut charakterisiert. Allerdings gibt es angesichts der prozessinduzierten Defekte der Kugeln Bedenken hinsichtlich deren Bruchfestigkeit. Um die mechanischen Eigenschaften zu verbessern, wurde am KIT eine neue Anlage für die ebenfalls schmelzbasierte Produktion von

fortschrittlichen keramischen Brutkeramikkugeln (“Advanced Ceramic Breeder” (ACB)) entwickelt und in Betrieb genommen. Durch den Einsatz von Lithiummetatitanat als Zweitphase anstelle von Lithiummetasilikat wird die mechanische Stabilität der Lithiumorthosilikatkugeln verbessert.

Die vorliegende Dissertation befasst sich sowohl mit der experimentellen als auch mit der numerischen Charakterisierung der thermischen und mechanischen Eigenschaften von Kugelschüttbetten aus ACB-Keramiken unter fusionsrelevanten Bedingungen. Dazu wurde auf der Grundlage des transienten Heißdraht-Verfahrens (Hot Wire Method) eine Versuchsanordnung konzipiert. Mit dieser wird der Einfluss der Temperatur, mechanischer Kompressionsbelastung, sowie der Art und des Drucks des Füllgases auf die effektive thermische Leitfähigkeit der Kugelschüttbetten untersucht. Auch der Einfluss der chemischen Zusammensetzung (Gehalt an Lithiummetatitanat) wird untersucht. Uniaxiale Druckexperimente werden zusammen mit numerischen Simulationen mittels der Diskrete-Elemente-Methode (DEM) durchgeführt, um den Einfluss von zyklischer Belastung auf das makro- und mikromechanische Verhalten der Schüttbetten zu untersuchen.

Table of Contents

Abstract	i
Kurzfassung	iii
Abbreviations	vii
Symbols	viii
Chapter 1	
Introduction	1
1.1 General overview on fusion technology and breeding blanket.....	1
1.2 Ceramic breeder materials, requirements and fabrication options	6
1.3 Motivation	9
Chapter 2	
Overview of the parameters affecting the thermomechanical behaviour of packed beds.....	13
2.1 Physical and mechanical parameters characterizing a packed bed.....	13
2.2 Heat transfer in packed beds.....	15
Chapter 3	
Thermal conductivity measurement methods and present know how on breeder beds thermomechanics.....	21
3.1 Methods for the measurement of thermal conductivity.....	21
3.1.1 <i>Steady state methods</i>	21
3.1.1.1 Comparative cut bar	22
3.1.1.2 Heat flow meter technique.....	23
3.1.1.3 Guarded hot plate technique	23
3.1.1.4 Radial Heat Flow Method	23
3.1.2 <i>Transient methods</i>	25
3.1.2.1 Flash Diffusivity Method	25
3.1.2.2 Hot wire and probe methods.....	26
3.2 Related work.....	28
3.2.1 <i>Thermal conductivity of breeder beds</i>	28
3.2.2 <i>Thermomechanical behaviour of breeder beds</i>	36

Chapter 4	
Experimental set-up to measure the thermal conductivity of ceramic pebble beds	41
4.1 Apparatus and experimental procedure	41
4.1.1 Probe design and sample size justification	46
4.1.2 Evaluation of the uncertainty	52
4.1.3 Probe calibration	54
Chapter 5	
Results on the effective thermal conductivity of ceramic breeder pebble beds	57
5.1 Investigated materials and experimental conditions	57
5.2 Experimental results and discussion	61
5.3 Summary	70
Chapter 6	
Validation study of cyclic behaviour of pebble beds	73
6.1 Numerical model and boundary conditions	73
6.2 Numerical results and Discussion	75
6.3 Summary	81
Chapter 7	
Experimental and numerical study of cyclic behaviour of ceramic pebble beds	83
7.1 Experimental	83
7.2 Numerical experiments	86
7.3 Results and Discussion	87
7.3.1 Macro scale response	88
7.3.2 Particle-scale response	91
7.4 Summary	98
Chapter 8	
Conclusions	101
References	105
Appendix A	113
Appendix B	114
Appendix C	118
Appendix D	119
Appendix E	120
Acknowledgements	121

Abbreviations

ACB	<i>Advanced Ceramic Breeder</i>
BB	<i>Breeder Blanket</i>
CDF	<i>Cumulative Distribution Function</i>
CN	<i>Coordination Number</i>
DEM	<i>Discrete Element Method</i>
DEMO	<i>Demonstration Power Reactor</i>
D-T	<i>Deuterium-Tritium</i>
EU Ref.	<i>EU reference</i>
FE	<i>Finite Element</i>
FEM	<i>Finite Element Method</i>
HCLL	<i>Helium Cooled Lithium Lead</i>
HCPB	<i>Helium Cooled Pebble Bed</i>
HM	<i>Hall and Martin correlation</i>
HTC	<i>Heat Transfer Coefficient</i>
HWM	<i>Hot Wire Method</i>
ITER	<i>International Thermonuclear Experimental Reactor</i>
KIT	<i>Karlsruhe Institute of Technology</i>
LMT	<i>Li₂TiO₃ (lithium metatitanate)</i>
LVDT	<i>Linear Variable Displacement Transducers</i>
PBC	<i>Periodic Boundary Condition</i>
PDF	<i>Probability Distribution Function</i>
PF	<i>Packing Factor</i>
RCP	<i>Random Close Packing</i>
RT	<i>Room Temperature</i>
SBZ	<i>Schunder, Bauer, Zehner correlation</i>
TBM	<i>Test Blanket Modules</i>
UCLA	<i>University of California Los Angeles</i>
UCT	<i>Uniaxial Compression Test</i>
TZ	<i>Ytria-stabilized Zirconia</i>

Symbols

Roman letters

A_{he}	[mm ²]	<i>Cross section area of the heated wire</i>
C		<i>Goodman's constant</i>
CN		<i>Coordination number</i>
c_p	[J/(Kg K)]	<i>Specific heat at constant pressure</i>
D	[m]	<i>Measuring cell diameter</i>
d	[m]	<i>Gap dimension</i>
d	[mm]	<i>Pebble diameter</i>
d_m	[m]	<i>Molecule diameter</i>
d_p	[m]	<i>Diameter of the probe</i>
$d_{pist.}$	[m]	<i>Displacement of the piston</i>
E	[MPa]	<i>Elastic modulus</i>
E_i		<i>Exponential integral</i>
H	[m]	<i>Bed height</i>
I	[A]	<i>Current</i>
K_n		<i>Knudsen number</i>
K^*		<i>Coverage factor</i>
\mathcal{K}	[J/K]	<i>Boltzmann constant</i>
k	[W/(m K)]	<i>Thermal conductivity</i>
k_g	[W/(m K)]	<i>Gas thermal conductivity</i>
k_s	[W/(m K)]	<i>Solid thermal conductivity</i>
k_0	[W/(m K)]	<i>Thermal conductivity of non-confined gas</i>
l_{he}	[m]	<i>Length of the heating element</i>
L_p	[m]	<i>Length of the probe</i>
m_g	[gr/mol]	<i>Atomic mass of the gas</i>
m_{pb}	[Kg]	<i>Packed bed mass</i>
m_r		<i>Ratio of the gas (m_g) to solid (m_s) atomic masses</i>

m_s	[gr/mol]	<i>Atomic mass of the solid material</i>
N		<i>Number of observations</i>
N_c		<i>Number of contacts in the assembly</i>
N_p		<i>Number of particles in the assembly</i>
P_r		<i>Prandtl number</i>
p_g	[Pa]	<i>Gas pressure</i>
Q	[W]	<i>Power</i>
q'	[W/m]	<i>Power per unit length of heater</i>
\vec{q}	[W/m ²]	<i>Heat flux</i>
q_x	[W/m ²]	<i>Heat flux along x</i>
R	[Ω/m]	<i>Characteristic resistance of the wire</i>
r	[m]	<i>Radius</i>
r_p	[m]	<i>Radius of the probe</i>
S_{10}	[1/K]	<i>Slope of the linear region of the temperature transient</i>
T	[K] or [°C]	<i>Temperature</i>
T_b	[°C]	<i>Boundary temperature</i>
T_{exp}	[°C]	<i>Experimental temperature</i>
t	[s]	<i>Time</i>
t_h	[s]	<i>Heating time</i>
u_i		<i>Standard uncertainty of the parameter i</i>
V	[V]	<i>Voltage</i>
V_{pb}	[m ³]	<i>Packed bed volume</i>

Greek letters

α	[m ² /s]	<i>Thermal diffusivity</i>
α_c		<i>Thermal accommodation coefficient</i>
β		<i>Gas constant in Kaganer's model</i>
γ		<i>Euler's constant</i>
δ		<i>Specific heat capacity ratio</i>
ε	[%]	<i>Strain</i>
ε_r	[%]	<i>Residual strain after unloading</i>

λ	[m]	<i>Mean free path</i>
μ	[N/s m ²]	<i>Dynamic viscosity</i>
μ_f		<i>Friction coefficient</i>
ν		<i>Poisson's ratio</i>
ρ	[Kg/m ³]	<i>Density</i>
ρ_{he}	[$\Omega/\text{mm}^2 \text{ m}$]	<i>Resistivity of the heating wire</i>
ρ_p	[Kg/m ³]	<i>Pebble density</i>
ρ_{pb}	[Kg/m ³]	<i>Pebble bed density</i>
σ_z	[MPa]	<i>Stress along z</i>

Chapter 1

Introduction

In this chapter a general overview about fusion technology, the breeding blanket and the breeding material is given, the motivation of this work is then introduced.

1.1 General overview on fusion technology and breeding blanket

In a fusion reaction, energy is released when two light atomic nuclei fuse into a heavier one. The energy arising from nuclear fusion is the difference between the binding energies of the initial nuclides and the fusion products. The difference, in mass, is equivalent to the energy released according to $E = m c^2$.

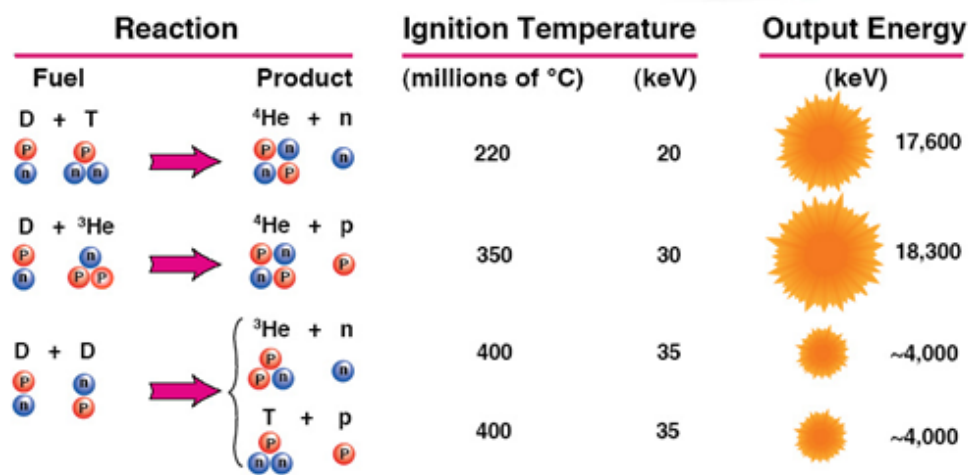
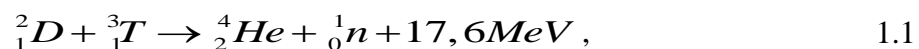


Figure 1-1: Ignition Temperatures and Output Energies of fusion reactions. Reproduced from [2].

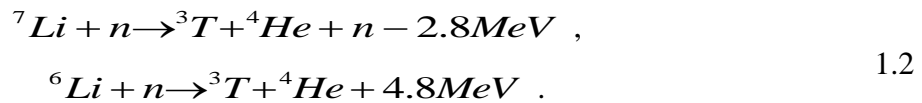
The nuclei need an extremely high kinetic energy to overcome the energy barrier (repelling electrostatic forces, Coulomb forces) to allow the fusion reaction. In Figure 1-1 the ignition temperatures and the output energies for some fusion reactions are reported [2]. The deuterium-tritium (D-T) fusion reaction is considered to be the most promising, having the highest reaction rate and the lowest ignition temperature.

This D-T fusion reaction reads to:



in which deuterium and tritium nuclei fuse together releasing energy. The reaction yields 17.6 MeV of energy; 80% of the out coming energy is carried by the neutron (14 MeV), the remaining 20% (3.5MeV) is carried by He⁴. Deuterium is a stable isotope of hydrogen and it is commonly available. Deuterium can be extracted from water as in every litre of seawater there are 33 milligrams of deuterium. On the other hand, tritium is a radioactive isotope of hydrogen which occurs in negligible quantities in nature, because of its relatively short half-life. However, tritium can be produced or “bred” by the interaction of the neutron, resulting from the D-T reaction and a lithium atom contained in the breeding blanket surrounding the plasma.

Natural lithium is composed of two stable isotopes, ⁶Li and ⁷Li, where the latter one is the more abundant (about 92.5 percent of the atoms). When lithium is subjected to a neutron flux, tritium is produced according to the reactions



In Figure 1-2 the reaction’ cross sections for the above reactions are reported [3]. As shown in the figure, the reaction involving ⁷Li is a threshold reaction only taking place if the incident neutron energy exceeds 6 MeV.

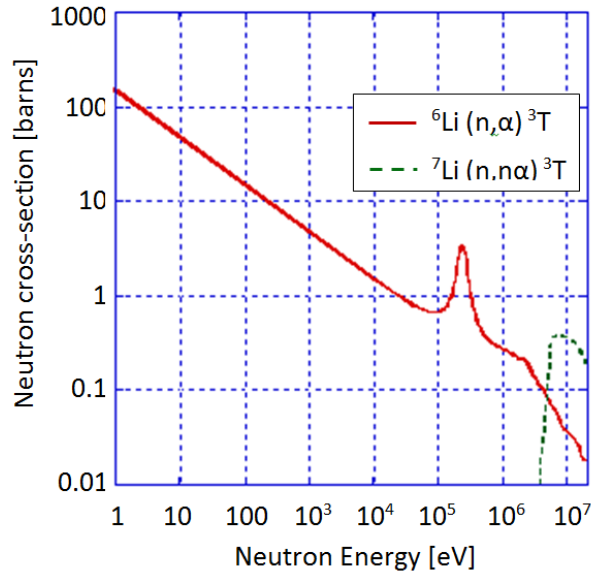


Figure 1-2: ⁶Li and ⁷Li reaction cross sections. After [3].

Not all neutrons coming out from the plasma react with lithium; neutrons can be absorbed by undesired absorption reactions or can pass through the breeding zone without interactions. The

TBR is the ratio between the tritium nuclei generated in the blanket and the tritium nuclei burned in the plasma. In order to assure a Tritium Breeding Ratio, $TBR > 1$ a neutron multiplier material must be used. A neutron multiplier material releases more neutrons than it absorbs as result of the nuclear reaction $(n, 2n)$. A neutron interaction with a neutron multiplier nuclide results in emission of two neutrons. Beryllium and lead show this property.

At the temperatures necessary to realize fusion, the fuel is in the state of plasma. Plasma is an electrically neutral hot ionized gas, where the electrons are completely loose from the positive nucleus. Three heating techniques can be used to heat up the plasma: ohmic heating, neutral beam injection and radiofrequency heating. Furthermore, the helium produced by the fusion reactions slows down inside the plasma heating up the plasma itself. This effect is called self-heating. If this contribution becomes equal to the energy lost by the plasma, the external heating is no longer necessary and the plasma is self-sustaining. This state is called ignition.

The plasma can be effectively confined by a torus shaped magnetic field in a toroidal vacuum chamber. In order to compensate the particle drifts the magnetic field lines have to be twisted around the torus. In this way the charged particles are forced on helical paths around the magnetic field lines. This contrasts the drifting effect leading to an effective plasma confinement. Methods used to produce the twisted field lines have given rise to two types of toroidal fusion machines:

- Stellarator
- Tokamak

An example of a stellarator, the Wendelstein 7-X (IPP Greifswald) [4], is shown in Figure 1-3. In this concept, the twisted magnetic field is produced by twisted coils surrounding the vacuum vessel.

Figure 1-4 shows a basic scheme of a tokamak [4]. In the tokamak concept the combination of a toroidal field, produced by the toroidal magnets surrounding the vacuum vessel, and a poloidal field generated by inducing a current in the plasma by the central coil (the plasma ring is the secondary winding), result in the desired helically twisted magnetic field lines.

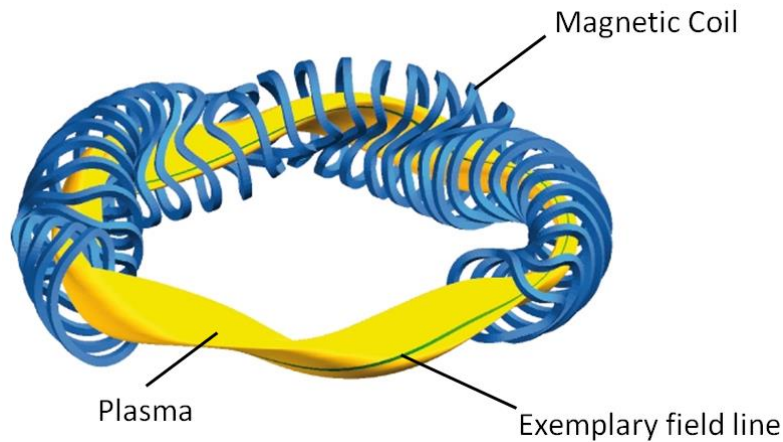


Figure 1-3: Wendelstein 7-X: Schematic representation of the shape of the plasma (yellow) with the course of one (exemplary) magnetic field lines on the plasma surface (green) and the required arrangement of the magnet coil system (blue). After [4].

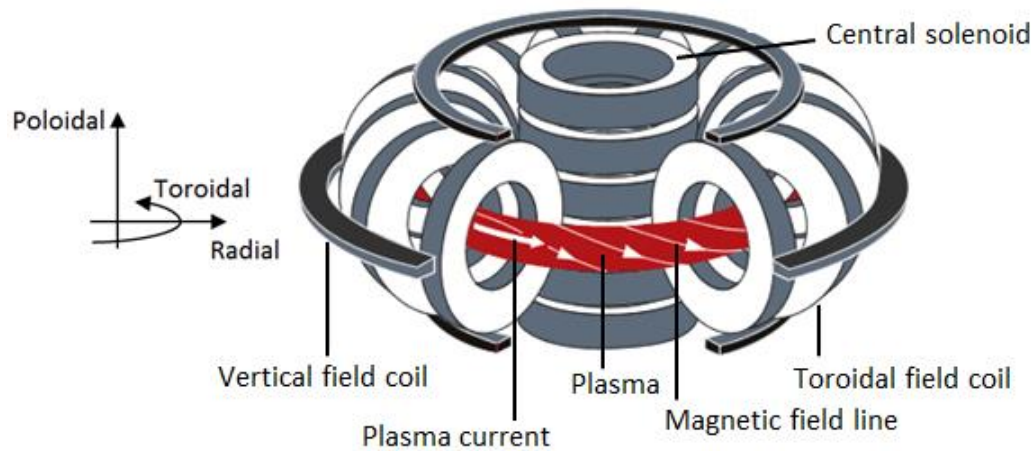


Figure 1-4: Schematic representation of a toroidal confinement fusion reactor (tokamak) [4].

The breeding blanket is one of the key components of a future fusion reactor facing the plasma. ITER will provide a unique opportunity to test mock-ups of breeding blankets, called Test Blanket Modules (TBM), in a real fusion environment. Within these test blankets, several concepts for ensuring tritium breeding self-sufficiency will be explored. The breeding blanket works as main thermal power conversion system. As it is the first component facing the plasma, it has to sustain high heat fluxes and to encompass three functions:

- to remove thermal energy from the plasma (surface heat flux, volumetric heating in blanket by neutrons bremsstrahlung) during normal and off-normal operational conditions,
- to breed tritium fuel,
- to contribute to the radioactive shielding of sensitive components.

Different Breeding blanket concepts have been developed in EU, Japan, China, Korea and India proposing different solutions for the conceptual design of the blanket of the future DEMO device [5]. In order to encompass the three major functions all breeding blankets concepts share the same basic radial design. Figure 1-5 shows a schematic arrangement of the components composing a blanket in the radial direction [3]. Starting from the plasma and moving in the radial direction the first blanket's component is an actively cooled first wall, whose main role is to remove the heat flux emitted by the plasma (heat radiation, bremsstrahlung). Behind the first wall the breeding zone is located, where most of the neutronic power is deposited as volumetric heat source and where the breeder/neutron multiplier materials are located. The breeding zone can either be actively cooled or, as in some liquid breeder concepts, the liquid breeder can be used as coolant itself. Finally, a shield is radially terminating the blanket towards the vacuum vessel.

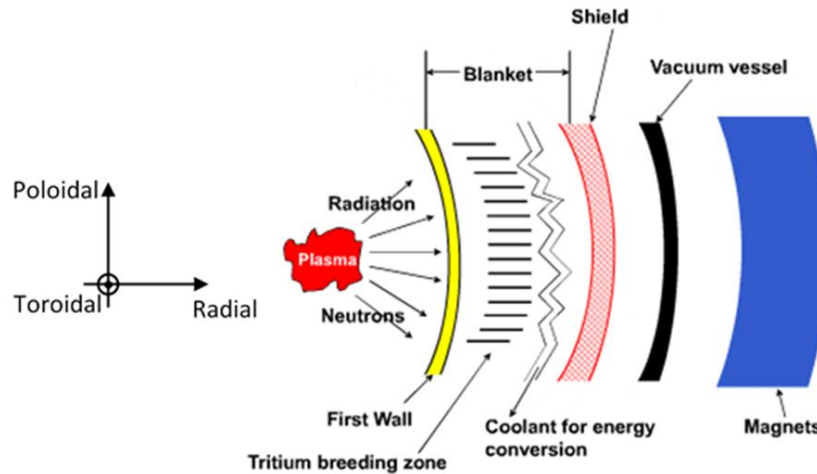


Figure 1-5: Main components of the Breeding Blanket. Reproduced from [3].

Different design solutions have been proposed for the breeding blanket using various combinations of breeder, neutron multiplier materials, coolants and structural materials. Two breeder blanket concepts are developed in Europe: the Helium Cooled Lithium Lead (HCLL) concept and the Helium Cooled Pebble Bed (HCPB) concept. In the HCLL concept the eutectic Pb-15.7 Li (90% enriched in ${}^6\text{Li}$) acts as tritium breeder material and neutron multiplier. In the HCPB concept the ceramic breeding material (lithium orthosilicate) and the neutron multiplier (beryllium) are separately arranged in the form of packed pebble beds. The heat-loaded structures are actively cooled a pressurized inert gas (helium at 80 bar).

1.2 Ceramic breeder materials, requirements and fabrication options

The choice of the tritium breeder material used in the blanket is fundamental for a fusion reactor since in it both tritium and heat are generated. In the fusion environment the breeder material is subjected to severe conditions such as neutron irradiation, high temperatures, cyclic mechanical compression and high thermal flux. Lithium-based ceramics compounds have been recognized as promising breeding materials for the solid breeder blanket concepts. Lithium compounds were identified in the first place based on the physical, chemical and activation properties. Lithium oxide (Li_2O) and ternary compounds including lithium orthosilicate (Li_4SiO_4), lithium metazirconate (Li_2ZrO_3), lithium metatitanate (Li_2TiO_3) and lithium aluminates (LiAlO_2) were identified as promising candidates [6]-[7]. A first selection was done after an initial extensive characterization of the candidate materials, which pointed out the strengths and the weaknesses of each material. Li_2O , Li_2ZrO_3 and LiAlO_2 became less attractive, mainly because of excessive swelling/creep, activation, modest tritium release and low lithium density, respectively. The R&D on ceramic breeder materials is still ongoing among the ITER members [8]-[9]. The research is mainly focussed on Li_2TiO_3 and Li_4SiO_4 . Li_2TiO_3 is the present reference material in Japan, Korea and India, while Li_4SiO_4 has been selected as reference material in Europe and China.

The early proposals for the breeder material shapes were either sintered pellets or blocks. However, swelling and fragmentation due to the irradiation and the thermal stresses were cause of concerns. In order to sustain the severe conditions of the breeding zone, breeder pebble beds were then proposed. The breeder beds consist of nearly spherical ceramic particles, with diameters of about 1 mm or smaller, packed in the breeding zone of the blanket. The small size of the particles composing the bed assures an intrinsic resistance to thermal loads. Due to their small diameter, resulting in a large surface area to volume ratio, the thermal stress inside the particles arising from the neutronic heat generation is negligible. Even for a highly densified bed, a purge gas flowing between pebbles can recover the generated tritium. Other advantages related to the use of breeder beds include the possibility to fill complex geometries and the mitigation of swelling and expansion thanks to rearrangement of the particles. Moreover, the parameters of the bed such as the packing factor, the pebble material, the size distribution, the filling gas type and pressure can be tailored to obtain the optimal thermomechanical properties. The main requirements for the breeder beds are:

- *Tritium generation and release.* The primary task of the breeder beds is to generate tritium and release it in an efficient way. A high intrinsic lithium density accompanied by a low tritium residence time is highly desired in order to minimize the tritium inventory stored in the blanket (safety issue) and to readily extract the fuel to sustain the fusion reaction.
- *Adequate mechanical properties.* In the breeder blanket the ceramic beds have no structural function; however they have to withstand the stresses due to the operational conditions of the blanket without excessive fragmentation. A high pebble crush load is desired to sustain the operational conditions. An excessive pebble fragmentation could result in a change of the effective bed properties, in an increase of the purge gas pressure drop and, in the extreme case, in the blockage of the purge gas flow (major safety issue).
- *Adequate thermal properties.* The thermal properties of the breeder beds are of primary importance for the design of the breeder zone of the blanket. The operational temperatures of the breeding zone depend on the heat transfer parameters of the bed such as the effective thermal conductivity and the heat transfer coefficient at the pebble bed/wall interface. Moreover, the tritium release strongly depends on the breeder material temperature. A low temperature of the breeder material result in a poor tritium release rate leading to a high tritium inventory in the breeding zone of the blanket (safety issue).
- *Compatibility with the structural materials.* The possible corrosion layer formed as a consequence of the contact (at high temperatures $300\text{ °C} < T < 550\text{ °C}$) between the breeder material and the metallic structure can affect the structural integrity and the tritium permeation as well as the heat transfer.
- *Stability.* Chemical and microstructural long-term stability of the ceramic compound in the expected operating temperature range ($300\text{ °C} < T < 920\text{ °C}$).
- *Neutron irradiation resistance.* The neutron irradiation should not result in an excessive degradation of the material properties.
- *Economic and efficient production.* Considering the necessity of the expensive ${}^6\text{Li}$ enrichment, the fabrication process should be cost effective with a high yield. The fabrication process should also be suitable for an easy recycling of the used pebbles.
- *Low activation properties.* A low activation characteristic of the ceramic compound including the impurities introduced from the raw materials or the fabrication process is desired to achieve a short recycling time.

In the literature numerous methods for the fabrication of tritium breeding pebbles are described, most of them are based on powder technological or wet-chemical routes. In the EU melt-based processes are favoured as they offer an easy recycling of used pebbles [10]-[11]. The current European reference breeding material consists of a two-phase material fabricated by the melt-spraying method [12]. A schematic representation of the process is given in Figure 1-6 left. The raw materials (lithium hydroxide and silica) are heated up in a platinum crucible above the melting temperature. The formed melt, driven by gravity, flows through the outlet pipe forming a melt jet which is sprayed with an air stream originating small melt droplets that solidify during the flight. The obtained material consists of about 90 mol% lithium orthosilicate (Li_4SiO_4) and 10 mol% lithium metasilicate (Li_2SiO_3) [10]. The melt-spraying process is economic and capable to generate pebbles suitable for the blanket use. However, it has low a yield (50%) and the pebble quality gives cause for some concerns [13]. Due to the fabrication process these pebbles exhibit pores (because of air inclusions) that influence rupture strength, while the low yield is related to the rough control of the pebble size distribution.

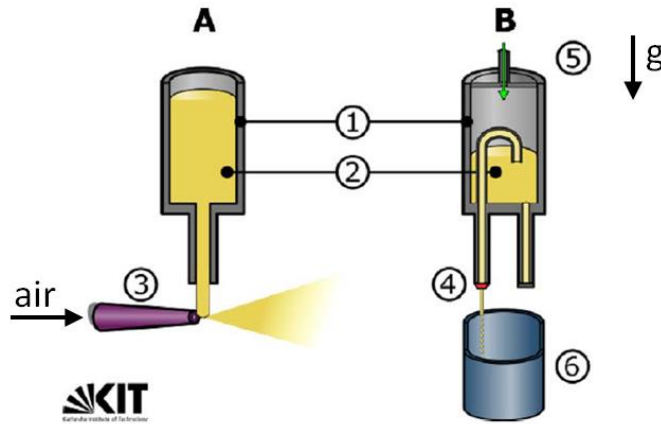


Figure 1-6: Schematic representation of the (A) melt-spraying and (B) melt-based methods with ① platinum crucible, ② melt, ③ spray, ④ nozzle, ⑤ applied pressure, ⑥ pebble container. After [14].

To improve the mechanical performances by reducing the process related defects, a new experimental facility based on a melt-based method was put into operation at KIT for the production of Advanced Ceramic Breeder (ACB) pebbles [14], Figure 1-6 right. In this process the raw materials are heated up in a platinum crucible. When the melt is formed the crucible is slightly pressurized by synthetic air forcing the melt through a nozzle with a fixed diameter. The melt jet breaks into small droplets thanks to the Plateau-Rayleigh instability; the formed droplets are cooled down during their flight and then collected. The melt-based process allows a better

control of the pebble size as well as a better pebble quality resulting in a higher yield and greater crush load, respectively. To further enhance the mechanical properties, lithium metatitanate (Li_2TiO_3) was introduced as a second phase [15]. With the introduction of Li_2TiO_3 the crush load was further enhanced [15].

1.3 Motivation

Lithium-based ceramics, in the form of packed pebble beds, are selected as tritium breeder in the solid breeder blanket concepts. In the fusion environment the breeder beds are subjected to severe conditions such as neutron irradiation, high temperatures, cyclic mechanical compression and high thermal flux. Pebble beds show a rather complex thermomechanical behaviour due to the discrete nature of the individual pebbles. Moreover, a pebble bed consists of a solid phase and a gas phase (purge gas) that fills the voids between pebbles. For that reason, the effective thermal properties of a packed bed depend on the thermal conductivities of the constituent phases. Both tritium release and heat recovery depend on the thermal performances of the breeding zone which in turn are closely related to the mechanical state as well as to the filling gas type and pressure.

The present European reference breeding material consists of a two-phase material of 90 mol% lithium orthosilicate and 10 mol% lithium metasilicate fabricated by the melt-spraying method. Advanced Ceramic Breeder (ACB) pebbles with lithium metatitanate as a second phase and fabricated by a melt-based method, were proposed as an alternative.

Even if the ceramic beds have no structural function, the beds have to withstand stresses induced by the blanket operating conditions. The qualification of the ACB material for blanket application is required to demonstrate acceptable performances at fusion relevant conditions. This also includes the characterization of the thermomechanical behaviour of the ACB ceramic. The effective mechanical and thermal properties of a granular bed, even directly related to the properties of the base material, cannot be derived from the properties of a single pebble. Therefore, the characterization of single pebble as well as of pebble beds is of primary importance for the understanding of the pebble bed thermo-mechanics. Laboratory testing has been extensively used to characterize the macroscopic response of ceramic breeder beds. However, laboratory investigations alone cannot produce a full insight into the complex thermomechanical behaviour of the packed pebble beds since the micro scale response of the

granular assembly is not experimentally accessible. Discrete Element Method (DEM) simulations can bridge the gap to understand the macroscopic behaviour from the micro response at the pebble scale.

The aim of this work is the characterization of the thermal properties and mechanical response of ACB ceramic pebble beds under fusion relevant conditions.

Regarding the characterization of the thermal properties, the general goal is the investigation of the effective thermal conductivity of ACB pebble beds at blanket relevant conditions. To this end an experimental facility has to be developed for the investigation of ceramic pebble beds' thermal conductivity as a function of temperature, chemical composition, compressive load, as well as filling gas type and pressure. The first specific objective is the derivation of correlations, to be used for the thermal design of the breeder zone of the blanket, namely for the calculation of the effective thermal conductivity of the European advanced and reference pebble beds as a function of temperature for different gas pressures. Since the ACB composition (i.e. metatitanate content) influences the effective thermal conductivity, the second specific objective is the identification of the optimal composition based on the results of the experimental campaign. The reduction of the purge gas pressure is beneficial for the reduction of the tritium permeation in the coolant. On the other hand, the reduction of the purge gas pressure could also reduce the effective thermal conductivity of the breeder bed. In view of this, the third specific objective is the identification of a minimum purge gas pressure. Besides, the fourth and last specific objective is to enhance the knowledge of the influence of the filling gas type in relation to the pebble size on the effective thermal conductivity of the breeder bed. This is achieved by both an experimental and a theoretical approach.

Regarding the characterization of the mechanical response of breeder beds, the general goal is to study the response of bed assemblies subjected to cyclic compression and to characterize the evolution of macro and micro mechanical parameters as the cycling loading proceeds. The first specific objective is the quantification and characterization of the progressive bed compaction due to cyclic loading and the influence of bed height, pebble material, pebble size, pebble size distribution and maximum compressive load. To this end, experiments and numerical simulations are conducted. Besides, this lead to the second specific objective, namely the validation of the KIT-DEM code by means of the comparison with experimental results. The third specific

objective is the study of the influence of the micro mechanical parameters characterizing the beds on their macroscopic behaviour (progressive compaction). The fourth specific objective is the study and quantification of the contact forces and the derivation of micro-macro correlations which may be used for design purposes. The last two specific objectives are met by pebble-scale numerical modelling.

Chapter 2

Overview of the parameters affecting the thermomechanical behaviour of packed beds

A pebble bed is a multiphase material consisting of a solid phase and a gas phase that fills the voids between pebbles. Due to their discrete nature, packed beds show a fully coupled thermomechanical behaviour. Here, the representative physical parameters characterizing a granular bed are introduced together with the mechanical and thermal parameters affecting its thermomechanical behaviour.

2.1 Physical and mechanical parameters characterizing a packed bed

The parameters characterizing a packed bed can be classified as macro and micro scale parameters. Regarding the physical macro parameters, the basic parameters are the mass m_{pb} [g] and the volume V_{pb} [cm³] of a packed bed. The ratio between the mass and the volume is defined as density [gr/cm³] of the packed bed:

$$\rho_{pb} = \frac{m_{pb}}{V_{pb}}. \quad 2.1$$

A macro parameter, related to the density of the bed, is the packing factor PF [%]. The PF is defined as the ratio of pebble volume (V_p [cm³]) to pebble bed volume (V_{pb})

$$PF = \frac{V_p}{V_{pb}} 100. \quad 2.2$$

The PF is related to ρ_{pb} by

$$\rho_{pb} = \rho_p PF, \quad 2.3$$

where ρ_p is the density of the pebbles [g/cm³].

The PF is influenced by many parameters such as the size distribution of the particles, the particle shape and their surface roughness, the dimensions of the structure in which the particles are contained, the ratio between the dimensions of the container and the diameter of the particles and the filling procedure [6].

In this work, the notion of packing state of a granular bed is introduced, in addition. The packing state of a granular bed is identified by the PF and all the other conditions (such as the particle size to container size ratio, particle shape etc.) that influence it. For instance, two packed beds with the same PF could have a different packing state due to the different particle size to container size ratio or particle shape used.

The Uniaxial Compression Test (UCT) (or oedometric compression test) is one of the few experimental options to get representative macro mechanical parameters of compressed granular beds. In UCT the pebbles, contained in a cylindrical container of diameter D [mm] to form a bed of height H [mm], are compressed in the axial direction by a piston connected to a testing machine. The bed axially deforms under the applied load while the lateral deformation is inhibited by the container. The overall macroscopic stress σ [MPa] (equal to the applied loading force divided by the area of the piston) and the overall macroscopic bed strain ε [%], defined as change of pebble bed height over initial height, characterize the behaviour of the bed. In particular, the obtained stress-strain curve is used to study the macro mechanical response of the granular bed. The σ - ε response is influenced mainly by the physical and mechanical parameters of the particles as well as by the packing state of the bed. The micro mechanical particles parameters that mainly influence the effective macro mechanical response of a packed bed are the particle Young's modulus E , the pebble shape and the friction coefficient between the particles μ_f .

The stress-strain curve obtained by the UCT is influenced by the H/D ratio [16] that should be kept at less than 1. Increasing the bed height, the effective constraints at the cylindrical wall (due to friction) increase and may introduce arching of pebbles inside the container, reducing the actual pressure in the bed with increasing axial distance from the piston. This would result in a bed compressed only in the upper part [16]. Moreover, to assure that the mechanical response of the bed is governed by the bulk behaviour in the UCT, the dimensions of the cylindrical container should be much larger than the diameter of the individual pebbles (d).

A characteristic macro mechanical parameters derived from the σ - ε curve is the oedometric modulus calculated as

$$E = \frac{\Delta\sigma}{\Delta\varepsilon} . \quad 2.4$$

The oedometric modulus E [MPa] can be calculated during either the loading or the unloading branch of the σ - ε curve by selecting suitable stress and strain intervals.

The residual strain after the unloading ε_r is a macro mechanical parameter that quantifies the permanent deformation of the bed due to the compression. If a cyclic loading is imposed to the bed, the difference between the residual strains of two consecutive cycles $\Delta\varepsilon_r$, representing the increment of the irreversible residual strain due to the cycling loading, is a further macro mechanical parameter characterizing the macro mechanical response of the bed and.

The micro parameters characterize the pebble-scale response of the packed bed. The contact force at the pebble-pebble contact is a primary micro parameter that helps to quantify the forces to which the particles are subjected. To this end the maximum and the average normal contact forces are used. The contact forces are obtained by pebble-scale numerical modelling.

The PF as defined in eq. 2.1 represents the overall PF of the assembly. However, the packing factor is not constant inside the bed since it is influenced by the presence of the boundaries. The packing structure developed inside the assembly has a substantial influence on the overall micro and macro response of breeder beds. The packing factor profile inside the bed is a micro parameter that allows to investigate the influence of the boundaries on packing structure, i.e. how the particles are arranged along a dimension, of the packed bed.

The number of contacts that every particle experiences influences both the heat transfer and the mechanical response of the bed. The coordination number (CN) is a micro parameter that defines the mean number of contacts per particle. It is calculated as

$$CN = \frac{N_c}{N_p}, \quad 2.5$$

where N_c and N_p are the total number of contacts and the number of particles in the bed, respectively.

2.2 Heat transfer in packed beds

Since a pebble bed consists of a solid phase and a gas phase filling the inter particle voids, the heat transfer in packed beds depends on the thermal properties of the two constituent phases. Several heat transfer mechanisms take place in a packed bed: conduction in the solid material,

conduction and convection in the gas phase, conduction through the contact area between contacting particles and radiation between particles.

The solid to gas thermal conductivity ratio (k_s/k_g) affects the heat transfer in the bed. In pebble beds with low k_s/k_g the heat flux is uniformly distributed among the solid and the gas phases, while in beds with a high k_s/k_g ratio the heat flows mainly through pebbles and contact areas between particles since these are the paths of higher thermal conductivity [17]. A compressive load acting on a breeder bed results in an increase of the number of the contacts between pebbles and of the contact areas dimension of the existing contacts. Therefore, the effective thermal conductivity of beds with high k_s/k_g ratios is influenced by the bed deformation.

Even if the thermal conductivity of the gas phase is much lower than that of the solid phase (ceramic pebbles), the gas contribution heavily influences the effective thermal conductivity of a packed bed. According to the kinetic theory of gases, the thermal conductivity of an unconfined gas is independent of the pressure. However when a gas is confined in small gaps, as in a packed bed, its thermal conductivity decreases with decreasing pressure (Smoluchowski effect [18]). For a given temperature, the mean free path (λ) of the filling gas molecules increases with the decrease of the pressure. When the mean free path of the gas molecules reaches the order of magnitude of the geometrical dimension (d) where the gas is confined, its thermal conductivity becomes a function of its pressure. When $\lambda \gg d$ (unconfined gas) the interaction between the gas molecules dominates the heat transfer in the gas phase, while when $\lambda \approx d$ (rarified gas) the interaction between the gas molecules and the walls become effective; thus the thermal energy is directly transferred between the boundary walls, and the gas thermal conductivity becomes dependent on the gas pressure. The Knudsen number ($K_n = \lambda/d$ [1]) is representative of the degree of rarefaction of a gas and defines the limits for the different regimes. For $K_n < 0.001$ the filling gas can be considered as continuum, the heat in the gas is transferred by molecular interactions and the bed's thermal conductivity is independent of the gas pressure. For $0.001 < K_n < 10$ the thermal conductivity of the gas as well as the bed's effective thermal conductivity are influenced by the gas pressure. Decreasing the gas pressure the effective thermal conductivity of the bed drops because the mean free path gradually reaches the order of magnitude of the characteristic dimension of the volume where it is enclosed. The range $0.001 < K_n < 10$ is

defined transition regime. For $K_n > 10$ (very low pressures) the gas thermal conductivity is again independent of the gas pressure, the same happens for the bed's thermal conductivity. This regime is called free molecule.

Several models have been proposed to predict the thermal conductivity of a confined gas by using different approaches [19]. Based on the temperature jump model and the kinetic theory of gases, a correlation for the estimation of the thermal conductivity of a confined gas (k_g [W/(m K)]), named Knudsen relation, was proposed by Kaganer [20] in 1969. Because of the simple form and the reliable estimation, the Knudsen relation

$$k_g = \frac{k_0}{1 + 2 \beta K_n}, \quad 2.6$$

with

$$K_n = \frac{\lambda}{d} = \frac{\mathcal{K} T}{\sqrt{2} \pi d_m^2 p_g d}, \quad 2.7$$

has been widely used to predict the thermal conductivity of a confined gas in engineering applications [19]. Here k_0 [W/(m K)] is the thermal conductivity of non-confined gas, β [/] is a coefficient related to the energy transfer between the gas molecules and the solid material, $\mathcal{K} = 1.38 \cdot 10^{-23}$ [J/K] is the Boltzmann constant, T [K] is the temperature, d_m [m] is the molecule diameter, p_g [Pa] is the gas pressure and d [m] is the gap size. λ [m] is the mean free path defined as:

$$\lambda = \frac{\mathcal{K} T}{\sqrt{2} \pi d_m^2 p_g}. \quad 2.8$$

The constant β [/] depends on the gas type, the solid material and the temperature, as proposed by Kaganer:

$$\beta = \frac{2 - \alpha_c}{\alpha_c} \frac{2\delta}{\delta + 1} \frac{1}{P_r}, \quad 2.9$$

with

$$P_r = \frac{\mu c_p}{k_0}. \quad 2.10$$

Here α_c [/] is the thermal accommodation coefficient, $\delta = c_p/c_v$ [/] is the adiabatic index and μ [N/(s m²)] is the dynamic viscosity. The thermal accommodation coefficient represents the effectiveness of the molecule-wall energy transfer. It depends on the gas/surface combination as well as on the gas temperature. α_c can be determined either experimentally or theoretically. Baule

[21] derived a correlation considering the transfer of kinetic energy between two hard spheres representing the molecules. A modification of the Baule formula for the estimation of α , proposed by Goodman [22], is

$$\alpha_c = \frac{C m_r}{(1 + m_r)^2}, \quad 2.11$$

where $m_r = m_g/m_s$ [1] is the ratio of the gas (m_g) to solid (m_s) atomic masses, $C = 2.4$ [1] is an empirical constant introduced by Goodman to better reproduce the experimental results. eq. 2.11 reduces to the Baule formula for $C = 0$.

The Knudsen relation is modified, concerning the coefficient β , by several authors [19]. In the present study the correlation

$$\beta = \frac{2 - \alpha_c}{\alpha_c}, \quad 2.12$$

proposed by Wakao and Kagnei [23] is used. The various Knudsen regimes are exemplarily depicted in Figure 2-1. The values reported in the following graphs are calculated with eq. 2.6-2.12. The values used for the calculations are reported in Appendix A. In Appendix B the dimension of the gap size (d) is estimated, for fusion relevant pebble sizes, based on some basic contact schemes in order to figure out the range of gap sizes involved. The determined values were then used hereafter for the investigation of the influence of d on the gas thermal conductivity.

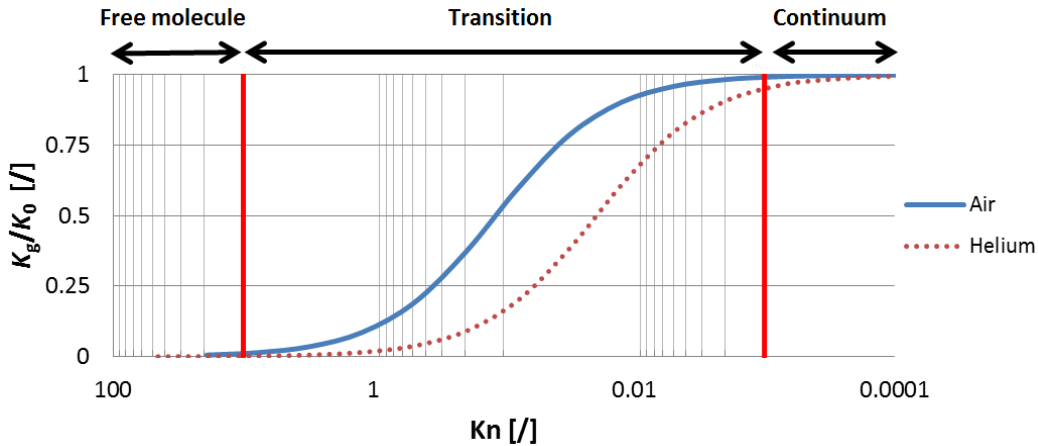


Figure 2-1: Calculated dependency of the gas thermal conductivity on the Knudsen number.

The influence of the gas pressure on the thermal conductivity of helium and air for different temperatures and gap sizes is shown in Figure 2-2 and Figure 2-3, respectively. In the figures the pressure range investigated in this study is highlighted in light orange. For a given gap size and

temperature, the thermal conductivity decreases with decreasing pressure with a characteristic S-shaped curve (in the semi logarithmic plot). According to eq. 2.6-2.7, in the transition regime ($0.001 < K_n < 10$) both a lower pressure and a higher temperature result in a longer mean free path resulting in a reduction of the gaseous contribution to the effective conductivity of the bed. For a granular/porous material the increase of the temperature could be sufficient to severely reduce the gas conductivity if the combination gap size, gas pressure result in $0.001 < K_n < 10$. While the increase of the temperature results in the onset of the Smoluchowski effect at higher pressures, the increase of the gap size shifts the transition regime to lower pressures, see Figure 2-3. With bigger gaps a lower pressure is needed for the mean free path of the gas molecules to reach the order of magnitude of the gap size.

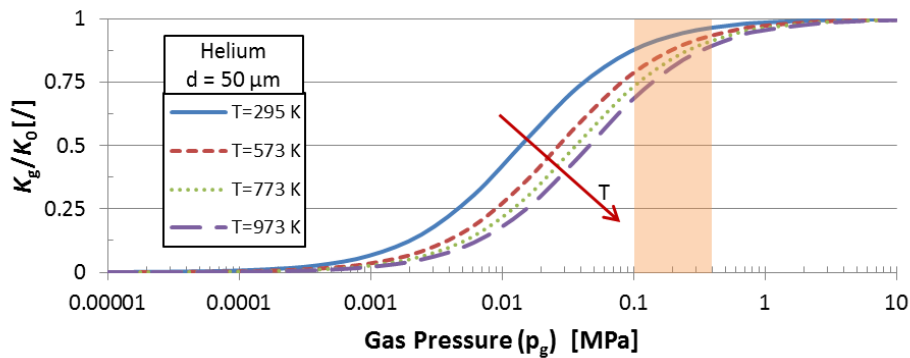


Figure 2-2: Calculated thermal conductivity of helium as a function of temperature and gas pressure for a constant gap size.

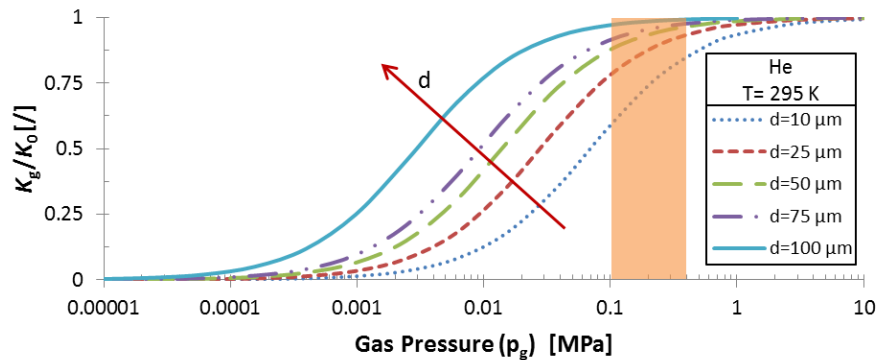


Figure 2-3: Calculated thermal conductivity of helium as a function of the gap size and gas pressure.

The dependence of gaseous thermal conductivity on gas type (air and helium) as a function of the gas pressure and of the gap dimension at RT is shown in Figure 2-4 and Figure 2-5, respectively. Compared to the helium atmosphere, in air the onset of the transition regime is shifted to lower pressures for a given gap size (Figure 2-4), and to a lower gap size for a give pressure (Figure 2-5). This reflects the lower mean free path of the air molecules compared to that of helium. The

higher mean free path of the helium molecules is due to their lower molecule diameter (d_m), see Appendix D. The mean free path of air and helium molecules in the investigated pressure range at RT is reported in Figure 2-6.

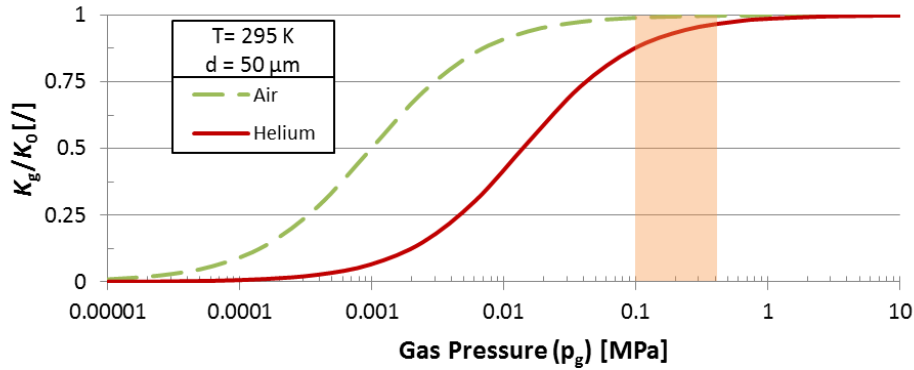


Figure 2-4: Calculated thermal conductivity of air and helium as a function of the gas pressure for a constant gap size.

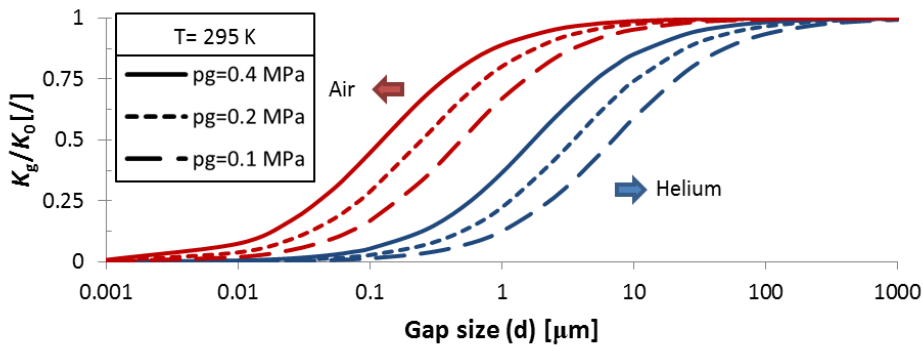


Figure 2-5: Calculated thermal conductivity of air and helium as a function of gas pressure and gap size for a constant temperature.

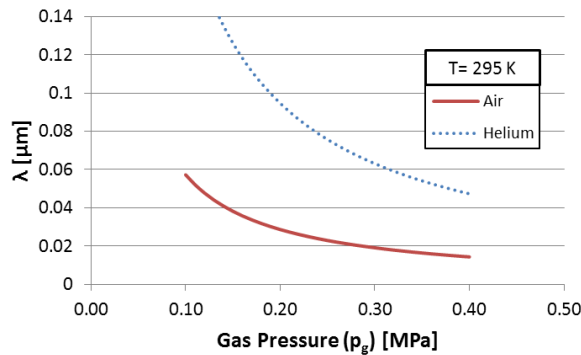


Figure 2-6: Calculated mean free path of air and helium molecules at RT.

Chapter 3

Thermal conductivity measurement methods and present know how on breeder beds thermomechanics

This chapter presents the results of the literature research. The first section provides an overview of the principal methods for measuring the thermal conductivity. The PhD work is based on the measurement of the effective thermal conductivity of ceramic breeder material pebble beds by using the hot wire method. Literature pertaining to this method will be treated in detail. In the second section, the related work on the thermomechanics of ceramic pebble beds is reviewed.

3.1 Methods for the measurement of thermal conductivity

3.1.1 Steady state methods

Steady state methods determine the thermal conductivity of a material by inducing a thermal gradient in the test sample. The measurement is performed when the sample reaches the thermal equilibrium (hence the name steady state methods) and the heat flux is uniform through the sample reducing the mathematics describing the heat conduction to the Fourier's law. Fourier's law is the constitutive equation for thermal conduction. It provides the definition of thermal conductivity founding the basis of all methods of determining its value. Fourier's law is an empirical relationship, first formulated by Fourier in 1822 [24], that relates the heat flux in a material to the temperature gradient. For a homogeneous and isotropic material this reads as

$$\vec{q} = -k \nabla T, \quad 3.1$$

where \vec{q} is the heat flux [W/m^2], k is the material's thermal conductivity [$\text{W}/(\text{m K})$] and ∇T is the temperature gradient [K/m]. Methods based on steady state heat flow differ in the specimen geometry, in the design of measurement system and in the method used to calculate the heat flux.

All experimental set-ups are designed to simplify the mathematics by reducing the heat transfer problem to a one-dimensional one. A unidirectional heat flux is induced in the material to be tested so that eq. 3.1 reduces to its one-dimensional form

$$q_x = -k \frac{dT}{dx} . \quad 3.2$$

Knowing the heat flux q_x and the thermal gradient $\frac{dT}{dx}$ in the sample, the specimen's thermal conductivity can be calculated as

$$k = q_x \frac{\Delta x}{\Delta T} . \quad 3.3$$

The main challenge of the steady state methods is to produce a perfect one-dimensional heat flow in a finite sample. To this end, great efforts are devoted to minimize the heat flow perpendicular to the direction of interest. The steady state techniques perform the measurement when the material to be analysed is in complete thermal equilibrium. This imply an easy processing of signals, on the other hand long measurement times and complicated experimental facilities are usually needed for steady state methods.

3.1.1.1 Comparative cut bar

In this technique a sample with a defined thickness, is placed between two identical reference specimens of known thermal conductivity and thickness [25]. The obtained test assembly is then placed between two temperature-controlled heaters at constant but different temperatures, to impose a thermal gradient along the assembly. In order to minimize the radial heat losses, the test assembly is surrounded by insulation or heaters. A schematic representation of the test assembly is reported in Figure 3-1a. According to eq. 3.2 the thermal gradients in the reference specimens and in the sample are inversely proportional to the respective thermal conductivity. After reaching the thermal equilibrium, the temperature gradients in both, the reference specimens and the sample are measured by means of thermocouples placed at known locations in each material. A minimum of two or more thermocouples should be placed in the reference specimens and in the sample, respectively. If more than two thermocouples are used, whenever possible, the linearity of the temperature gradient in the material can be confirmed. The heat flux flowing in the test assembly is calculated by measuring the thermal gradient in the specimens of known thermal conductivity. Knowing the thermal gradient and heat flux flowing through the specimen, its thermal conductivity is then calculated by means of eq. 3.3. The

comparative cut bar is one of the ASTM test standards for thermal conductivity measurement [25].

3.1.1.2 Heat flow meter technique

A unidirectional heat flow is induced in the test sample being placed between two parallel temperature-controlled heaters kept at constant but different temperatures, as depicted in Figure 3-1b. This technique makes use of a calibrated heat flux transducer for measuring the heat flux flowing through the test material. Once the thermal equilibrium is reached, the temperature gradient in the test material is measured by means of thermocouples placed at known locations. The thermal conductivity is then calculated according to eq. 3.3. The heat flow meter technique is one of the ASTM test standards for thermal conductivity measurement [26].

3.1.1.3 Guarded hot plate technique

The guarded hot plate technique can be used either in a two sided or a one sided mode. The standard method [27] makes use of two samples symmetrically arranged on both sides of the main heater, see sketch in Figure 3-1c. The test assembly consisting of the main heater and the two specimens is placed between two cold plates kept at lower temperature than the main heater. In the single sided configuration [28], the test sample is placed between the main heater and the cold plate. In both configurations, guard heaters are used to minimize the lateral heat flow. In the single sided configuration, an additional heater is used as a guard plane to create an adiabatic surface on the backside of the main heater. The heat flux is calculated as the ratio of the power generated by the main heater and its surface area. At the thermal equilibrium, the temperature gradient across the specimen is measured by means of thermocouples and the thermal conductivity of the specimen is calculated by means of eq. 3.3.

3.1.1.4 Radial Heat Flow Method

This technique uses a cylindrical geometry as heat transfer model. A cylindrical heater is placed along a cylindrical specimen's axis, while a band heater, surrounding the specimen, is used to heat up the sample up to the test temperature. The test assembly (core heater/test specimen/band heater) is surrounded by thermal insulation, as shown in Figure 3-1d. The experimental apparatus has been developed either with or without end guard heaters [29]. After the system reaches the steady state, the core heater is switched on and a thermal gradient arises in the specimen. Two (or more) thermocouples at different radii are used to measure the radial

gradient in the specimen. For a one dimensional cylindrical heat transfer problem eq. 3.1 is solved for a cylindrical coordinate system, rearranged to calculate the thermal conductivity yields

$$k = \frac{Q}{2\pi L_h} \frac{\ln\left(\frac{r_2}{r_1}\right)}{(T_1 - T_2)}, \quad 3.4$$

where Q is the power generated [W] by the core heater of length L_h [m] and $T(r)$ is the temperature at radius r . Q is determined as $Q = V I$, where V [V] and I [A] are the voltage and the electric current flowing through heater element, respectively. An inaccuracy of this method, as well as for all steady state methods, is the control of the undesired axial heat flow. This technique has been utilized over a wide temperature range with specimens in either solid or powder form.

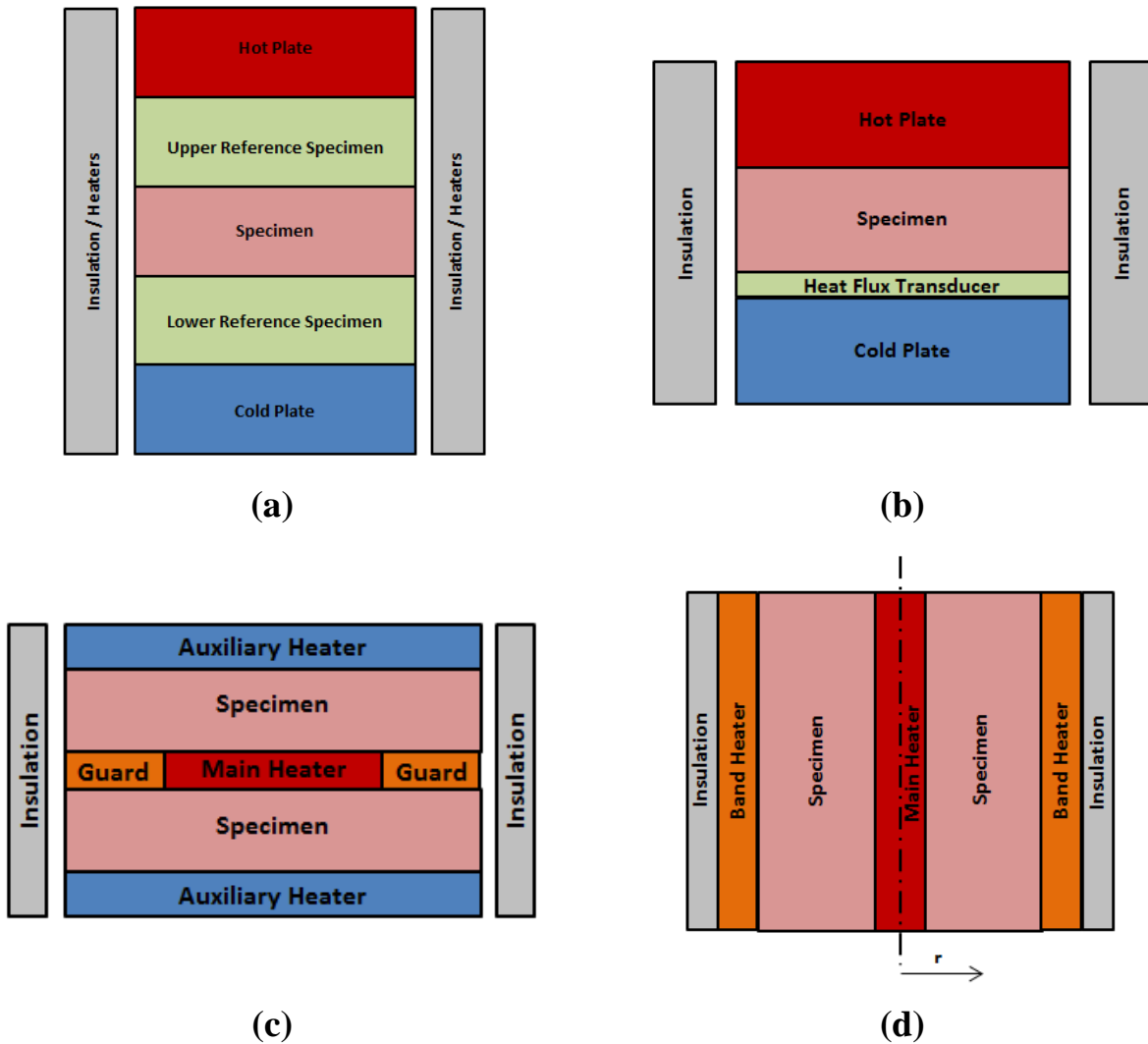


Figure 3-1: Illustration of the geometrical arrangement of the main components of different methods for the measurements of the thermal conductivity: (a) comparative cut bar, (b) heat flow meter, (c) guarded hot plate and (d) radial heat flow techniques.

3.1.2 Transient methods

The heat equation is a partial differential equation that describes the change in temperature over time and position. This equation arises from the energy balance in a continuum and Fourier's law. In absence of internal heat generation and for a constant thermal conductivity, it reads to:

$$\rho c_p \frac{\partial T(\vec{r}, t)}{\partial t} = k \nabla^2 T(\vec{r}, t), \quad 3.5$$

where ρ is the material's density [Kg/m³], c_p is the specific heat [J/(Kg K)], T is the temperature [K], t is the time [s] and k is the thermal conductivity [W/(m K)]. Transient techniques make use of this equation to obtain the thermal conductivity. The transient approach performs a measurement during the heating up of the sample. For this reason, transient technique measurements can be made relatively quickly, while techniques based on the steady state approach are very time consuming (usually a long time is needed to reach the required steady state temperature difference). A well-engineered experimental setup is usually needed in order to assure that the heat conduction is unidirectional so that eq. 3.5 is simplified to its one-dimensional form. Thin wires, needles or planes are used as heaters for the transient techniques. Several measuring systems are commercially available either using a plane [30]-[31] or a needle [32]-[33] heater.

3.1.2.1 Flash Diffusivity Method

A face of a disc specimen of defined thickness is heated up by a short duration light pulse produced by a laser [34]. The heat diffuses in the sample and the resulting temperature rise of the rear face is recorded. The thermal diffusivity ($\alpha = k/\rho c_p$) is calculated by analysing the characteristic temperature vs. time graph describing the temperature rise of the rear surface. This value is then used to calculate the thermal conductivity according to

$$k = \alpha \rho c_p, \quad 3.6$$

where α is the thermal diffusivity of a material [m²/s], ρ is the density [Kg/m³], c_p is the specific heat [J/(Kg K)].

A furnace can be used to heat up the sample in order to determine the thermal conductivity over a temperature range. The sources of uncertainties related to this method are associated to the specimen itself (homogeneity of the material), the deviation from unidirectional heat flow and the accuracy of the temperature measurement system. Other sources of uncertainty are the radiative

and conductive heat losses and the non-uniform heating of the sample. The detailed theoretical background of the flash diffusivity method can be found in [34].

3.1.2.2 Hot wire and probe methods

The Hot Wire Method (HWM) is a transient technique. A linear heat source (a thin wire or a thin heated probe) is embedded in the material to be investigated. By analysing the temperature rise of the heater, over a defined time interval, the thermal conductivity of the surrounding material is derived. The temperature rise of the wire is measured by thermocouples. In some applications the heating wire can be used as resistance thermometer. The theory of the hot wire method first developed by [35] is based on the solution of the heat conduction equation for an infinitely long linear heat source embedded in an infinite homogenous medium. If a spatially constant amount of heat per unit length q' , instantaneously generated at $t=0$ is kept constant in time; the temperature rise T at time t is expressed as

$$T(r, t) = -\frac{q'}{4\pi k} E_i\left(\frac{-r^2}{4\alpha t}\right), \quad 3.7$$

where r is the radial distance from the line source, k and α are the thermal conductivity and the thermal diffusivity of the material, respectively. $E_i\left(\frac{-r^2}{4\alpha t}\right)$ is an exponential integral, that in its series representation reads as

$$E_i(-x) = \gamma + \ln x + x + \frac{x^2}{2 \cdot 2!} - \frac{x^3}{3 \cdot 3!} + \frac{x^4}{4 \cdot 4!} + \dots, \quad 3.8$$

where γ is the Euler's constant. For small values of x (< 1), eq. 3.8 can be approximated as

$$E_1(-x) = \gamma + \ln x. \quad 3.9$$

For this application small x means sufficiently large value of time. Under this assumption eq. 3.7 reduces to

$$T(r, t) = \frac{q'}{4\pi k} \left(-0.5772 - \ln \frac{r^2}{4\alpha t} \right). \quad 3.10$$

For a fixed r , the temperature rise T_2 and T_1 at times t_2 and t_1 is given by

$$T_2 - T_1 = \frac{q'}{4\pi k} \ln \frac{t_2}{t_1}, \quad 3.11$$

from which it is possible to calculate the value of the thermal conductivity k as

$$k = \frac{q' \ln\left(\frac{t_2}{t_1}\right)}{4\pi T_2 - T_1} = \frac{2.3 q' \log_{10}\left(\frac{t_2}{t_1}\right)}{4\pi T_2 - T_1} = \frac{2.3 q'}{4\pi S_{10}}. \quad 3.12$$

Here, $S_{10} = \frac{T_2 - T_1}{\log_{10}\left(\frac{t_2}{t_1}\right)}$ is the slope of the linear region of the temperature transient used to calculate the material's thermal conductivity. In the present study S_{10} is evaluated by least squares fitting of the temperature vs. the $\log_{10}(t)$ graph in the selected time interval. The power q' [W] is calculated by

$$q' = \frac{R l_{he} I^2}{L_p}, \quad 3.13$$

where R is the characteristic resistance of the wire [Ω/m], l_{he} is the length of the heating element [m], I is the electric current flowing through heater element [A] and L_p is the length of the probe [m]. R is determined by

$$R = \frac{\rho_{he}}{A_{he}}, \quad 3.14$$

where ρ_{he} [Ω/mm^2m] and A_{he} [mm^2] are the temperature dependent resistivity as provided by the supplier and the cross section area of the heating element, respectively. In the present study, a probe has been used as a linear heat source.

A modification of the HWM for granular materials employs a more robust probe instead of a wire. In this technique the heater and the thermocouple are enclosed in a thin clad, which is embedded in the material to be investigated. The heating wire enters the clad from one end, runs all along the length and back to leave it at the same end, see sect. 4.1 for the detailed description of the probe design. Accounting for $l_{he} = 2 L_p$ in eq. 3.13 due to the design of the heated probe, eq. 3.12 yields

$$k = \frac{2.3 R I^2}{2\pi S_{10}}. \quad 3.15$$

The probe method is a modification of the hot wire method. Both methods are based on the same theory utilizing the line heat source theory. The temperature rise is still proportional to the logarithm of time with an additional term depending on the contact resistance at the probe/medium interface. The same general method can be used to determine the thermal conductivity using either the probe or the linear heat source (hot wire).

Figure 3-2 shows a qualitative temperature vs. the natural logarithm of time graph for the transient hot wire method. As shown, a linear region between two non-linear portions at both short and long times exists. For a reliable measurement of the thermal conductivity, only the

linear region has to be taken into account. Any practical application of the HWM deviates from a perfect linear heat source. The truncation of eq. 3.8 together with the finite dimension of the probe, the contact resistance at the probe/medium interface and the finite dimension of the sample are all sources of errors of the probe method. These errors can be minimized by a tailored design of the probe (i.e. by choosing an appropriate length to diameter ratio) and by discarding the early and the late regions of the temperature transient affected by the non-linearities due to the contact resistance and boundary effects (see sect. 4.1 for the detailed design of the probe). A detailed survey of the probe theory and of the errors associated can be found in literature [36]-[42].

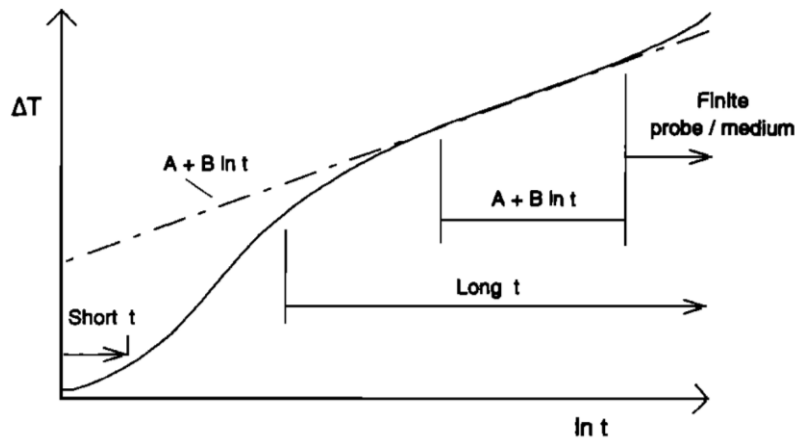


Figure 3-2: Qualitative temperature vs. logarithm of time plot (from [36]). The finite probe/medium can cause a rise in temperature (as reported) or a fall.

3.2 Related work

The effective mechanical and thermal properties of a granular bed, even though directly related to the properties of the base material, cannot be derived from the properties of a single pebble. Therefore, the characterization of single pebbles as well as of pebble beds is of primary importance for the understanding of the pebble bed thermomechanics. Here, an overview of the performed experimental and numerical investigations on the effective thermal and mechanical properties of pebble beds is given.

3.2.1 Thermal conductivity of breeder beds

The effective thermal conductivity of the lithium ceramics pebble beds was investigated in several studies. The main outcomes of the previous studies are presented hereafter.

In 1990, Dalle Donne and Sordon [43] measured the effective thermal conductivity of Li_4SiO_4 pebble beds with a pebble size of 0.5 mm. The steady state radial heat flow method was

used. The effective thermal conductivity was investigated in the temperature range 50-350 °C in helium at 0.1 MPa. An increase of effective thermal conductivity with the temperature was reported. Results of this study compared with other studies in Figure 3-6.

In 1991, Sullivan et al. [44] measured the thermal conductivity of a 1.2 mm Li_2ZrO_3 pebble bed in 0.1 MPa helium gas over the temperature range 70-500°C. An increase of the effective thermal conductivity with the temperature was observed. The pressure dependence of the thermal conductivity of alumina pebble beds (1-3 mm diameter) in the pressure range 3-100 KPa was investigated as well. A reduction of the effective thermal conductivity with the reduction of the gas pressure was observed. The experimental results were compared with the values predicted by the Hall and Martin (HM) correlation [45]. This correlation describes the thermal conductivity of a packed bed by the study of the heat transfer in a basic thermal cell. In Figure 3-3 the results of this work are reported.

Enoeda et al. [46] investigated the effective thermal conductivity of Li_2O pebble beds in 1994 by a steady state method. The experiments were carried out with 1 mm pebbles in 1 bar helium atmosphere with a gas velocity from 0 (stagnant) to 10 cm/s. Preliminary tests showed that there was no influence of the gas velocity on the temperature profile, therefore the experiments were then carried out with stagnant helium. The thermal conductivity was investigated in the temperature range 150-650°C. For a packing factor of 48% the measured value was about 0.9 W/(mK) with a slight tendency to decrease with the temperature. Sintering occurred around the inner cooling tube resulting in the formation of a solid core and of a sintered region of pebbles with a higher packing factor than the initial packed bed. The estimated packing factor of the solid and the sintered zones were 71% and 55%, respectively. The increase of the packing factor resulted in an increase of the effective thermal conductivity.

In 1994, Dalle Donne et al. [47] repeated the experiment performed in 1990 using a similar apparatus. The temperature range was extended up to 720°C. Helium was used as filling gas. The bed packing factor was 64.4%. The obtained data were correlated in the temperature range 40-720 °C by the equation

$$k = 0.708 + 4.51 * 10^{-4} T + 5.66 10^{-7} T^2, \quad 3.16$$

where k is in [W/(m K)] and T is in [°C].

In 1995, Gierszewski et al. [48] presented their results on the effective thermal conductivity of 1.2 mm Li_2ZrO_3 pebble beds in 1 bar helium. The effective thermal conductivity was investigated in the temperature range 100-1175 °C. For 1.2 mm Li_2ZrO_3 pebbles (density ~ 82 % of theoretical density and PF=63 %) in 0.1 MPa helium, the bed's thermal conductivity was fitted by

$$k = 0.66 + 1.17 * 10^{-7} T^{2.2}, \quad 3.17$$

where k is in [W/(m K)] and T is in [°C]. No significant influence of the mechanical external load on the effective thermal conductivity of the bed was found.

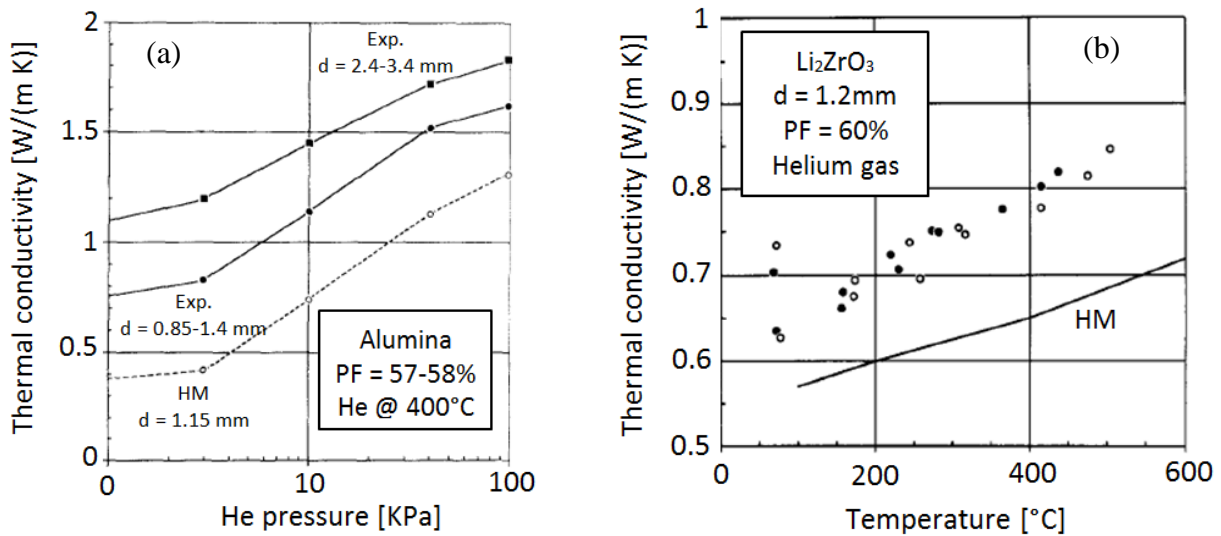


Figure 3-3: Pressure dependence of thermal conductivity of alumina pebble beds for different pebble size (experimental and calculated values) (a) thermal conductivity of 1.2 mm Li_2ZrO_3 pebble bed in He at 0.1 MPa (experimental and calculated values) (b). After [44].

In 1998, Earnshaw et al. [49] published their results on the effective thermal conductivity of Li_2ZrO_3 pebbles beds in helium over a temperature range of 75-1170°C. The effect of the helium pressure was assessed varying the helium pressure in the pressure range $0.01 < p < 300$ KPa. The effective thermal conductivity of the bed was found to depend on both the helium purge gas pressure and the temperature of the bed. The results are shown in Figure 3-4. At 100 KPa, the thermal conductivity is given by

$$k = 0.69 + 2.2 * 10^{-10} T^3, \quad 3.18$$

where k is in [W/(m K)] and T is in [K].

In 2000, Dalle Donne et al. [50] measured the thermal conductivity of Li_4SiO_4 pebble beds, with a pebble size of 0.25-0.63 mm, as a function of the bed average temperature and of the

helium pressure. The experiment showed that the effective thermal conductivity of the bed is not influenced by the filling gas pressure for pressures higher than 1 bar. The increase of effective thermal conductivity with the temperature was confirmed. Results are reported and compared with other studies in Figure 3-6. The effective conductivity of the bed was correlated by

$$k = 0.768 + 0.496 * 10^{-3}T, \quad 3.19$$

where k is in [W/(m K)] and T is in [°C].

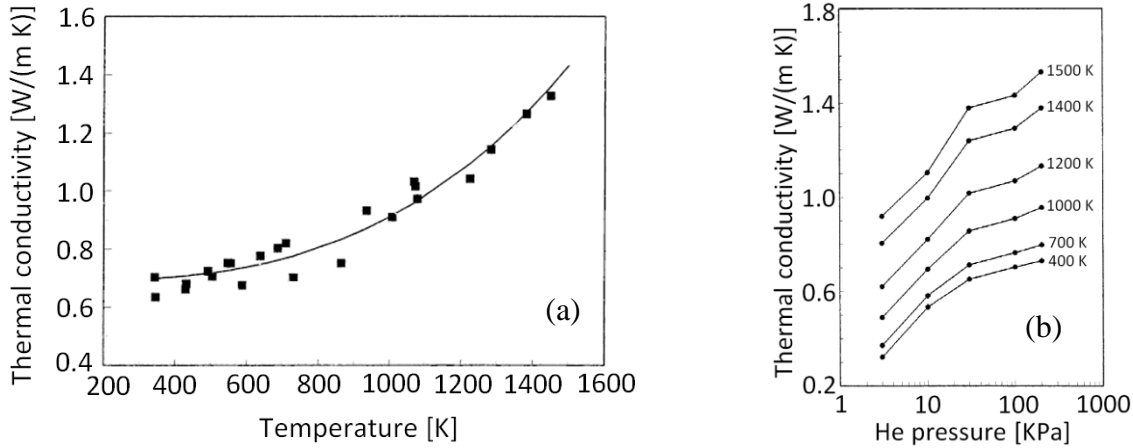


Figure 3-4: Effective thermal conductivity of Li_2ZrO_3 pebble bed in He at 100 KPa (a) pressure dependence of thermal conductivity of Li_2ZrO_3 pebble bed in He at various temperatures (b). Reproduced from [49].

In 2001, Enoeda et al. [51] presented their results on the effective thermal conductivity of Li_2TiO_3 , Li_4SiO_4 , Li_2ZrO_3 and Li_2O . The hot wire method was used. The thermal conductivity was investigated in the temperature range 425-775 °C. Helium at 0.1 MPa was used as filling gas. The helium pressure dependence was assessed for Li_4SiO_4 and Li_2ZrO_3 at about 520 °C for helium pressures ranging from 0.0001 to 0.2 MPa. Li_2O showed the highest thermal conductivity (≈ 1.8 W/mK) while all other investigated breeder materials show almost the same value (≈ 1.0 W/mK). In Figure 3-5 and Figure 3-6, the measured thermal conductivities are reported and compared with previous studies. The results were also compared with the correlations derived by Bauer and Schlunder (SBZ) [52] and Hall and Martin (HM) [45]. As for the HM correlation, also the SBZ correlation is based on a mathematical model that describes heat transfer in a basic cell. A good agreement was found from both hot the wire method and the steady state method for the effective thermal conductivity of Li_4SiO_4 pebble beds. It was found that the effective thermal conductivity of the bed is strongly influenced by the filling gas pressure in the pressure range 0.0001-0.1 MPa, see Figure 3-7. The thermal conductivity always increases with the increase of the helium pressure; however, the increment is attenuated for pressures above 0.1 MPa. The

experimental results were found to be in agreement with the values predicted by the mathematical models.

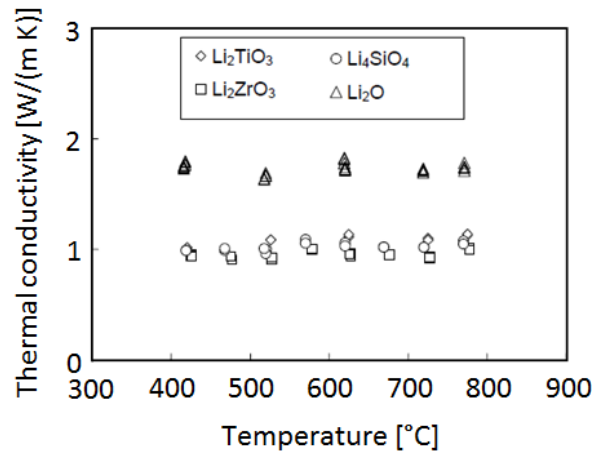


Figure 3-5: Comparison of measured effective thermal conductivity of Li₂O, Li₂TiO₃, Li₂ZrO₃ and Li₄SiO₄ Pebble Bed in He at 0.1 MPa. After [51].

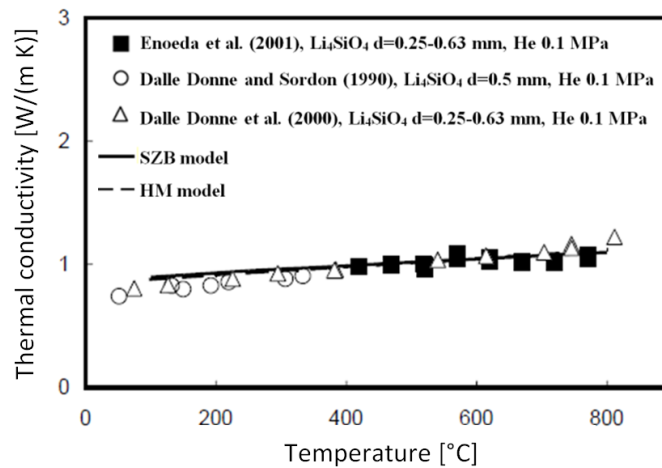


Figure 3-6: Comparison of thermal conductivity of Li₄SiO₄ pebble beds in He at 0.1 MPa as a function of the temperature from [51] and comparison with results from [43] and [50]. After [51].

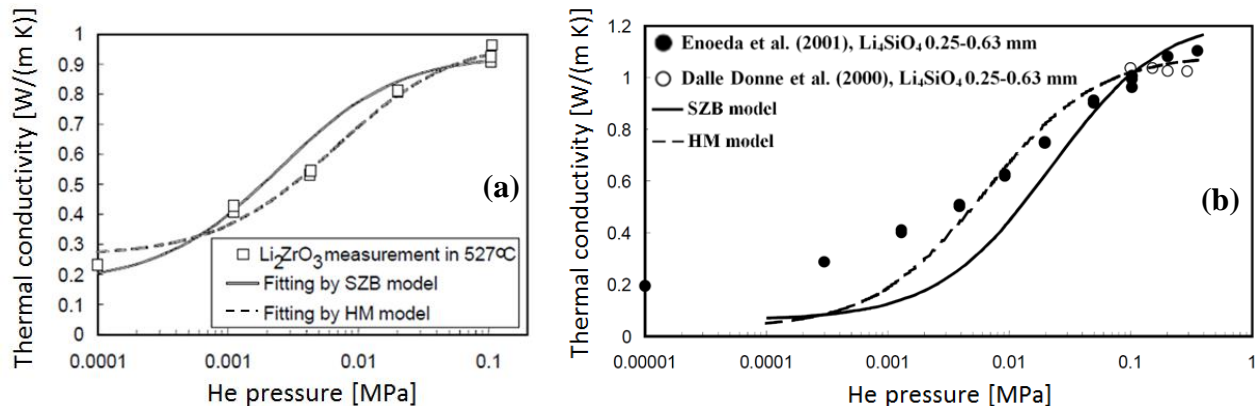


Figure 3-7: Pressure dependence of thermal conductivity of Li₂ZrO₃ (a) and Li₄SiO₄ (b) pebble beds in He. After [51].

In 2002, Reimann and Hermsmeyer [53] measured the effective thermal conductivity of compressed ceramic breeder pebble beds. Li_4SiO_4 and different types of Li_2TiO_3 pebble beds (monosized and binary beds) were used. The effective thermal conductivity was measured for bed deformations up to 4.5% and temperatures up to 800°C using the transient hot wire technique. Most of the measurements at high temperatures were performed in air. At ambient temperature, helium and argon were also used. Figure 3-8 shows the influence of the bed strain on the measured effective thermal conductivity observed in this work. A slight increase of the effective thermal conductivity with increasing strain was observed. For uncompressed beds in helium at elevated temperatures, the correlation of Dalle Donne et al. [50] for Li_4SiO_4 beds was confirmed. In air a severe reduction of the thermal conductivity was observed. The correlation reads to:

$$k = 0.768 + 0.496 * 10^{-3}T + 0.045 \varepsilon , \quad 3.20$$

for deformed pebble beds in a helium atmosphere of 0.1 MPa was proposed, where k is in $[\text{W}/(\text{m K})]$, T is in $[\text{C}^\circ]$ and ε is the uniaxial strain in [%]. The equation above reduces for uncompressed beds to the correlation given by [50].

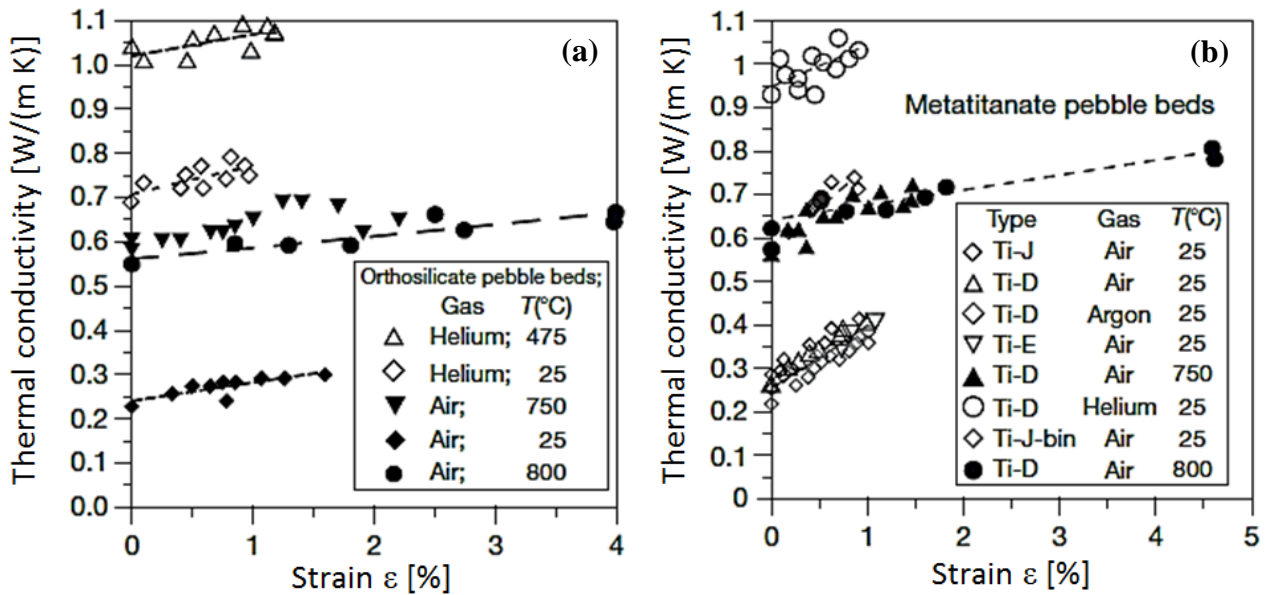


Figure 3-8: Thermal conductivity as a function of the bed strain ε for Li_4SiO_4 (a) and Li_2TiO_3 (b) pebble beds. Reproduced from [53].

The effective thermal conductivity of monosized and binary compressed Li_2TiO_3 pebble beds was measured by Hatano et al. [54] in 2003 using the hot wire method. The thermal conductivity was investigated in the temperature range $420\text{--}775^\circ\text{C}$. Helium was used as filling

gas. The results are reported in Figure 3-9. An increase of effective thermal conductivity with the temperature was reported. The effect of the compressive load at high temperature was assessed; it was found that the effective thermal conductivity slightly increases with the strain of the pebble bed.

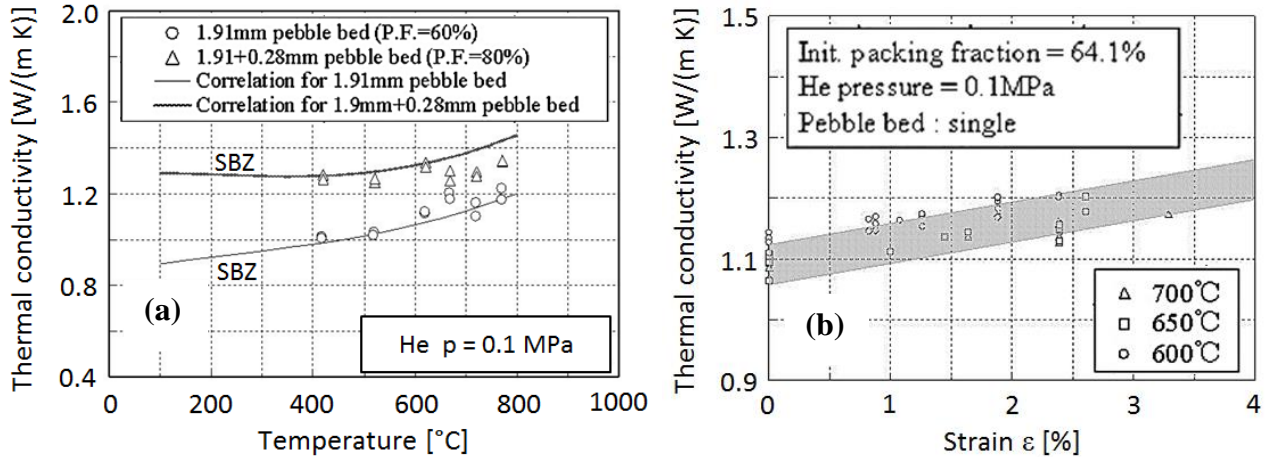


Figure 3-9: Effective thermal conductivity of Li_2TiO_3 pebble bed as a function of the temperature (a) and of the bed strain (b). After [54].

Using a new apparatus allowing the simultaneous measurement of effective thermal conductivity and stress–strain properties, Tanigawa et al. [55] presented their results on the effective thermal conductivity of Li_2TiO_3 pebble beds in 2005. The transient hot wire method was used. The effective thermal conductivity of the bed was measured under compressive load up to 10 MPa at temperatures ranging from 673 to 973 K. A slight increase of the effective thermal conductivity due to compressive deformation was confirmed as well as the increase of effective thermal conductivity with the temperature, see Figure 3-10.

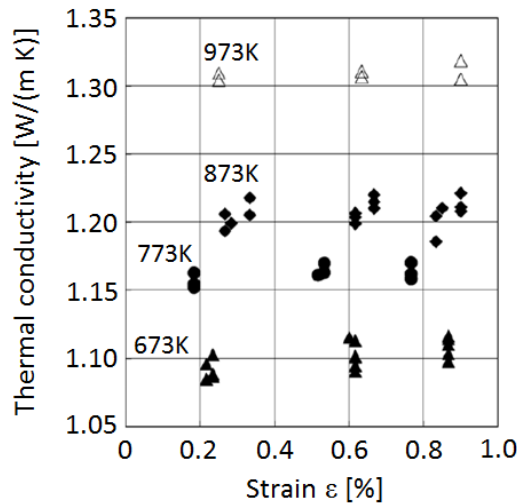


Figure 3-10: Thermal conductivity of Li_2TiO_3 pebble bed as a function of the bed strain for various temperatures. After [47].

In 2007, Abou Sena et al. [56] measured the effective thermal conductivity of Li_2TiO_3 pebble beds as a function of the average bed temperature in the range of 50–500 °C using the steady state axial flow method. 1.7–2 mm diameter pebbles were used, the bed packing factor was 61%. Helium at atmospheric pressure was used as filling gas. The results from this work show the tendency of a decrease of the effective thermal conductivity with increasing temperature. The experimental results showed that the thermal conductivity decreased from 1.40 to 0.94 W/mK with the increase of temperature from 50 to 500 °C.

In 2015, Feng et al. [57] investigated the effective thermal conductivity of Li_4SiO_4 pebble beds using the transient plane source method. Monosized pebbles were used (1.0 mm pebble diameter) with a packing factor of about 63%. By means of this method the thermal conductivity, thermal diffusivity and specific heat capacity were simultaneously determined. The thermal parameters of the uncompressed bed were investigated in the temperature range RT-600 °C. It was found that the effective thermal conductivity and the effective specific heat increase with increasing temperature of the bed, while the thermal diffusivity decreased with the increasing temperature of the bed. The effective conductivity, thermal diffusivity and specific heat capacity were correlated in the temperature range RT-600 °C by the equations

$$k = 0.97198 + 5.04496 * 10^{-4}T + 3.30432 * 10^{-7}T^2, \quad 3.21$$

$$\alpha = 0.5476 - 4.08679 * 10^{-4}T + 1.95265 * 10^{-7}T^2, \quad 3.22$$

$$c_p = 1.57753 + 0.00179 T + 2.22244 * 10^{-6}T^2, \quad 3.23$$

where k is in [W/(m K)], α in [mm^2/s], c_p in [J/(Kg K)] and T is in [°C].

Summarizing, a literature regarding the investigation of the effective thermal conductivity of lithium orthosilicate (Li_4SiO_4) [43], [47], [50], [51], [53], [57], lithium metazirconate (Li_2ZrO_3) [44], [48]-[49], [51], lithium metatitanate (Li_2TiO_3) [51], [53], [54]-[56] and lithium oxide (Li_2O) [46], [51] materials exists. Both transient [51], [53]-[55], [57] and steady state [43], [44], [46]-[50], [56] methods were utilized. The thermal conductivity was found to be mainly influenced by the temperature, the thermal conductivity of the ceramic material, the bed strain, the packing factor and by the filling gas type and pressure. All studies, except for [56], reported an increase of the effective thermal conductivity with the temperature. For some material the increase was more pronounced while other material, such as Li_2O , showed a poor temperature dependence. Only few reports on the measurement of the effective thermal conductivity of

compressed bed exist [48], [53], [54]-[55]. These reports detect a moderate increase of the thermal conductivity with the increase of the strain of the pebble bed. Li_2O beds showed the highest thermal conductivity compared to the other breeder materials investigated in [51], due to the inherently higher thermal conductivity of Li_2O . All reports in which the effect of the filling gas pressure was assessed [44], [49], [51] agree that the effective thermal conductivity of the bed is strongly influenced by the filling gas pressure in the pressure range 0.0001-0.1 MPa. For pressures above 0.1 MPa the pressure dependence, although still present, was found to be drastically reduced. Only in [50], the influence of the helium pressure was reported to be negligible for pressures higher than 0.1 MPa.

3.2.2 Thermomechanical behaviour of breeder beds

The effective mechanical properties of pebble beds were studied by dedicated experiments and modelling. A comprehensive survey about the status of ceramic breeder materials thermomechanics R&D can be found in [6], [58]. In this section, an overview of the experimental and numerical investigations on pebble beds thermomechanics is given.

The Uniaxial Compression Test (UCT) (or oedometric compression test) was extensively used to characterize the mechanical response of breeder beds. Several UCT experiments have been carried out by using different facilities and types of pebbles [59]-[66]. Figure 3-11 exemplarily shows an empirical stress-strain curve obtained from a UCT experiment [6]. The mechanical behaviour of the pebble beds is characterized by a nonlinear-elasticity accompanied by an irreversible residual strain after the unloading. This is due to a significant pebble rearrangement leading to a densification of the bed. At elevated temperatures the mechanical behaviour of the bed is more compliant because of the decay of the mechanical properties of the pebbles [63]; [66]. At temperatures higher than 600 °C thermal creep becomes evident [61]-[64]. When the bed is subjected to cyclic loading, the largest part of the irreversible residual strain is generated during the first few cycles [66], then the compaction of the bed is still progressing, but with smaller increments as the cycling proceeds. The results of UCT campaigns, carried out by various authors, were used to derive correlations for the creep rate and for the stress dependent oedometric modulus. Data from UCTs are used to derive the effective properties and to validate the results of modelling.

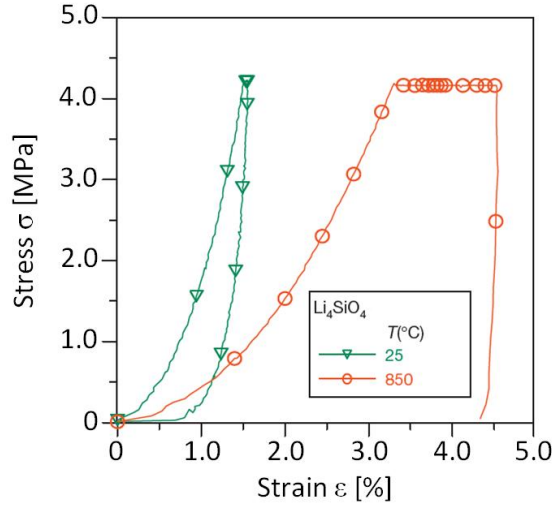


Figure 3-11: Experimental stress-strain curves at RT (green) and at high temperature (red). After [6].

The mechanical behaviour of pebble beds can be modelled by either a Discrete Element Method (DEM) or a continuum approach. In the continuum approach a set of phenomenological constitutive equations, based on the effective properties of the beds, are implemented in a FEM code to simulate the mechanical behaviour of the beds. The developed codes were validated with the out-of-pile mock-up experiments HELICA and HEXCALIBER [67]. The continuum approach was found to adequately represent the macroscopic thermomechanical behaviour of breeder beds, for further details see e.g. [6], [58].

The DEM, introduced by [68], is widely used to study the mechanical response of assemblies consisting of discrete particles. Each particle defined by its geometrical extension, the mass, the physical and mechanical properties, is tracked in a Lagrangian manner. The contact law between particles defines the inter particle forces (normal and tangential). Towards the microscopic interaction between the constituent particles, the macroscopic behaviour of the granular assembly is derived by solving the equations of motion for each single particle composing the assembly. Regarding the thermomechanics of breeder beds, the DEM is a powerful numerical tool that allows to deeply understand the physical meaning of the experimental outcomes thanks to the pebble-scale mechanical description. Moreover, the influence of the mechanical, thermal and geometrical properties can be systematically investigated. DEM has been widely adopted to study the thermomechanical responses of pebble bed assemblies. The use of DEM for fusion related applications was started by the researchers of the University of California Los Angeles (UCLA), who firstly used a DEM approach to study the

micro mechanics of breeder beds [60], [69]. In their following works [70]-[71] pebbles were packed in cuboidal and cylindrical assemblies confined by elastic walls made of steel and compressed in the axial direction, the stress strain response as well as the internal contact forces were investigated. Assemblies consisting of monosized spherical pebbles (diameter of 1 mm) with an initial packing factor, PF of $60\pm 0.5\%$ were studied. This packing density is slightly lower than the reference value for the solid BB concept. In their more recent works an open-source DEM code was employed to study the uniaxial compression of monosized packed assemblies with periodic boundary conditions [72] and the thermomechanics of breeder beds experiencing pebble failure [73]. In [72] a modified and randomly distributed young modulus was assigned to the pebbles according to experimental outcomes. An estimation of the percentage of crushed pebbles has also been made.

The DEM studies have been continued at the Karlsruhe Institute of Technology (KIT), where an in-house DEM code was developed by Gan and Kamlah [74]. The original KIT-DEM code was extended by Zhao et al. and Annabattula et al., who implemented the possibility to simulate polydispersed [75] and crushable [76]-[78] assemblies. Recently the development of the KIT-DEM code has been restarted. The code was further extended to study the bulk behaviour of assemblies composed of ellipsoidal particles [79].

The KIT approach [74]-[75], [78]-[79] was to simulate periodic cubic assemblies of random packed pebbles with periodic boundary conditions. Doing that, the bulk behaviour of the assembly dominates the mechanical response of the assembly. The assemblies were generated using a Random Close Packing (RCP) algorithm [80] with an initial PF of approx. 64%, consistent with the reference value of the actual EU BB design. The KIT-DEM code was successfully used in previous studies [74], [75] to investigate the mechanical behaviour of monosized, binary and polydispersed pebble assemblies. The influence of the initial PF [74] and the friction coefficient between pebbles [75] were investigated as well. In these simulation studies a defined uniaxial macroscopic strain (ϵ) was gradually applied on random pebble assemblies. When the defined maximum strain was reached, the assemblies were unloaded by gradually removing ϵ until the stress approaches zero. No repeating cycles were simulated, as the studies were focused on the first loading/unloading cycle. The DEM simulations accurately reproduced the characteristic mechanical behaviour of granular assemblies. The obtained stress-strain curves were found to be in good agreement with the UCT experimental outcomes [74],

[75]. The initial PF as well as the friction coefficient had a significant influence on the mechanical response of the assembly. The monosized assemblies were characterized by a stiffer behaviour than binary and polydispersed assemblies. For an initial PF of approx. 64%, a negligible residual strain was found for monosized assemblies. The micro mechanical parameter such as the average coordination number, the maximum and average contact forces were obtained as a function of the hydrostatic pressure.

With application to breeder beds, numerical and experimental studies on granular beds undergoing cyclic mechanical loading are comparatively rare. A recent research [81] investigated the effect of mechanical cycling on the behaviour of granular materials. The simulations were carried out with an assembly consisting of monosized spherical pebbles (diameter of 0.5 mm) with an initial packing factor (PF) of 59.9%. The pebbles were randomly generated in a cubic box made of steel. The bed was compressed imposing a cyclic loading on the top wall of the box, the number of compressive load cycles was limited to 10. The initial packing factor used in the study is actually below the reference value for the solid BB concept. Furthermore, in the EU solid BB concept polydispersed beds are used. Zhang et al. [66] investigated the stability of pebble beds under pulsed loading conditions. Both UCTs and Finite Element Method (FEM) simulations were conducted. The UCTs were performed at elevated temperatures (up to 750 °C) on both Li_4SiO_4 (PF = 61%) and Li_2TiO_3 (PF = 63%) tritium breeding materials. The FEM simulations were carried out to study the coupled thermomechanical problem of the HELICA mock-up experiment. In the very recently published studies [82]-[83], a commercial DEM code was used to study the cyclic behaviour of packed assemblies subjected to uniaxial compression with a considerable number of cycles (about 80). In [82] the influence of sphericity, size distribution and friction coefficient between pebbles on the cyclic behaviour of packed beds was assessed. The assemblies were uniaxially compressed with both target stress [82]- [83] and strain [83]. Mixed boundary conditions were used, the initial packing factors varied in the range 60-62%. The simulated pebble size was 1mm while, when simulated, a very narrow Gaussian size distribution (0.9-1.1 mm) and high sphericity (0.95) were used.

The experimental and numerical studies [66], [70], [81] and very recently [82]-[83] show that cyclic loading leads to a progressive compaction of the bed, resulting in an increase of the effective bed stiffness [70], [81]-[82]. Initially a large volume reduction occurs during the first cycles, then the compaction saturates as the cycling proceeds. In [81] the compaction was found

to obey a stretched exponential evolution law. The average and maximum normal contact forces were found to decrease to some extent with cycling, while the coordination number and effective elastic moduli increased [82]-[83]. In [66], beside the UTC experiments, FEM simulations were also carried out to study the coupled thermo-mechanical problem of HELICA mock-up experiment. A main outcome was that the cyclic thermal stress peaks acting on breeder pebble are relaxed, to then saturate after few thermal cycles, due to the pebble bed volume reduction.

DEM simulations have been recently employed to investigate the thermal behaviour of breeder beds. Attention was focussed on the investigation of the effective thermal conductivity [84]-[85] and on the prediction of the temperature distribution [86]-[88] of breeder beds subjected to neutronic heating. The effective thermal conductivity was found to be adequately represented and the experimental outcomes were numerically reproduced. A coupled DEM-CFD code was used in [86] allowing to take into account the contribution of the fluid motion on the heat transfer. The influences of pebble failure and bed orientation were investigated as well. It was found that the fluid motion helps to equilibrate the temperatures in the beds. The DEM was proven to be a robust approach to study the heat transfer taking into account the thermomechanical coupling in breeder beds. The temperature distribution and the mechanical state were found to be mainly affected by the PF, the particle size and size distribution [86]-[88]. In particular, beds with a higher initial PF show lower temperatures.

Chapter 4

Experimental set-up to measure the thermal conductivity of ceramic pebble beds

The experimental set-up is aiming to study the thermal conductivity of ceramic pebble beds as a function of temperature, chemical composition, compressive load and filling gas type/pressure. The hot probe method has been selected to measure the thermal conductivity of ceramic pebble beds. In this chapter, the developed experimental set-up for the investigation of the effective thermal conductivity of ceramic pebble beds is presented together with the probe design, its calibration and the evaluation of the uncertainty of the method [89].

4.1 Apparatus and experimental procedure

Figure 4-1 shows the developed experimental set-up for the measurements of ceramic pebble beds' thermal conductivity. The experimental setup is conceived to generate a purely radial heat flow around the probe ⑧. A cylindrical measuring ⑥ cell of 55 mm inner diameter with the probe placed along its axis is manufactured to be filled with ceramic pebbles. After filling the pebbles into the measuring cell a dummy piston made of stainless steel is placed above the bed with the only purpose to measure the bed height, Figure 4-2. The bed height is measured as $H = H_{mc} + h - H_{pist.}$, where h is the distance between the top of the dummy piston and the top of the measuring cell while H , H_{mc} and $H_{pist.}$ are the heights of the pebble bed, the measuring cell and of the piston, respectively. Using measurable quantities, the PF is calculated according to eq. 2.3 as

$$PF [\%] = \frac{m_{pb}}{V_{pb} \rho_p} 100, \quad 4.1$$

where m_{pb} and V_{pb} are the mass [g] and the volume [cm³] of the bed and ρ_p [g/cm³] is the density of the pebbles. The pebble bed is mechanically vibrated to reach the desired PF using an electric-mechanical vibrator. The initial Packing Factor (PF) of the bed is approx. 64 % with an initial height of approx. 40 mm. Ceramic disks ⑦ made of MACOR[®] [90] are placed below and above the pebble bed to thermally decouple it in the axial direction. MACOR[®] is a machinable

glass ceramic that can withstand high temperatures. It exhibits a low thermal conductivity (around 1.4 W/m K). The experimental setup is placed axially in a universal testing machine. By this, the pebble bed is compressed in the axial direction by a piston ① connected to the movable crossbar of the testing machine. The compressive load is measured by a load cell ⑩, while the bed strain ε [%] is calculated by:

$$\varepsilon [\%] = \frac{H - d_{pist.}}{H} 100 . \quad 4.2$$

Here, H is the initial bed height while $d_{pist.}$ is the displacement of the piston measured by means of three Linear Variable Displacement Transducers (LVDTs) ⑪ circumferentially equal spaced. A three axial heating zones furnace ⑫ surrounding the experimental setup is used to heat up the bed. A three zones furnace guarantees a better temperature uniformity of the sample through the control of three heated zones. The furnace control system controls the power of both end zones to follow the centre zone temperature. Four type K thermocouples ⑬, equally spaced along 360° at four different heights (namely $H_{tc} = 0, H/4, H/2, H$), are used to monitor the temperature of the measuring cell. The thermocouples are placed in dedicated holes radially drilled in the measuring cell. In Figure 4-1 only two of the four thermocouple' positions are visible, the other two are located on the back of the measuring cell. The LVDTs are placed outside the heated zone of the facility thanks to a displacement measuring system ② that transfers the displacement of the piston outside of the facility. The measuring system consists of six bars going through the cap ④. Three of them are connected with the piston, while the other three are connected to the test cell. The LVDT body is fastened to one of the three rods connected to the test cell, while the LVDT plunger is fastened to the one of the three rods connected to the piston. In this way the differential displacement between the piston and measuring cell is measured by the LVDTs working at ambient temperature.

A pipe flanged at both ends ⑤, connecting the test cell with the upper cap, has been designed in order to assure the desired atmosphere in the pebble bed. The sealing is assured by a flat high temperature gasket between the measuring cell and the pressure pipe and by o-rings in the upper part. A high temperature fitting is used to hold the thermal probe in position and to ensure the sealing. Water-cooled heat exchangers have been designed to keep the temperature below 200 °C where o-rings are used. Furthermore, in order to thermal disconnect the experimental setup and the testing machine two additional heat exchangers are placed around the

lower and the upper rods. The test cell as well as all other components exposed to high temperatures is made of high temperature/low creep materials like Hastelloy X and Nimonic 80A alloys.

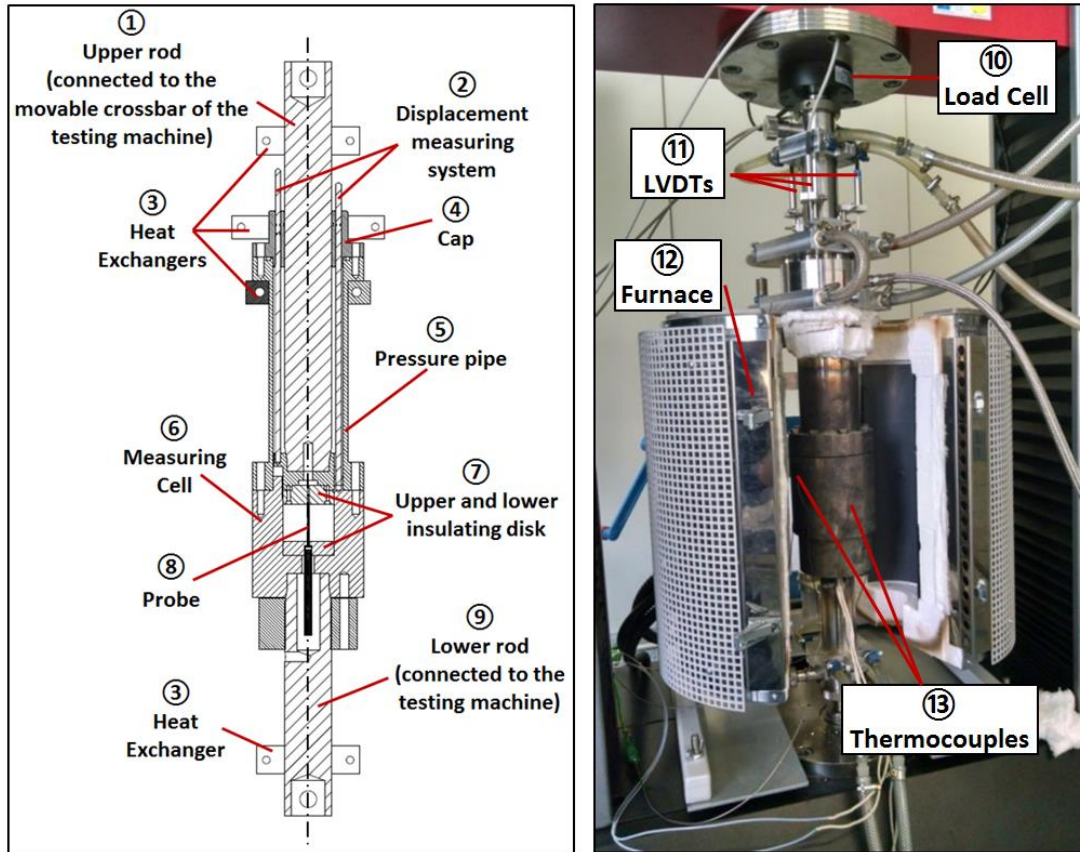


Figure 4-1: Experimental setup for the measurements of ceramic pebble beds' thermal conductivity: cross-sectional cut (left), photograph (right).

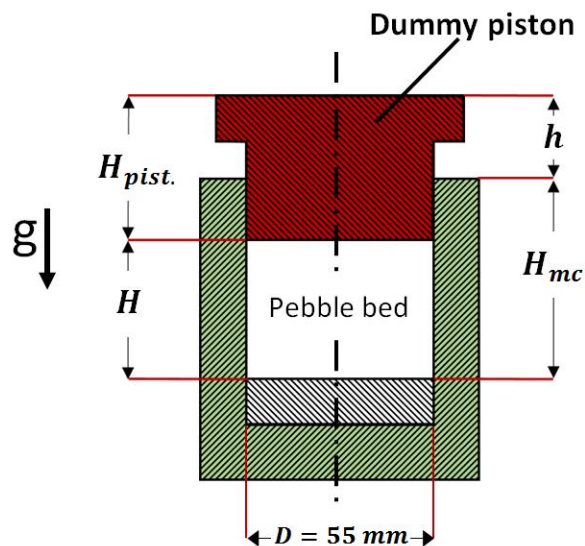


Figure 4-2: Cross-sectional cut of measuring cell with the dummy piston for the evaluation of the initial bed height.

In the present study a 40 mm long probe with an outer diameter of 1.9 mm is used as linear heat source. The thermal probe consists of a heating element and a type K thermocouple enclosed in a thin clad. The thermocouple junction is located at the probe middle length. Great efforts have been made to design a suitable probe. The design is based on the analysis of error sources (see sect. 4.1.1). In Figure 4-3 an image of the installed probe and a schematic drawing of the thermal probe are shown. A 1.9 mm outer diameter INCONEL pipe, with a 0.3 mm wall thickness, is used as external sheath. A Nickel-chromium wire 0.18 mm in diameter is used as resistance heater wire, while aluminium oxide acts as electrical insulator. In the previous works [51], [53]-[55], thermocouples were welded on the heater's surface. In this way, the temperature sensor may be in contact with a pebble or with the gas and the temperature measurement may be affected by the thermocouple position. In the present work the thermocouple is placed within the probe, so that the temperature measurement is not affected by the position of the thermocouple.

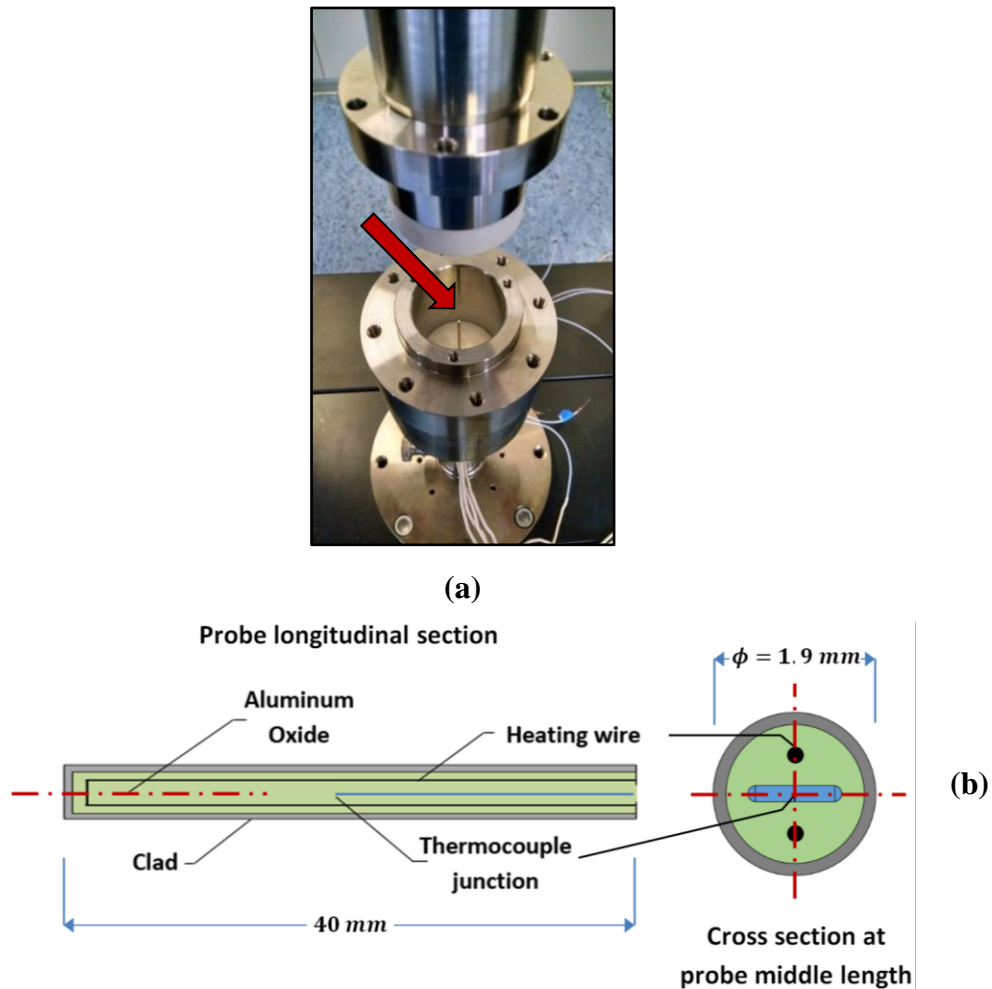


Figure 4-3: Photograph of the installed probe in the measuring cell (a) and cross-sectional cut and dimensions of the probe used in the experiments (b).

After the assembling of the experimental setup, the bed is first evacuated and then filled with the selected gas at the desired pressure. For each investigated material the first experiment is conducted at RT with the selected initial packing factor. Then the measurements are performed at increased temperatures up to 700 °C. During the heating up process the helium atmosphere is kept in the facility. At every investigated temperature the bed is first evacuated and then filled with the selected gas at the desired pressure. Then the facility is allowed achieve the thermal equilibrium, at the selected testing temperature, for several hours. When the difference in relative temperature measured by all thermocouples during a 30 minute period falls below $\Delta T_{30\ min} \ll 1\ ^\circ\text{C}$, the experiment is started. When the measuring cell reaches the designed temperature and thermal equilibrium is achieved, the probe is heated by feeding a constant current to the heating element and the temperature rise of the probe is measured by the enclosed thermocouple. The experimental setup is monitored and controlled by a dedicated LabVIEW program. The heating time is set to 100 s (see sect. 4.1.1), while the current is kept constant by means of a high precision power supply. Figure 4-4 exemplarily shows the characteristic temperature rise of the employed probe. In the figure, the linear region used to calculate the thermal conductivity and the power are also reported.

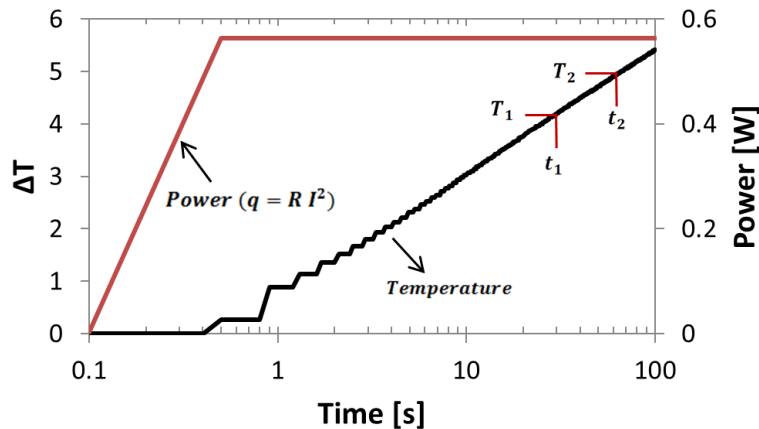


Figure 4-4: Characteristic temporal evolution of the probe temperature due to the applied heating power q .

To obtain a well-defined mechanical state of the bed, at each investigated temperature a mechanical conditioning is executed prior to the thermal conductivity measurements. The mechanical conditioning consists of 3 loading/unloading cycles up to 6 MPa with a loading rate of 1 MPa/min. The effective thermal conductivity at a certain temperature is then measured under a compressive load of 0 and 6 MPa. Figure 4-5 exemplary shows the loading history of the bed for a selected experimental temperature. The red points represent where the thermal conductivity

is measured. The number of loading cycles after the mechanical conditioning varied depending on the thermal conductivity measurements performed. The flow chart of the experiment is reported in Appendix C.

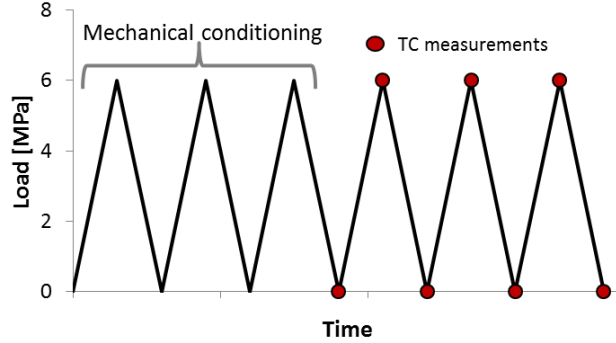


Figure 4-5: Loading history of the pebble bed for a selected temperature.

4.1.1 Probe design and sample size justification

In practical applications several factors contribute to the definition of the sample and probe dimensions. Aim of this work is the investigation of the effective thermal conductivity of ceramic pebble beds under severe conditions (mechanical compression and high temperature). This has influenced the design of the probe in order to withstand such conditions. Due to theoretical approximation and practical considerations the probe method deviates from the ideal linear heat theory. The sources of uncertainty of the method are related to the finite dimension of the probe, the contact resistance at the probe/medium interface and the finite dimension of the sample. The implicit error arising from the truncation of the series approximation (Eq. 3.8) was addressed by Blackwell [91] who demonstrated that this error is less than 1% if

$$\left(\frac{d_p^2}{2 \alpha t} \right)^2 < 0.01, \quad 4.3$$

where d_p is the diameter of the probe, α is the thermal diffusivity of the sample and t the time. The error arising from the series approximation can be minimized either reducing the probe radius or by excluding the early part of the temperature transient for the thermal conductivity calculation. eq. 4.3 suggests that the error is minimized if $t > 10 r^2/\alpha$.

The linear heat source theory refers to a zero radius and infinitely long heat source. Any practical probe differs from this assumption leading to axial heat flow in the probe and in the sample, violating the pure radial heat flow. Blackwell [37] demonstrated that the axial heat flow error is minimized (error < 1 %) for probes with a length L_p to diameter d_p ratio $L_p/d_p > 25$.

He [91] also calculated that to fulfil the radial heat flow assumption the length of the sample L_p should be

$$L_p > \left(\frac{4 \alpha t_h}{0.0632} \right)^{0.5}, \quad 4.4$$

where t_h is the heating time. Rearranged eq. 4.4 yields

$$t_h < \frac{0.0632 L_p^2}{4 \alpha}. \quad 4.5$$

Another source of error is related to the finite radial dimension of the sample. After a sufficiently long time the heat front reaches the boundary of the sample generating a non-linearity in the temperature vs. the logarithm of time graph. The heat is transferred to the boundary walls leading to a fall or a rise of the temperature graph at long times. Anderson and Backstrom [92] theoretically estimated that a finite radial sample dimension cause an error less than 0.1% as long as

$$R_s > 2 (\alpha t)^{0.5}, \quad 4.6$$

or for times t :

$$t < \frac{0.25 R_s^2}{\alpha}, \quad 4.7$$

where R_s is the radial dimension of the sample.

The error sources have been considered in the probe design. The diameter of the probe is kept as small as possible according to the requirements of the linear heat source theory. A 40 mm long probe with an outer diameter of 1.9 mm is used as linear heat source. The L_p/d_p ratio of the selected probe is 21. The sample dimensions, in particular the bed height (equal to the probe length), is the result of a compromise for a reliable measurement of the thermal conductivity with a uniform compressed bed along its axis. A higher value of the bed height would be beneficial for the thermal conductivity measurement, but detrimental to the uniformity of the mechanical compression, see sect. 2.1. The chosen radial dimension of the sample is 55 mm while $H = 40$ mm resulting in a H/D ratio of 0.73.

The measuring time, based on the wire and sample dimensions is calculated according to eq. 4.3, 4.5 and 4.7. Both, short and long times have to be discarded for the calculation of the sample thermal conductivity to avoid significant errors either from truncation, axial heat loss and

boundary effects. The calculated time restrictions over the measuring temperature are reported in Figure 4-6. The material properties of lithium orthosilicate, used to estimate the thermal diffusivity for the evaluation of the time limits, are taken from [93] and reported in Appendix D. According to the results of the calculations the heating time is set to 100 s while, time interval 30-60 s is used to calculate the thermal conductivity of the bed.

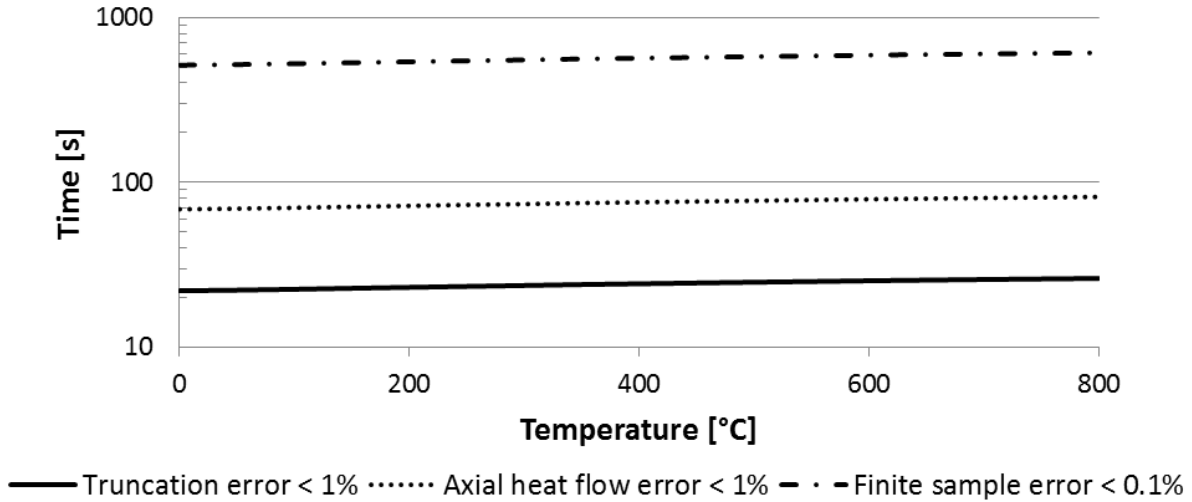


Figure 4-6: Time restrictions for the calculation of the thermal conductivity.

A series of simulations have been carried out with the Finite Element code ANSYS to support the design of the experimental set up. The rotational symmetry of the measuring cell simplifies the FE and hence, one fourth of the measuring cell is simulated. The probe is simulated as one body having the averaged thermal properties (over the volume) of the constituent components, see Appendix E. This avoids resolving details of the probe, since the dimensions of the internal components (heating wire and the electrical insulation) are very small. The lithium orthosilicate bed is simulated as continuum having the effective thermal properties reported in [93], see Appendix D. Figure 4-7 left shows the geometrical model used.

The expected experimental parameters are used to run the simulations. The heating time is set to 100 s with a power of 0.55 W. The period 30-60 s is used to calculate the material thermal conductivity. The adopted heating power correspond to an input current of 0.35 A. As in the real probe, the temperature is recorded in the center of the probe ($r = 0$) at the sample middle length ($L_p/2$). According to the measuring cell dimensions, the radial extension of the sample is 27.5 mm. When simulated, the thermal contact resistance between the probe and the sample is accounted by applying a Heat Transfer Coefficient (HTC) according to the equation reported in

[94]. The thermal properties of the insulating disks (MACOR) are taken from [98]. The symmetry planes as well as the axial and radial boundaries of the model have been considered adiabatic. During the heating time of the probe the heat front does not reach the external radial boundary of the sample. Therefore, the external container made of Hastelloy is excluded from the simulations. Figure 4-7 right exemplary shows the calculated temperature distribution at the end of the heating time ($t = 100s$) for a sample height of 40 mm starting from an initial homogenous temperature of $500^{\circ}C$.

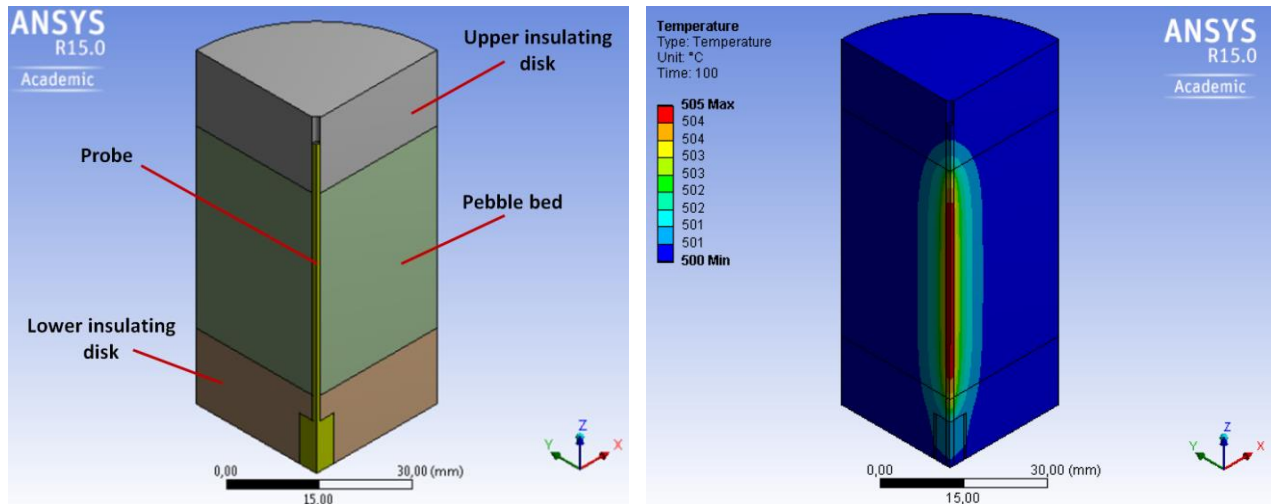


Figure 4-7: Geometrical model (left) and calculated temperature distribution at the end of the heating time (right).

The influences of the sample height and the contact resistance between the probe and the sample have been systematically investigated. Simulations are carried out with a sample height of $H = 50, 40, 30$ and 20 mm, respectively. Figure 4-8 shows the temperature transient at the probe middle length for different bed heights at RT and $500^{\circ}C$. In this case a perfect thermal contact between the probe and the sample is simulated. The curves differ from each other for different bed heights. In particular, reducing the sample height the non-linearity of the temperature vs. the logarithm of time graph, due to the boundary effect, increases. The influence of the upper and lower boundaries increases with decreasing the bed height, resulting in a deviation from the desired pure radial heat flow due to axial heat flow to the boundaries. At RT the influence of the boundaries is clearly visible for a bed height of 20 mm while, at $500^{\circ}C$ this influence attenuates. As reported in Appendix D, at $500^{\circ}C$ the thermal conductivity of the sample is higher than at RT. For this reason, the axial heat flow in the probe is reduced. Hardly any difference in the

temperature rise of the probe can be observed for a sample height of 40 and 50 mm at both temperatures.

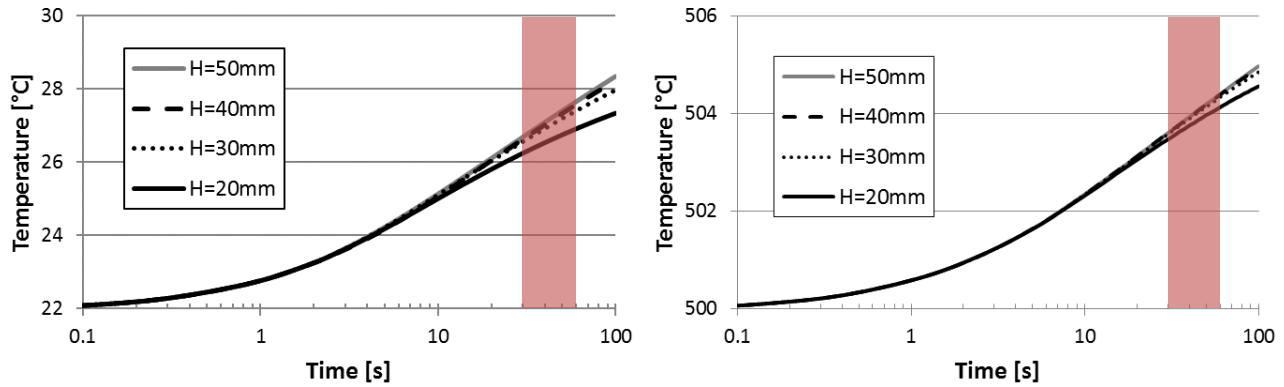


Figure 4-8: Calculated temporal evolution of the probe temperature at RT (left) and 500 °C (right) for different pebble bed heights.

For the bed height of 40 mm a series of simulations are performed with and without thermal contact resistance between the probe and the sample. Figure 4-9 exemplarily shows the influence of the contact resistance at 300 °C. The contact resistance is found to shift the temperature rise to higher temperatures with a slight change of the slope.

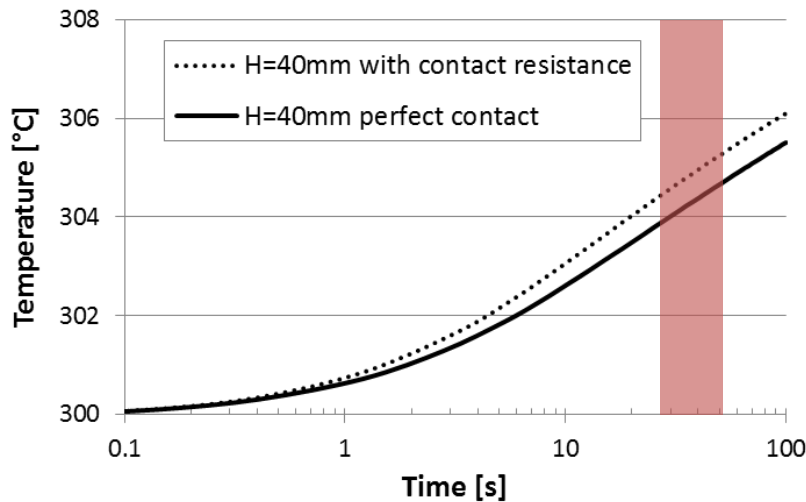


Figure 4-9: Influence of the thermal contact resistance between the probe and the bed on the temperature transient.

In Table 4-1, the computed thermal conductivity values with and without the contact resistance for a bed height of 40 mm are reported. The obtained thermal conductivity values, either with or without the thermal contact resistance, are in good agreement with the values used to run the simulation. The maximum deviation is around 4%. This deviation is not the uncertainty or accuracy of the method.

Table 4-1: Computed thermal conductivity values obtained from the FE simulations.

T [°C]	K pebble bed [W/(m K)]	With thermal contact resistance K computed [W/(m K)]	Without thermal contact resistance K computed [W/(m K)]
22	0.80	0.81	0.82
300	0.90	0.86	0.88
500	1.00	0.96	0.98
700	1.10	1.07	1.08

A homogenous sample temperature, even if highly desired, is rather difficult to achieve in practical applications. In order to study the influence of an uneven temperature distribution a series of simulations have been conducted with a sample height of 40 mm and HTC between the probe and the sample. A non-uniform temperature field has been obtained by applying a constant uniform temperature on the radial external surface of the sample equal to the measuring temperature T_{exp} and a constant uniform temperature (T_b), equal to $T_b = T_{exp} - 20^\circ\text{C}$, on the top and bottom surfaces of the model, see Figure 4-10 left.

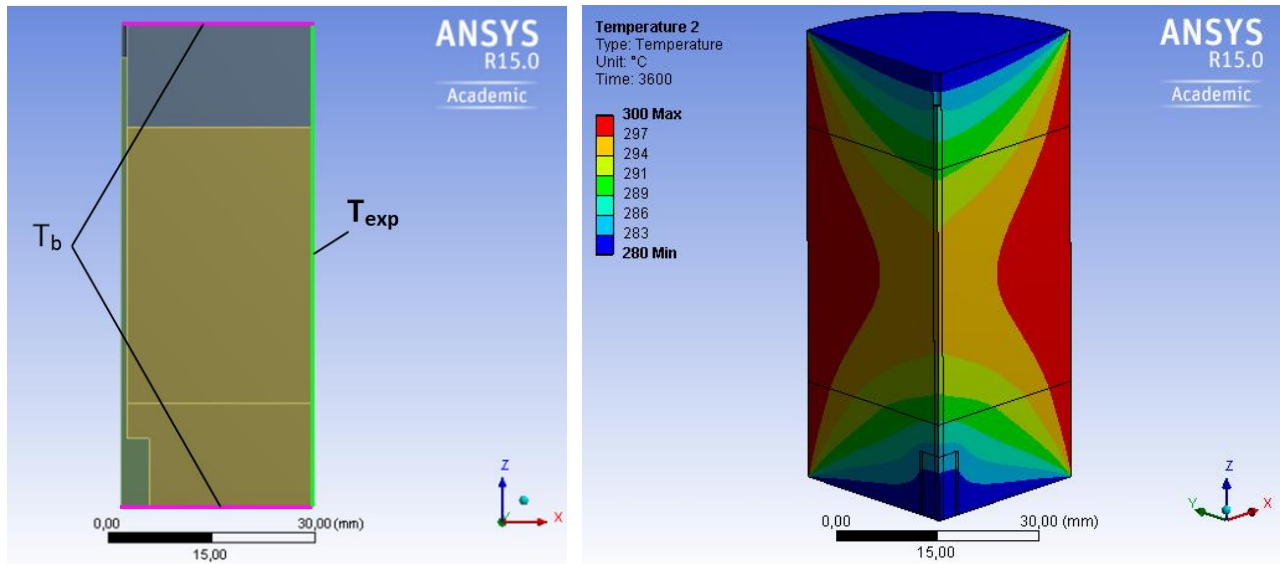


Figure 4-10: Applied temperature boundary conditions (left) and computed temperature distribution (right) at $t = 3600$ s.

The symmetry planes have been considered adiabatic. Three temperatures are investigated $T_{exp} = 300, 500$ and 700°C . The simulations start with a uniform model temperature $T_{start} = T_{exp} - 100^\circ\text{C}$, then the FE model is let to reach the steady state configuration. At $t = 3600$ s the probe is switched on for 100 s with a power of 0.55 W. Figure 4-10 right exemplary shows the

obtained temperature distribution at $t = 3600$ s (right before the heating of the probe), while in Figure 4-11 the computed temperature evolution at the probe middle length is illustrated. Both figures refer to the same simulation conducted at $T_{exp} = 300$ °C. All simulations show an hourglass shaped temperature field, the temperature in the middle of the sample is about 5 °C less than that of the external surface temperature. Nevertheless, the obtained thermal conductivity values are similar to those reported in Table 4-1 for the simulation with thermal contact resistance. The maximum difference is less than 1%. The results of the FE simulations confirm that the chosen geometry is suitable for the measurement of the thermal conductivity of ceramic breeder beds.

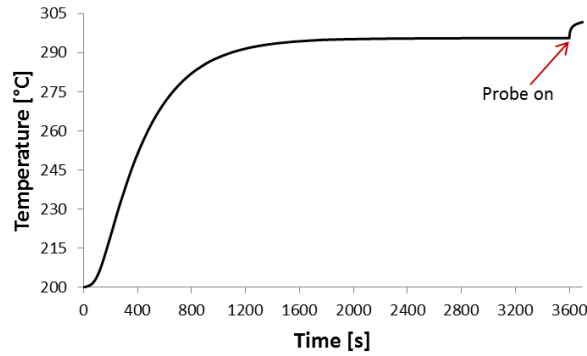


Figure 4-11: Temperature over time at probe middle length.

4.1.2 Evaluation of the uncertainty

The uncertainty on the measured thermal conductivity is assessed following the rules reported in the guide to the expression of uncertainty in measurement (GUM) [99]. The thermal conductivity (k) is not measured directly but is determined by equation 3.15 that involves other quantities:

$$k = \frac{2.3 R I^2}{2\pi S_{10}}. \quad 4.8$$

Here R is the characteristic resistance of the wire [Ω/m], I is the current flowing through heater wire [A] and S_{10} is the slope used to evaluate the thermal conductivity calculated using the temperature vs. the $\log_{10}(t)$ graph.

Assuming that the quantities R , I and S_{10} are uncorrelated, the uncertainty u_k on k is calculated combining the standard uncertainties u_i of $i = R, I$ and S_{10} by using:

$$u_k = \sqrt{\sum \left(\frac{\partial k}{\partial i}\right)^2 u_i^2}. \quad 4.9$$

The uncertainty u_R of R has been estimated to be represented by a rectangular distribution with bounds $\pm 2.5\%$ of the calculated value. The standard uncertainty u_R is then

$$u_R = \frac{5 R}{100 \sqrt{3}}. \quad 4.10$$

The standard uncertainty u_I of I arises from the setting and read back accuracies of the power supply. The setting and read back accuracies are both given as

$$\pm(0.05\% \text{ of setting} + 2.5\text{mA}). \quad 4.11$$

The standard uncertainty u_I is represented by the combination of the standard uncertainties arising from the setting (u_{SA}) and readback (u_{RA}) standard uncertainties. Assuming that the aforementioned accuracies lie with equal probability in the range current value $\pm (0.05\%$ of setting +2.5mA) i.e. a rectangular distribution, the standard uncertainty u_I is given by:

$$u_I = \sqrt{u_{SA}^2 + u_{RA}^2} = \sqrt{4 \left[\left(\frac{\frac{0.05 I}{100} + 0.0025}{\sqrt{3}} \right)^2 + \left(\frac{\frac{0.05 I}{100} + 0.0025}{\sqrt{3}} \right)^2 \right]}. \quad 4.12$$

The standard uncertainty u_S of S_{10} has been quantified by a statistical method. Two slopes, S_1 and S_2 , are derived by the least squares fitting of the temperature vs. the $\log_{10}(t)$ graph in two time intervals $\Delta t_1 = t_2 - t_1$ and $\Delta t_2 = t_4 - t_3$ ($t_1 < t_2 = t_3 < t_4$). Then the average value of both slopes is used to evaluate the thermal conductivity. The standard uncertainty u_S is then calculated by:

$$u_S = \frac{s}{\sqrt{N}}, \quad 4.13$$

where s is the standard deviation of the two slopes S_1 and S_2 while N denote the number of observations ($N=2$).

The combined standard uncertainty is then calculated by means of eq. 4.9 as

$$u_k = \sqrt{\left(\frac{\partial k}{\partial R} \right)^2 u_R^2 + \left(\frac{\partial k}{\partial I} \right)^2 u_I^2 + \left(\frac{\partial k}{\partial S} \right)^2 u_S^2}, \quad 4.14$$

$$\frac{\partial k}{\partial R} = \frac{2.3 I^2}{2 \pi S}, \quad \frac{\partial k}{\partial I} = \frac{2.3 R I}{\pi S}, \quad \frac{\partial k}{\partial S_{10}} = -\frac{2.3 R I^2}{2 \pi S^2}.$$

Assuming the measured thermal conductivity is a normally distributed random variable, the expanded uncertainty U_k of the measured thermal conductivity is obtained by multiplying the combined standard uncertainty (u_k) by a coverage factor K^* :

$$U_k = K^* u_k . \quad 4.15$$

For a level of confidence of 95%, the coverage factor K^* is equal to 2.

For each experiment, the uncertainty of the measured values is calculated combining the standard uncertainties of the input quantities as reported above. The overlap between the uncertainty bands of distinct experiments, performed with the same material assured the consistency of the experiments. Once the consistency between the experiments is proved, the values are averaged and then the standard deviation among experiments is used as indicator of the uncertainty. The values are discarded when the uncertainty bands do not overlap with those of other measurements. For the experimental conditions for which only one experiment is performed, the uncertainty is calculated by combining the standard uncertainties of the input quantities.

4.1.3 Probe calibration

Due to lack of certified reference granular materials with a thermal conductivity in the representative range of ceramic breeder beds, the probe calibration is hardly feasible in the expected operational range. Therefore, the calibration of the probe is carried out with water gel at RT as suggested by the ASTM code [100]. The ASTM standard D5334-08 [100] states that the calibration is especially required for large diameter probes ($d_p > 2.5 \text{ mm}$). The precision and bias of the needle probe method has been investigated by the ASTM committee [101]. The result shows a precision between $\pm 10\%$ and $\pm 15\%$, with the tendency to overestimate the thermal conductivity of the investigated material.

The developed probes are tested to prove their accuracy. As suggested by the ASTM code [100], water stabilized with 5 gr/L of agar is used as calibration standard. Agar is added to the water to prevent free convection. The thermal conductivity of water, reported in the ASTM standard, is 0.607 [W/(m K)] at 25 °C. The two developed probes (named probe 1 and probe 2) are immersed in the water gel at RT. Figure 4-12 left shows the probe immersed in the reference material. Six measurements with two different power levels are performed for each probe. The power levels correspond to a current of 0.35 [A] and 0.25 [A]. The time range 60-180 s is used to calculate the thermal conductivity of the water according to eq. 4.3, 4.5 and 4.7.

The measured thermal conductivity values with their uncertainty are shown in Figure 4-13. The uncertainty is calculated according to eq. 4.14. The overlap between the uncertainty bands of distinct experiments assured the consistency of the performed experiments. The averages of the

measured thermal conductivity values for the probe 1 and probe 2 are 0.656 [W/(m K)] and 0.678 [W/(m K)], respectively. The averaged expanded uncertainty (U_k) on the measurements has been $\pm 7.1\%$ for probe 1 and $\pm 6.2\%$ for probe 2. The power level used is irrelevant for the results of the thermal conductivity measurement. Both probes overestimate the thermal conductivity of water. The relative error is consistent with the precision reported in [100]. In particular, the relative error of probe 1 and 2 is found to be 8% and 12%, respectively.

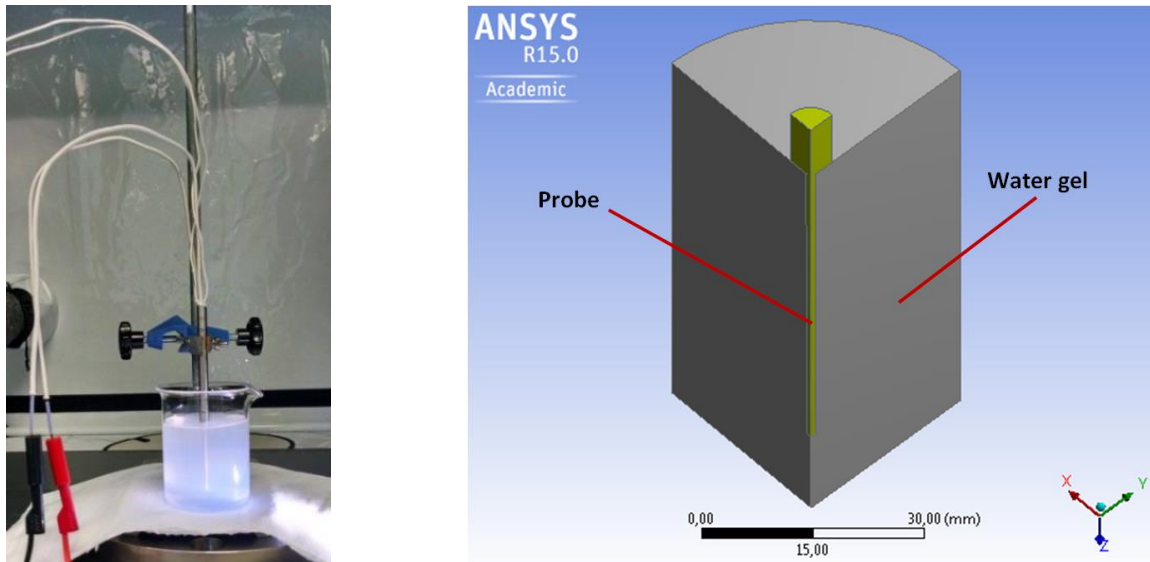


Figure 4-12: Probe being tested with water gel (left) and the corresponding water-gel geometrical model (right).

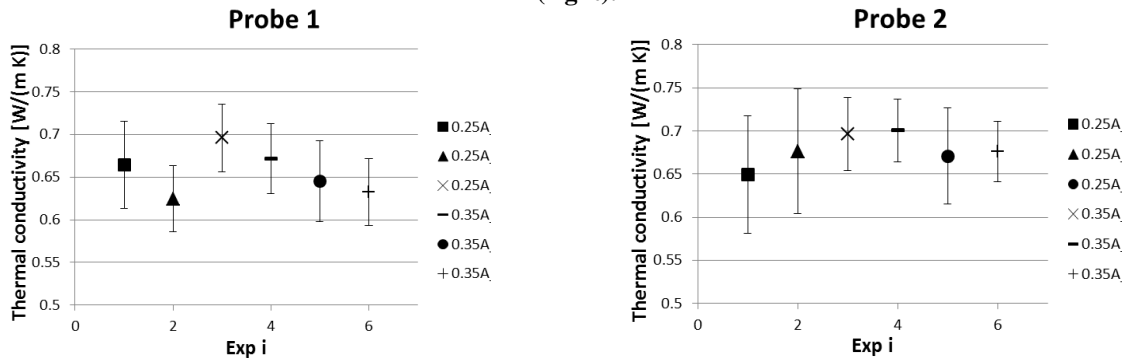


Figure 4-13: Measured thermal conductivity of water with the probe 1 (left) and the probe 2 (right).

The behaviour of the probe in water has been analysed with a complementary FE simulation. The geometry model used is shown in Figure 4-12 right. The thermal conductivity of the water gel has been set to 0.607 [W/(m K)] with a density and a specific heat of 997.4 [kg/m³] and 4179 [J/(Kg K)], respectively. As in the experiment, the time range 60-180 s is used to calculate the thermal conductivity. A power level corresponding to a current of 0.35 [A] is used. The computed thermal conductivity is 0.658 [W/(m K)]. The result of the FE simulation has been

found to be consistent with the experimental findings. The thermal conductivity of the water gel is overestimated of about 8.5%.

Considering the average of the measured values with the average uncertainty, equal to $0.656 \pm 7.1 \%$ and $0.678 \pm 6.2 \%$ for the probe 1 and 2, respectively, the relative error of the developed probes is considered to be acceptable. The lower band values slightly overestimate the thermal conductivity of the water gel. The accuracy of the present measurement system can be therefore confidently considered to be $\pm 10 \%$, with a tendency to overestimate the thermal conductivity.

Chapter 5

Results on the effective thermal conductivity of ceramic breeder pebble beds

This work focuses on the study of the effective thermal conductivity of the EU advanced and reference lithium orthosilicate materials [89]. For comparison with the European lithium silicate based material, also the advanced Japanese lithium metatitanate pebbles are studied. Here, the influence of temperature, compressive load and filling gas type/pressure on the effective thermal conductivity pebble beds is systematically investigated. The influence of the chemical composition (LMT content) is examined as well. At first the investigated materials are introduced then, the experimental results are presented and discussed.

5.1 Investigated materials and experimental conditions

Advanced Ceramic Breeder (ACB) pebble beds characterized by different lithium metatitanate contents are examined. The investigated ACB compositions are $\text{Li}_4\text{SiO}_4 + 20 \text{ mol\% Li}_2\text{TiO}_3$ (20 LMT), $\text{Li}_4\text{SiO}_4 + 25 \text{ mol\% Li}_2\text{TiO}_3$ (25 LMT) and $\text{Li}_4\text{SiO}_4 + 30 \text{ mol\% Li}_2\text{TiO}_3$ (30 LMT). The EU reference (EU Ref.) tritium breeding material ($\text{Li}_4\text{SiO}_4 + 10 \text{ mol\% Li}_2\text{SiO}_3$), fabricated by Schott AG by the melt-spraying method [12], is also investigated. The pebbles fabricated by this method are characterized by a peaked pebble size distribution in the range 0.25-0.65mm. The ACB pebbles are fabricated at KIT by a melt-based process [14]. For comparison with the European lithium silicate based material, the effective thermal conductivity of the advanced lithium metatitanate pebbles (LMT) with lithium excess ($\text{Li}_{4+2x}\text{TiO}_{3+y}$) developed in Japan [102] are studied.

In Figure 5-1 and Figure 5-2, the pebble size distributions of the investigated compositions are reported. For each material the pebble size distribution is obtained from optical micrographs (2D projection of the pebbles) of a representative sub sample of the selected material. As shown in the figures, pebbles fabricated by the melt-based process are characterized by a pebble size distribution in the range 0.25-1.25 mm. Among the ACB materials, the pebble size distribution of

20LMT is the standard size distribution of a typical batch produced by the melt-based process (Figure 5-1b), while the pebble size distributions of 25 and 30 LMT (Figure 5-1c and d) are not frequently obtained by the production process. As shown in Figure 5-2, lithium excess metatitanate pebbles fabricated by the emulsion method [103] are nearly monosized pebbles with a mean diameter of 1.13 mm and diameter variation < 10%.

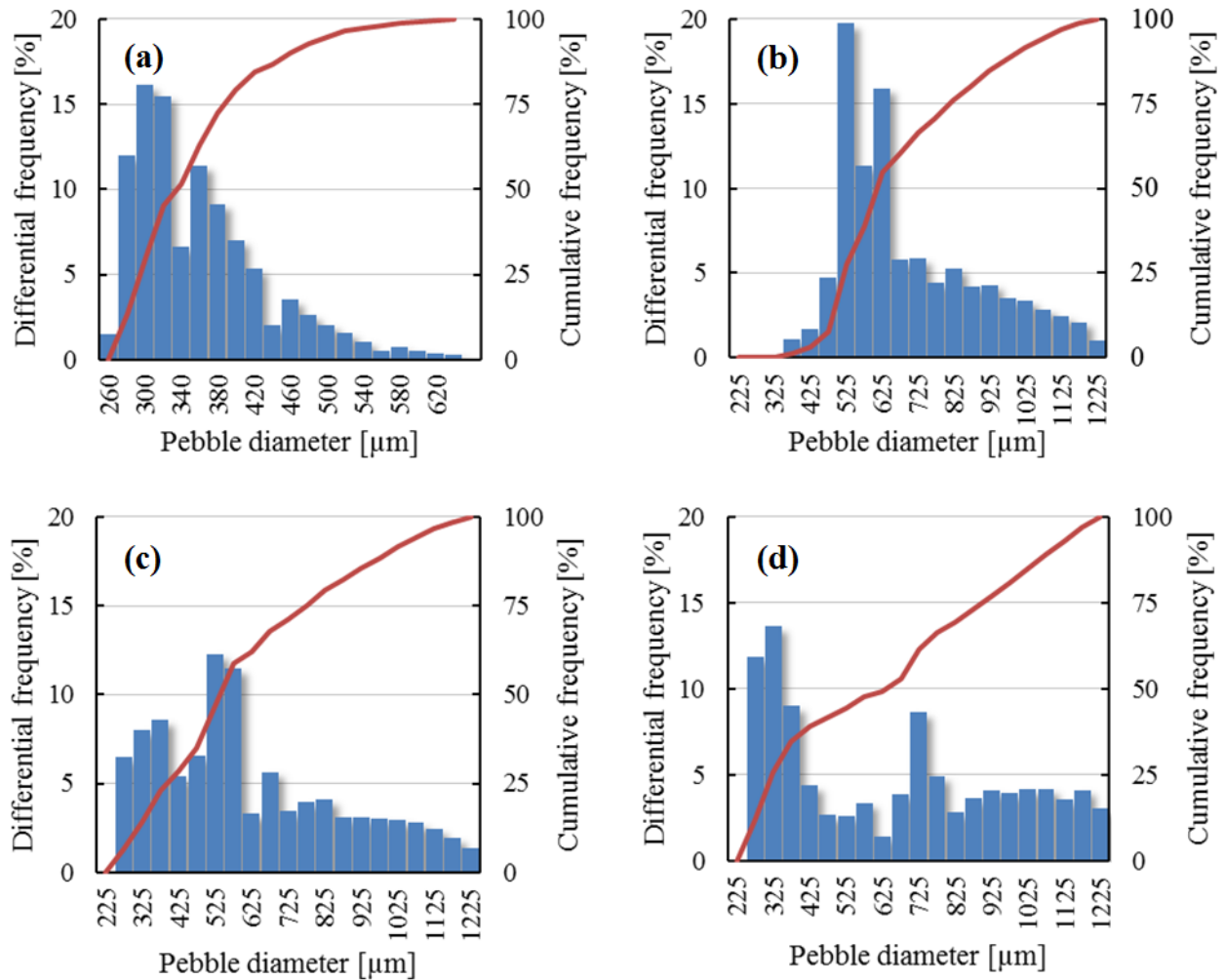


Figure 5-1: Measured size distributions of the investigated breeder materials: EU Ref. (a), 20 LMT (b), 25 LMT (c) and 30 LMT (d).

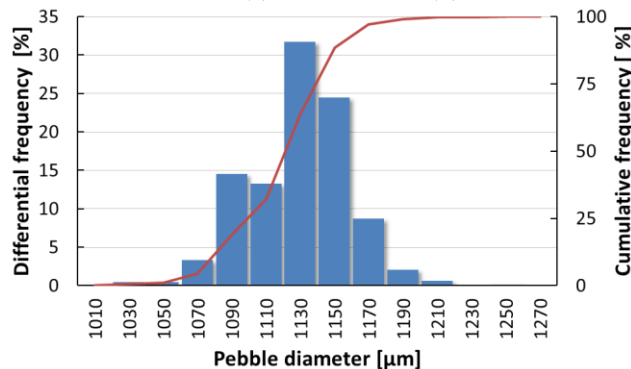


Figure 5-2: Measured size distribution of LMT breeder material.

The physical characteristics of the studied beds and the main experimental conditions are listed in Table 5-1. Approximately 150 g of pebbles are used for the experiments. Before being tested, the pebbles are dried at 300 °C for one hour in a vacuum oven. The experiments are carried out in helium and air atmosphere. Three pressures are investigated, namely 0.12, 0.2, and 0.4 MPa. For the ACB and EU Ref. materials a PF around 64% has been easily achieved by mechanical vibration, whereas a powerful bed vibration has been necessary to attain a PF of 62.5% for LMT pebbles due to their very narrow size distribution.

Table 5-1: Characteristics of the investigated material and main experimental conditions.

ID	Material	Th. Density [g/cm ³]	Pebble diameter [mm]	Density [% Th. Density]	PF [%]	Filling gas	Temp. [°C]
20 LMT	Li ₄ SiO ₄ + 20 mol% Li ₂ TiO ₃	2.54	0.25-1.25	93.0	64.2	He/Air	RT-700 in He RT-600 in Air
25 LMT	Li ₄ SiO ₄ + 25 mol% Li ₂ TiO ₃	2.58	0.25-1.25	93.3	64.2	He	RT-600
30 LMT	Li ₄ SiO ₄ + 30 mol% Li ₂ TiO ₃	2.62	0.25-1.25	93.5	64.2	He	RT-700
EU Ref.	Li ₄ SiO ₄ + 10 mol% Li ₂ SiO ₃	2.40	0.25-0.65	95.1	64.2	He/Air	RT-700 in He RT-600 in Air
LMT	Li ₂ TiO ₃	3.41	1.13	91.2	62.5	He	RT-600

The effective thermal conductivity of a packed bed is dependent on the thermal conductivities of the solid (k_s) and gas (k_g) phases. Figure 5-3 shows the thermal conductivity of Li₄SiO₄ and Li₂TiO₃ as a function of the temperature, as reported in literature [43], [53], [104]-[107]. In this figure, p is the porosity of the studied material. For both materials the thermal conductivity decreases with the temperature tending to level off for temperatures higher than 300 °C, apart from the results of [43] and [107]. Except for the values reported in [43], Li₂TiO₃ shows a slightly higher thermal conductivity than Li₄SiO₄.

In Figure 5-4, the thermal conductivities of unconfined helium and air are reported. Helium and air are selected to simulate the breeder beds atmosphere during normal and accidental conditions and to study the influence of different gas properties on the beds' effective thermal conductivity. The thermal conductivities of the two gases monotonically increase with the temperature. For both gases the thermal conductivity at 800 °C is about 2.5 times the thermal conductivity at RT. Helium has a higher thermal conductivity than air. In the temperature range RT-800 °C the thermal conductivity of unconfined helium is about five times higher than the thermal conductivity of air.

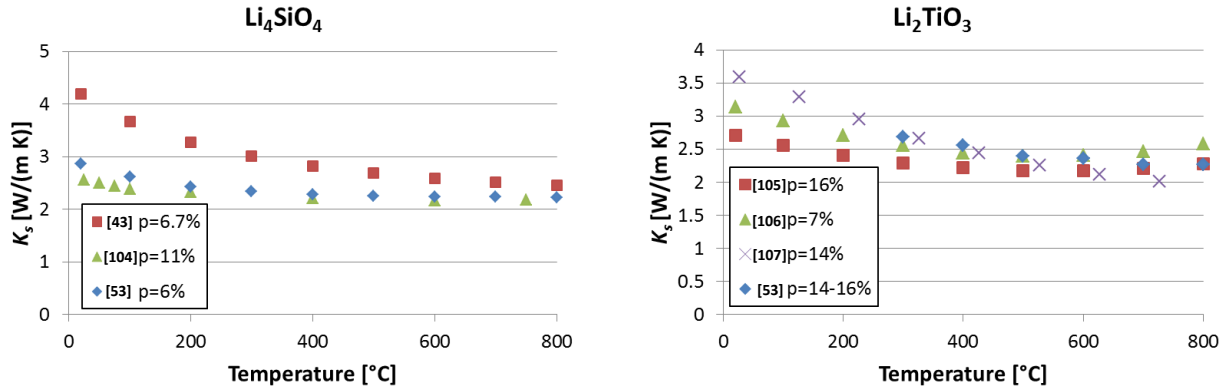


Figure 5-3: Thermal conductivity of the Li_4SiO_4 [43], [53], [104] (left) and Li_2TiO_3 [53], [105]-[107] (right) solid materials with p representing the sample porosity as a function of the temperature.

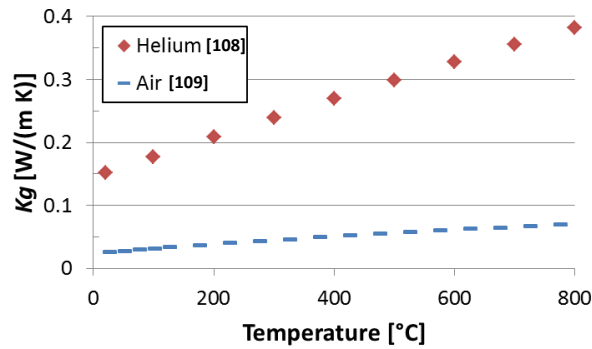


Figure 5-4: Thermal conductivity of helium [108] and air [109].

Figure 5-5 shows the computed k_s/k_g ratio for Li_4SiO_4 and Li_2TiO_3 with helium and air at different temperatures. The k_s/k_g ratio decreases with the temperature for both materials in both atmospheres. Because of the lower thermal conductivity of air, the k_s/k_g ratio in air is significantly higher than in helium.

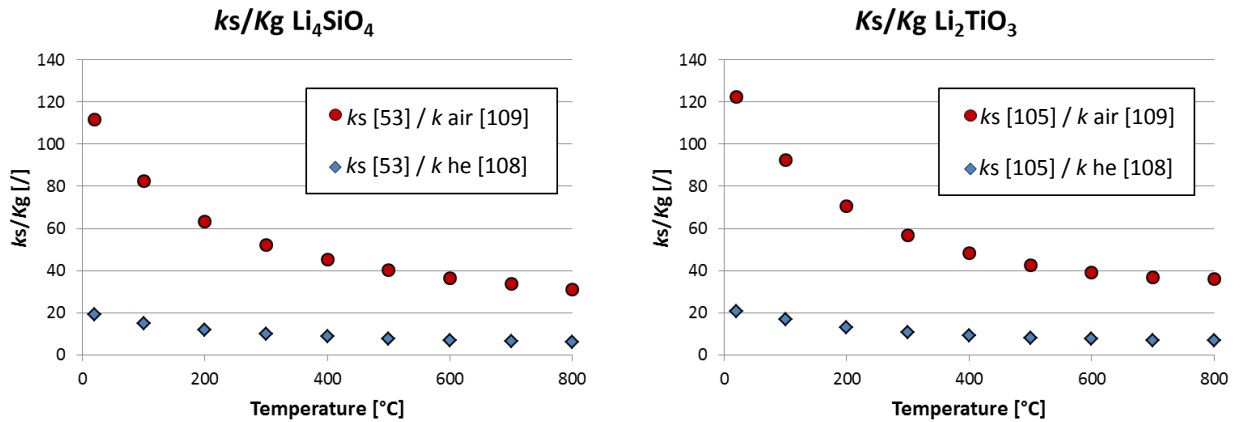


Figure 5-5: Computed solid to gas thermal conductivity ratio of Li_4SiO_4 and Li_2TiO_3 at different temperatures in helium and air.

5.2 Experimental results and discussion

Several experiments are performed for each investigated material. For each experiment fresh pebbles are packed into the measuring cell. Subsequently the measurements are performed at increased temperatures from RT up to 700 °C without repacking of the bed. The loading history reported in Figure 4-5 is applied to the pebble bed at each temperature. The acronyms of the respective materials hereafter used are reported in Table 5-1. For each experiment the uncertainty of the measured values is calculated combining the standard uncertainties of the input quantities R, I and S used in eq. 3.15 to evaluate the effective thermal conductivity. The overlap between the uncertainty bands of distinct experiments, performed with the same material assures the consistency of the experiments. The calculated expanded uncertainty for each measurement ranges between 5 % and 10 % of the measured value. Figure 5-6 exemplarily shows the consistency of the measured effective thermal conductivity of 20 LMT in different experiments. Since the influence of the compressive load has been found to be small (later discussed), in this figure the averaged values between compressed and uncompressed bed with the associated uncertainty are reported for each performed experiment. If the experiments are consistent, the measured values are averaged and the standard deviation among experiments is used as indicator of the uncertainty.

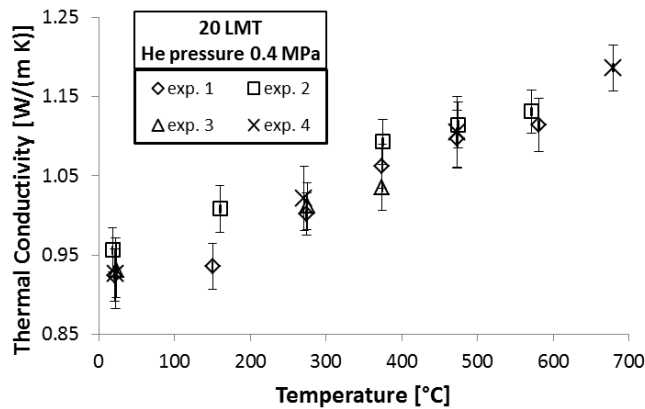


Figure 5-6: Consistency between experiments of the measured effective thermal conductivity of 20 LMT pebble bed as a function of the temperature for He at 0.4 MPa.

The influence of the compressive load on the effective thermal conductivity is shown in Figure 5-7 and Figure 5-8. In the figures, the measured effective thermal conductivities of the investigated compositions are reported as a function of the temperature for compressive loads of 0 and 6 MPa, in helium and air at 0.4 MPa.

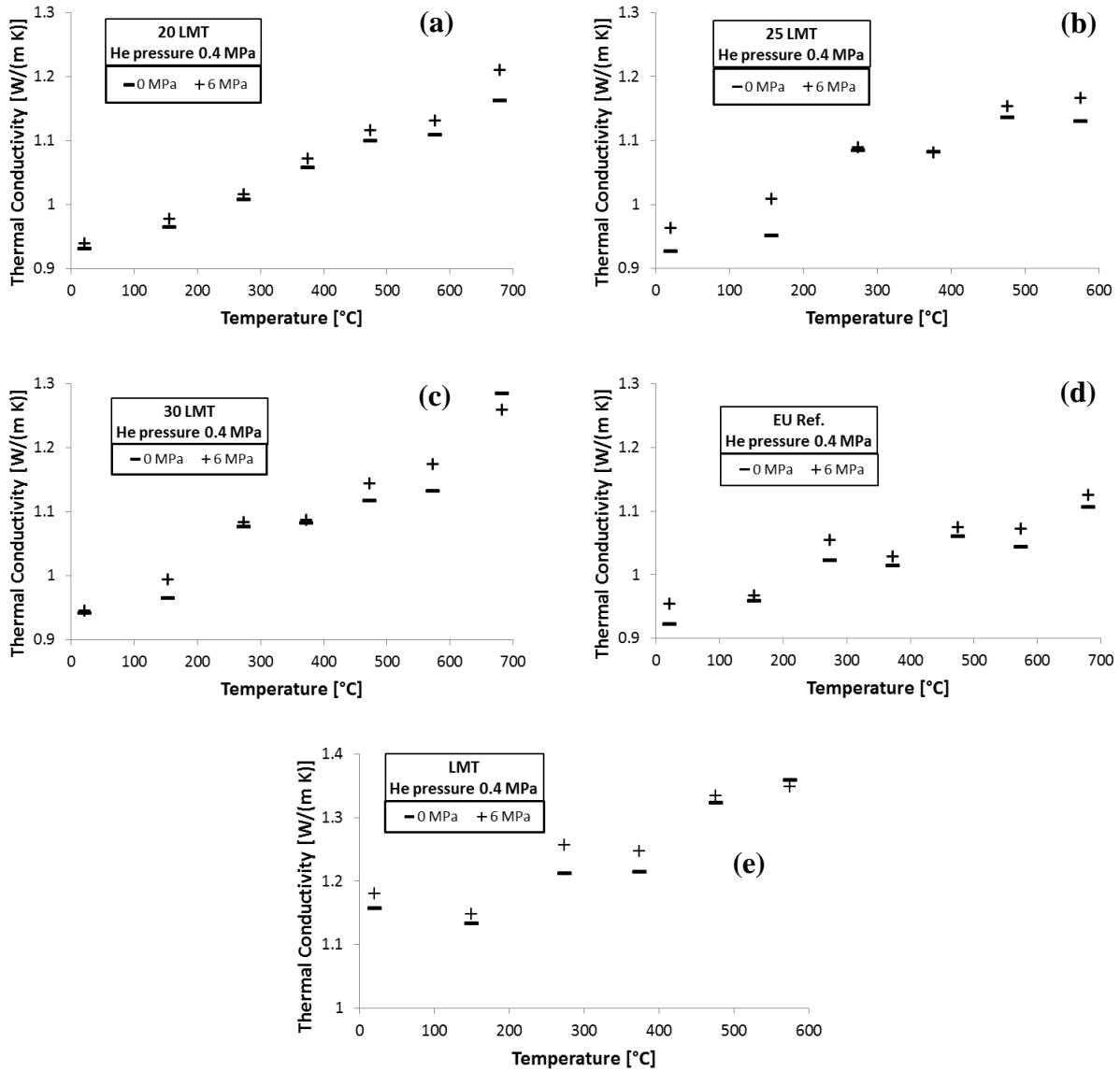


Figure 5-7: Measured effective thermal conductivity as a function of the bed temperature for 20 LMT (a), 25 LMT (b), 30 LMT (c), EU Ref. (d) and LMT (e) in He at 0.4 MPa and compressive loads of 0 and 6 MPa.

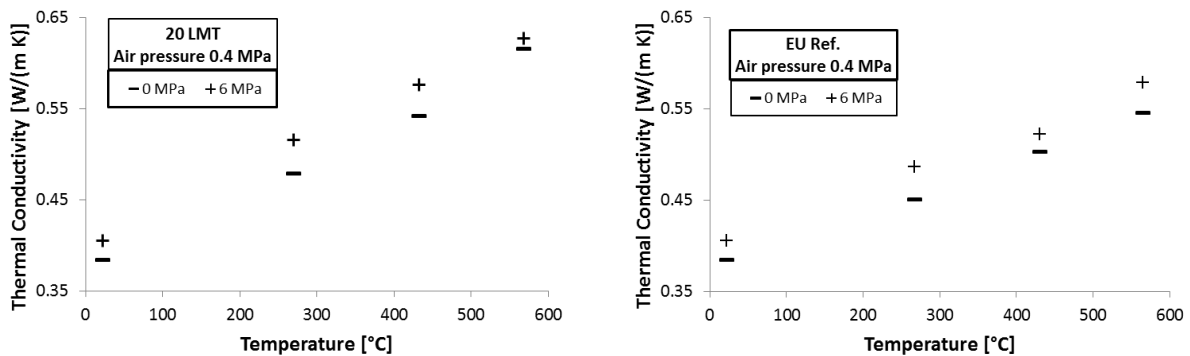


Figure 5-8: Measured effective thermal conductivity as a function of the bed temperature for 20 LMT (left) and EU Ref. (right) in air at 0.4 MPa and compressive loads of 0 and 6 MPa.

At all investigated temperatures and pressures, a slight increase of the effective thermal conductivity with the applied compressive load is observed for all investigated materials. For ceramic beds in helium, the increase in the bed conductivity with the compressive load is expected to be low due to the small solid to gas thermal conductivity ratio. According to the decrease of the k_s/k_g ratio with the temperature (Figure 5-5), the influence of the compressive load is found to be more pronounced at low temperatures with the tendency to vanish at high temperatures. Figure 5-9 exemplarily shows the influence of the compressive load, reported as percentage increase of the bed's effective thermal conductivity for the EU Ref. material as a function of the temperature in helium and air at different pressures. The influence of the compressive load is more evident when air is used as filling gas, although the increase of the thermal conductivity at RT in air is less than 8%. The more pronounced influence of the mechanical compression in air is consistent with the higher k_s/k_g ratio. The gas pressure, in the investigated range, namely 0.12-0.4 MPa, has no influence on the load dependency of the effective thermal conductivity.

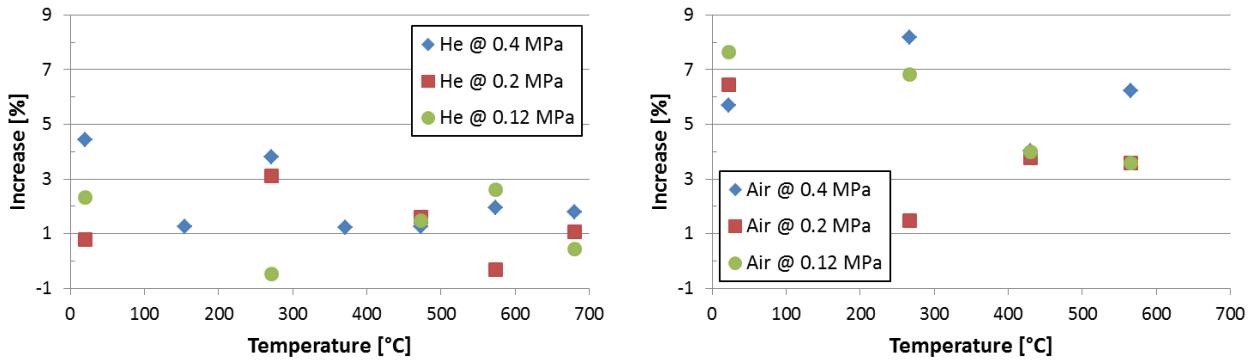


Figure 5-9: Percentage increase of the bed effective thermal conductivity due compressive load for EU Ref. material in helium (left) and air (right) as a function of the temperature.

In Figure 5-10, the measured effective thermal conductivities of the investigated compositions as a function of the temperature in helium at 0.4 MPa are compared. The figure shows the averaged values of the effective thermal conductivities of compressed and uncompressed beds with the associated uncertainty. The current reference correlation for EU Ref., first proposed by Dalle Donne et al. [50] and later extended by Reimann et al. [53] with a term taking into account the bed deformation ε [%], is reported for comparison. An increase of the effective thermal conductivity with the temperature is observed for all investigated compositions. The increase amounts to around 30 % and 20 % for the ACB and the EU Ref. materials, respectively, in the temperature range RT-700 °C. Compared to the reference

correlation, higher values are determined for the thermal conductivity of the EU Ref. material at low temperatures. The results show no significant influence of the chemical composition of the solid material on the bed's effective thermal conductivity. Compared to the EU Ref. material the thermal conductivity of the ACB materials is observed to be slightly higher at high temperatures.

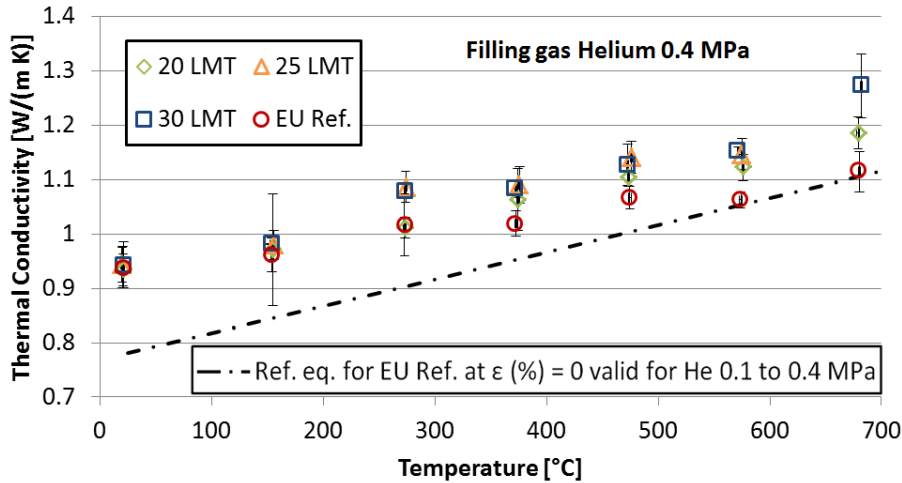


Figure 5-10: Comparison of the measured effective thermal conductivities for the investigated compositions in helium at 0.4 MPa as a function of temperature and comparison with the current reference correlation [53].

The effect of the filling gas is depicted in Figure 5-11 in which the bed thermal conductivities in helium and air at 0.4 MPa are compared. In the temperature range 300-700 °C, the investigated materials show a severe reduction of around 50 % of the effective thermal conductivity when air is used as a filling gas. In air the temperature increase from RT to 600 °C results in an increase of about 60 % of the effective thermal conductivity for beds with lithium metatitanate as a second phase. For the EU Ref. material, the increase of the effective thermal conductivity is about 40 % for the same temperature range in air.

Figure 5-12 exemplary shows the ratio between the effective thermal conductivity of the beds and the thermal conductivity of unconfined helium and air as a function of the temperature. The graph refers to the EU ref. material in helium and air at 0.4 MPa, similar values are obtained for the other investigated materials. The effective thermal conductivity of the beds is about 4 times the thermal conductivity of unconfined helium and about 10 times the thermal conductivity of unconfined air (averaged values over the temperature range RT-700 °C). This highlights the contribution of the solid material on the bed effective conductivity. Both curves decrease with the temperature, accordingly with the dependence on temperature of the solid material thermal

conductivity reported in Figure 5-3. In the temperature range RT-300 °C the ratio shows a 30% reduction, while in the range 300-700 °C the reduction is around 15%.

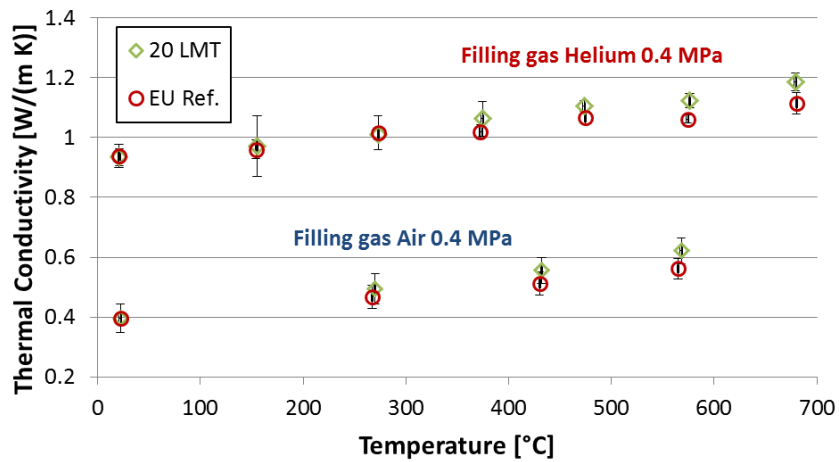


Figure 5-11: Measured effective thermal conductivity as function of temperature for different filling gas.

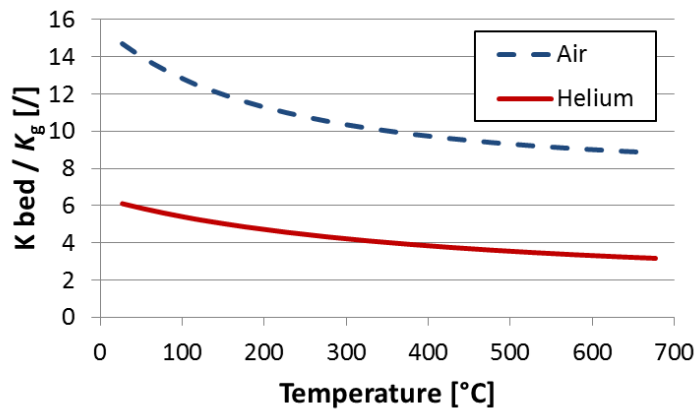


Figure 5-12: Computed bed to gas thermal conductivity ratio in air and helium as function of the temperature.

The measured effective thermal conductivities for pure LMT in helium at 0.4 MPa are compared with the results of EU Ref. (pure silicate) in Figure 5-13. The effective thermal conductivity of pure lithium metatitanate pebble beds is approx. 20 % higher than that of the EU Ref. material. This underlines the impact of the solid material. In this study, the beneficial influence of the LMT content in the ACB material on effective conductivity is partially masked by the scattering of the experimental data. Moreover, to estimate the expected increase in terms of effective thermal conductivity due to the LMT content, we may assume that the increase of the thermal conductivity is only due to the different thermal properties of the solid material (no influences of pebble size/shape and PF) and that the increase is linear with the LMT content. In this case a LMT content of 30 mol% results only in an increase of about 6 %.

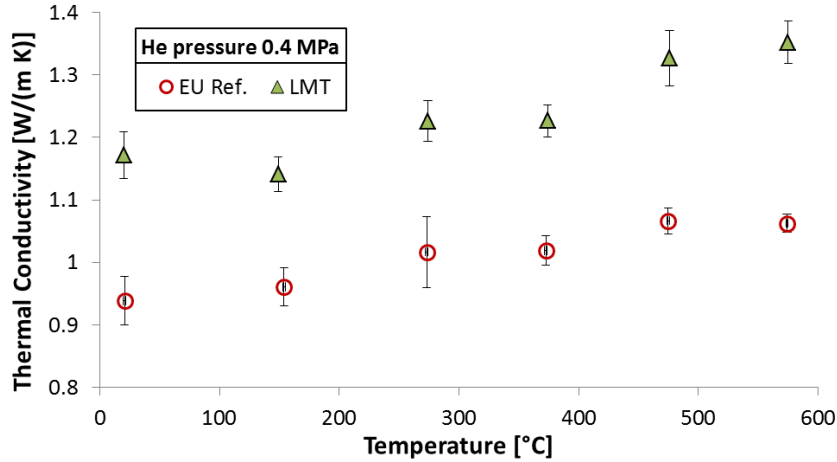


Figure 5-13: Measured effective thermal conductivity of LMT compared to the EU Ref. material as a function of temperature.

Figure 5-14, Figure 5-15 and Figure 5-16 show the pressure dependence of the measured effective thermal conductivities in helium and air, respectively as a function of temperature for helium pressures of 0.12, 0.2 and 0.4 MPa. All investigated materials exhibit a dependence of the effective thermal conductivity on the gas pressure if helium is used as filling gas. The halving of the helium pressure results in a slight reduction (around 5%) of the effective thermal conductivity, while the reduction of the helium pressure from 0.4 to 0.12 MPa leads to a reduction of the bed's effective thermal conductivity of about 10 %. When air is used as a filling gas the pressure dependence of the thermal conductivity is reduced, because helium molecules have a larger mean free path compared to air molecules. By using air instead of helium, the onset of the Smoluchowski effect is shifted to lower pressures (as with air a lower pressure is needed for the mean free path of the gas molecules to become comparable with the gap dimension, see sect. 2.2). Figure 5-17 exemplarily show the normalized increase of the bed's effective thermal conductivity due to the increase of the gas pressure from 0.12 to 0.4 MPa for 20 LMT in air and helium atmospheres as a function of the temperature. In helium, the increase of the thermal conductivity of the bed with the increase of the gas pressure is amplified by the temperature increase due to the increase of the mean free path of the filling gas molecules, which shifts the transition regime to higher pressures (see sect. 2.2). The pressure dependence in helium, together with the limited dependence in air, indicates that in breeder beds the gas is in the upper part of the transition regime ($0.01 < K_n < 0.001$). This Knudsen range corresponds a characteristic gap size ranging between a few μm to about $100 \mu\text{m}$.

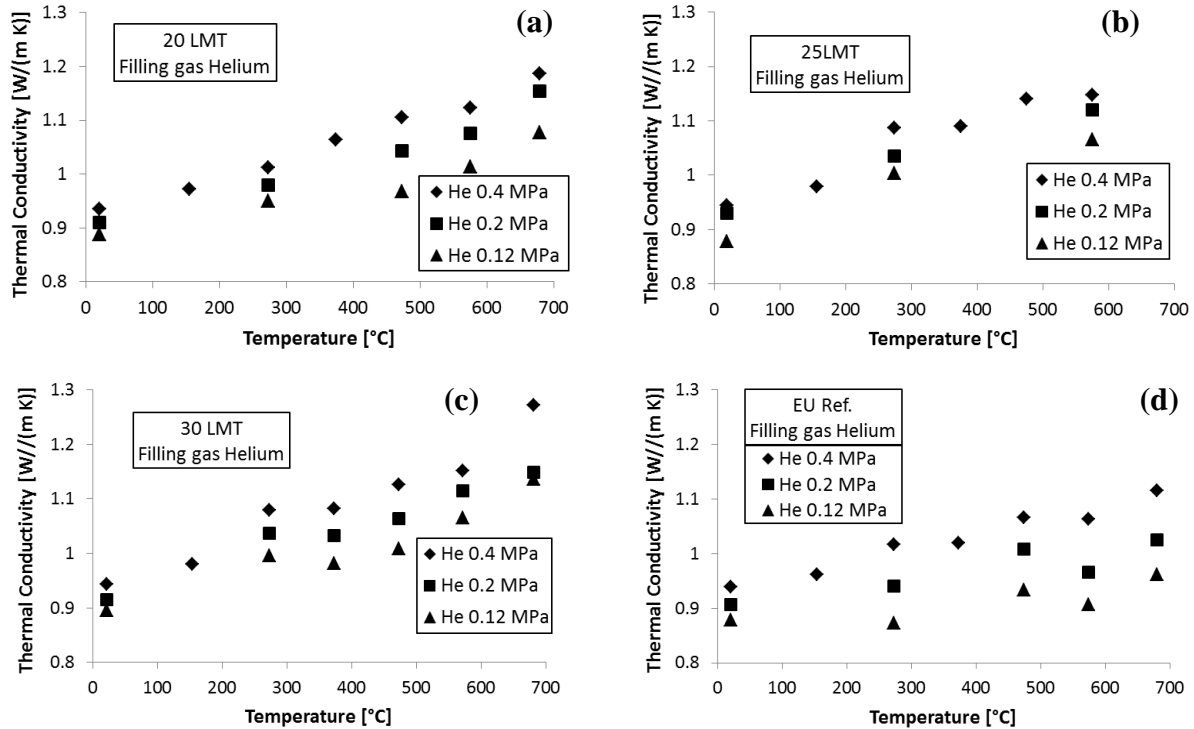


Figure 5-14: Measured effective thermal conductivity of 20LMT (a), 25LMT (b), 30LMT (c), EU Ref. (d) pebble beds in helium as a function of the temperature for different gas pressure.

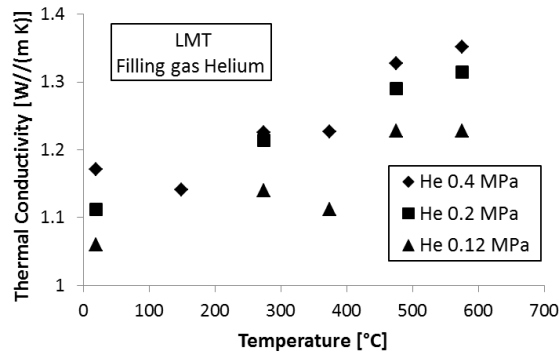


Figure 5-15: Measured effective thermal conductivity of LMT pebble bed in helium as a function of the temperature for different gas pressure.

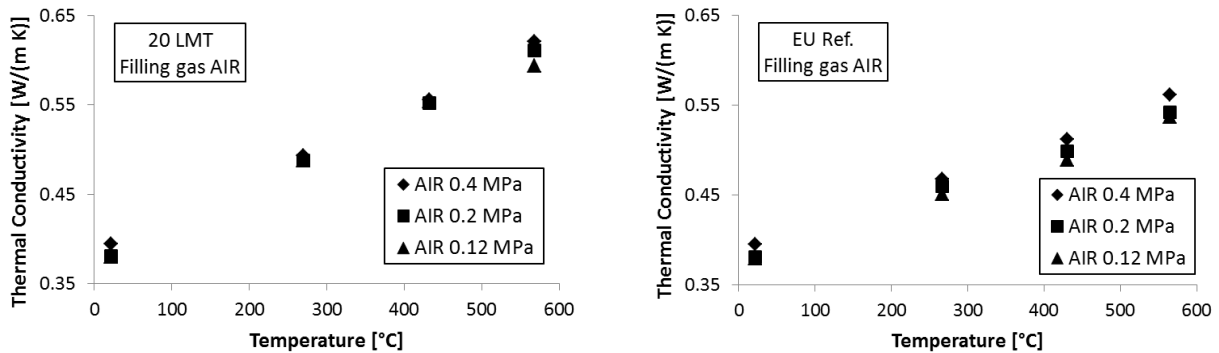


Figure 5-16: Measured effective thermal conductivity of 20LMT (left) and EU Ref (right) in air as a function of the temperature for different gas pressure.

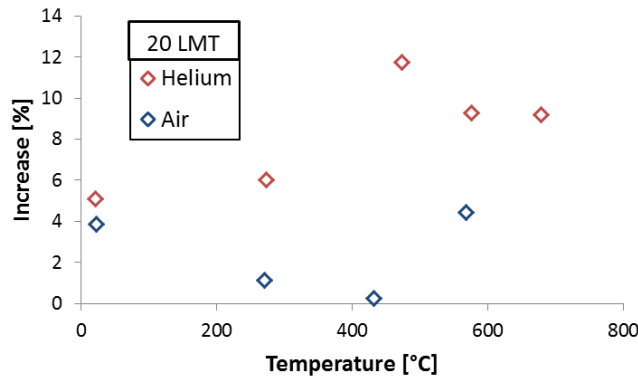


Figure 5-17: Percentage increase of the bed effective thermal conductivity due to the increase of the gas pressure from 0.12 to 0.4 MPa for 20 LMT.

The measured effective thermal conductivities for the compressed EU Ref. material in helium at 0.12, 0.2 and 0.4 MPa are compared with literature data in Figure 5-18. The literature values refer to uncompressed beds with flowing (at very low velocity) [50] and stagnant [57] helium. Both transient (Transient Plane Source) [57] and steady state [50] methods are used. Helium at atmospheric pressure is used in [57], while in [50] the helium pressure varies in the pressure range 0.1-0.3 MPa. In contrast to the outcomes of the present study, no influence of the helium pressure on the thermal conductivity of the pebble bed is found in [50].

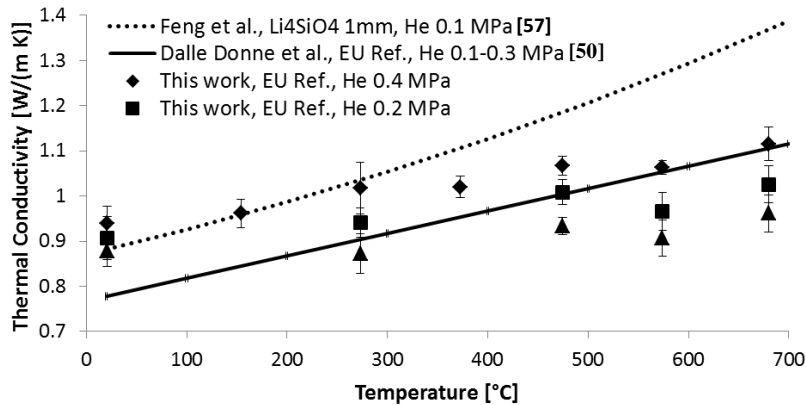


Figure 5-18: Measured effective thermal conductivities in He at 0.12, 0.2 and 0.4 MPa, comparison with literature values

Considering the experimental standard deviation ($4\% < \sigma_{95\%} < 6\%$), for temperatures above 300 °C the results for helium at 0.4 and 0.2 MPa are in good agreement with those obtained in [50]. Higher values are observed at low temperatures, partially due to the effect of the compressive state induced by the mechanical conditioning. As mentioned before, the effect of the compressive load is more expressed at low temperatures. Because of the helium pressure dependency observed in this study, lower values are obtained at high temperatures in helium at

0.12 MPa. The increase of the effective thermal conductivity with the temperature is confirmed, though for all investigated pressures, a weaker temperature dependence is observed in comparison with [50]. Higher thermal conductivity values, especially at high temperatures, were reported in [57] in comparison with the results of [50] and the present study. The reason can be attributed to the different measured methods used in [50] and [57]. Another possible reason may originate from the different pebble sizes. Monosized Li_4SiO_4 pebbles with a diameter of 1 mm were used in [57], while in [50] and in this study, polydispersed Li_4SiO_4 pebbles are investigated. Furthermore, even if in both studies the same materials are investigated, they are produced by similar processes but different facilities that may result in different physical characteristics of the pebbles.

Regarding the thermal conductivity of LMT beds a good agreement with literature values [55] is observed. However, it should be noted that a different pebble size and different physical characteristics of the pebbles were used in [55].

The helium pressure dependence observed in this work is consistent with previous investigations [44], [49], [51], in which the effect of the filling gas pressure was assessed. These reports agree that the effective thermal conductivity of the bed is strongly influenced by the filling gas pressure in the pressure range 0.001-0.1 MPa. Furthermore, the dependence on the helium pressure is drastically reduced, although still present, for pressures above 0.1 MPa.

As result of the experimental campaign, the following empirical correlations are suggested for the calculation of the effective thermal conductivity of the European advanced and reference pebble beds as a function of temperature in helium and air at 0.4, 0.2 and 0.12 MPa.

$k [\text{W}/(\text{m K})] = 9.27 \cdot 10^{-1} + 4.17 \cdot 10^{-4} T [^\circ\text{C}]$	He @ 0.4 MPa		5.1
$k [\text{W}/(\text{m K})] = 9.12 \cdot 10^{-1} + 3.37 \cdot 10^{-4} T [^\circ\text{C}]$	He @ 0.2 MPa	ACB	5.2
$k [\text{W}/(\text{m K})] = 8.79 \cdot 10^{-1} + 3.01 \cdot 10^{-4} T [^\circ\text{C}]$	He @ 0.12 MPa	$20^\circ\text{C} \leq T \leq 700^\circ\text{C}$	5.3
$k [\text{W}/(\text{m K})] = 9.31 \cdot 10^{-1} + 2.59 \cdot 10^{-4} T [^\circ\text{C}]$	He @ 0.4 MPa		5.4
$k [\text{W}/(\text{m K})] = 9.02 \cdot 10^{-1} + 1.66 \cdot 10^{-4} T [^\circ\text{C}]$	He @ 0.2 MPa	EU Ref.	5.5
$k [\text{W}/(\text{m K})] = 8.63 \cdot 10^{-1} + 1.17 \cdot 10^{-4} T [^\circ\text{C}]$	He @ 0.12 MPa	$20^\circ\text{C} \leq T \leq 700^\circ\text{C}$	5.6
$k [\text{W}/(\text{m K})] = 3.77 \cdot 10^{-1} + 4.09 \cdot 10^{-4} T [^\circ\text{C}]$	Air ACB	$20^\circ\text{C} \leq T \leq 600^\circ\text{C}$	5.7
$k [\text{W}/(\text{m K})] = 3.78 \cdot 10^{-1} + 2.93 \cdot 10^{-4} T [^\circ\text{C}]$	Air EU Ref.	$0.12 \text{ MPa} \leq \text{Air p.} \leq 0.4 \text{ MPa}$	5.8

The proposed equations result from the linear fitting of the averaged thermal conductivity values between compressed and uncompressed beds of the investigated materials. The equations are affected by an uncertainty of $\pm 10\%$. The contribution of the compressive load is not explicitly reported in the equations to emphasise the fact that the influence of the compressive load is small for densified beds. Moreover, designers need to know the thermal conductivity as a function of the bed strain ε (%) and not as a function of the compressive load. Considering that the influence of the load, and consequently of the bed strain, is found to be small, its contribution can be neglected. Furthermore, even if the bed deformation (mm) is measured during the experiments, the evaluation of ε (%) is only possible at RT when the initial bed height is known. ε (%) at high temperatures can only be evaluated assuming the initial bed height at RT as reference for each temperature. Yet in doing so, the thermal expansion of the experimental setup as well as of the bed is neglected and consequently the evaluated ε (%) is not representing the real packing state of the bed.

5.3 Summary

The effective thermal conductivity of compressed ceramic pebble beds has been measured using the hot wire method. The studied temperature range covers the prototypical operating temperatures of the ceramic breeder materials. Experiments have been performed in helium and air atmospheres in the pressure range 0.12-0.4 MPa at a compressive load up to 6 MPa for an initial packing factor of the beds of approx. 64 %.

No significant influence of the chemical composition of the solid material is observed between the European reference and advanced breeder materials. Instead, the effective thermal conductivity of pure lithium metatitanate pebble beds is approx. 20 % higher than that of the EU reference material, showing a clear influence of the solid material. An increase of the effective thermal conductivity with the temperature is recorded at all investigated pressures and for both gas types. The influence of the compressive load on the bed's effective thermal conductivity is marginal. All investigated materials exhibit a pressure dependence of the effective thermal conductivity in helium, while no pressure dependence of the thermal conductivity is observed in air. The results show that in the accidental case of leakage in the breeding zone, associated with air ingress in the breeder beds, the effective thermal conductivity of the beds will be severely reduced. Equations for the evaluation of the effective thermal conductivity for EU advanced

ceramic breeder and reference breeder materials are proposed with an uncertainty within a $\pm 10\%$ threshold.

Chapter 6

Validation study of cyclic behaviour of pebble beds

A blanket module will experience cycling loading due to the burn pulses of the plasma. Due to the temperature gradients and a mismatch of the thermal expansion coefficients between the beds and the structural materials, a cyclic compressive load will arise on the breeder beds. Only few studies about the influence of the cyclic loading on the mechanical behaviour of pebble bed assemblies exist [66], [70], [81]. The existing numerical studies [70], [81] refer to monosized pebble assemblies bounded by elastic walls. The initial packing factor used (about 60%) is actually below the reference value for the solid BB concept. Furthermore, in the EU solid BB concept, polydispersed beds are used.

In this chapter, a numerical investigation of polydispersed pebble assemblies with periodic boundary conditions subjected to cyclic loading is presented. To provide a representative result for the EU BB, an initial PF of approx. 64% has been used. The results are compared with the experimental outcomes of the UCTs performed during the thermal conductivity experimental campaign.

6.1 Numerical model and boundary conditions

In this study [110], the existing in-house KIT-DEM code [74]-[78] has been slightly modified to simulate cyclic loading with the stress σ_z as the driven parameter. The assemblies consist in 5000 perfect spherical particles packed, in periodic configuration, in a virtual box using the Random Close Packing (RCP) algorithm [80]. The assemblies generated by this algorithm accurately reproduce the packing structure obtained in packing experiments [111]. The contacts between pebbles and between the pebbles and the boundaries are considered to be purely elastic with normal and tangential interactions. The normal force is evaluated by the Hertzian contact law while the tangential interaction is modelled as a linear elastic force proportional to the tangential displacement unless the Coulomb condition is exceeded. To account for energy

dissipation, artificial damping is introduced. The particles' motion, resulting from the calculated contact forces acting on them, is obtained by the numerical integration of the Newton-Euler equations. PBCs allow to use a comparably low number of pebbles to achieve the representative mechanical behaviour of the specimen by avoiding the wall effects on the packing structure of the assembly. The assemblies are generated with a PF of approx. 64%, consistent with the reference value of the actual EU BB design.

Figure 6-1a exemplarily illustrates an assembly of polydispersed pebbles packed into the virtual cubic box. The pebbles in blue reported in Figure 6-1b represent the boundary pebbles simulating the periodic boundary conditions.

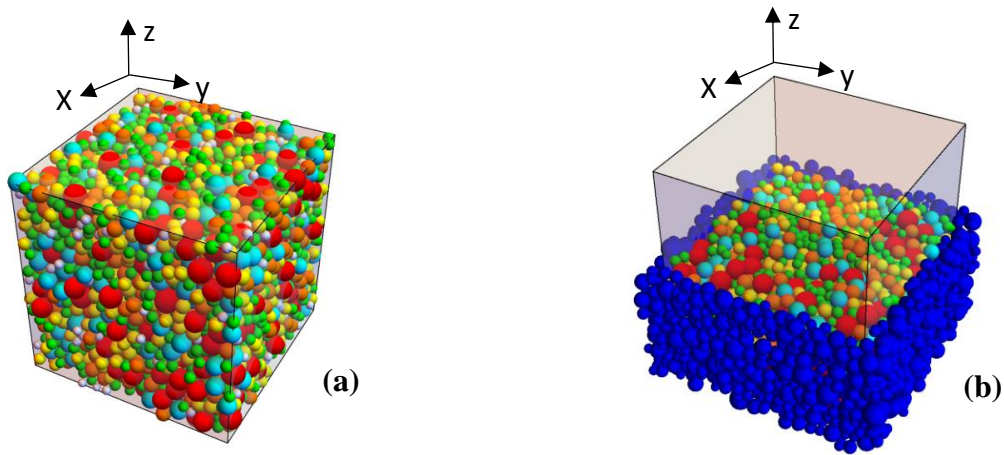


Figure 6-1: Polydispersed pebbles packed into the virtual cubic box (a), assembly with boundary pebbles (b).

The assemblies are generated with the actual pebble size distributions of the EU Ref. and of the three modified breeder ceramic compositions reported in Figure 5-1. For each investigated composition an assembly with a PF close to the experimental value is generated. The assemblies are subjected to cyclic loading simulating the experimental uniaxial compression tests. Starting from the stress-free configuration, generated by the RCP algorithm, the assemblies are progressively loaded up to a defined maximum stress ($\sigma_z = \sigma_{\max}$). After the loading, the assemblies are unloaded by gradually reducing σ_z until the stress-free configuration, $\sigma_z \approx 0$, is reached. As in the experiments the assemblies are compressed by five loading cycles. During the thermal conductivity experimental campaign, simultaneous measurements of the thermal conductivity and stress-strain properties are conducted. Even if the bed deformation [mm] is measured during the experiments at each investigated temperature, the evaluation of ε [%] is only possible at room temperature when the initial bed height is known. Therefore, the numerical

results are compared with the experimental outcomes of the UCTs conducted at room temperature performed during the thermal conductivity experimental campaign.

For the assembly simulating 20 LMT, representative of the size distribution for the melt-based process, another assembly with a PF of approx. 64 % has been created. For this assembly the loading/unloading process has been repeated 30 times. Three maximum loads of 6, 4 and 2 MPa are applied. The maximum compressive load of 6MPa has been selected because it is considered as the upper limit for the cyclic thermal stress peaks in the breeder zone. The performed simulations are listed in Table 6-1. The sample ID reported in the table assigns the investigated material, the number of loading cycles and maximum load.

Due to lack of experimental data, the mechanical properties of EU Ref. are used for all investigated assemblies. A Young's modulus of (E) equal to 90 GPa and a Poisson's ratio (ν) equal to 0.25 are taken. The friction coefficient (μ_f) is set to 0.1. The mechanical behaviour of pebble beds subjected to cyclic loads at high temperatures is not addressed due to a lack of material properties data at high temperatures. All mechanical properties available refer to room temperature.

Table 6-1: Performed simulations.

ID	No. Loading cycles	PF [%]	Max. load [MPa]
20LMT-30-6			6
20LMT-30-4	30	64.056	4
20LMT-30-2			2
20LMT-5	5	64.225	6
25LMT-5	5	64.226	6
30LMT-5	5	64.246	6
EU Ref.-5	5	64.154	6

6.2 Numerical results and Discussion

Due to pebble rearrangements and crushing, granular materials show a densification when subjected to cyclic loading that can be accentuated by the magnitude of the alternating loading itself [112]. This is defined as ratcheting of the material, which describes the gradual accumulation of permanent deformation. In some cases, the material can adapt to the external excitation and does not accumulate further deformations (shake down condition). Figure 6-2 shows the simulated stress-strain curves of the investigated assemblies for five compressive

cycles. In the graph only the first two loading/unloading cycles are reported (to avoid the figure to be overloaded by curves plotted on top of each other). As shown in the figure, the size distribution influences the stress-strain behaviour of the assemblies. Even though the EU reference breeding material has the lowest PF, it shows the stiffer behaviour (smaller strain for a given stress) with a residual strain less than 0.2% after the first unloading. This assembly is characterized by a narrow and peaked size distribution resulting, for the given PF, in a denser configuration in comparison to the ACB materials. The assemblies representing the modified breeder compositions show a softer behaviour compared to the reference breeding material. Furthermore, even if the three assemblies have the same size ranges, differences in the overall stress-strain behaviour due to the different pebble size distributions are observed. In particular, the stiffer behaviour with the lower residual strain after the first unloading refers to 20 LMT, which shows a peaked pebble size distribution around 575 μm . Samples with 25 and 30 LMT are characterized by a smoother pebble size distribution resulting in a softer stress-strain behaviour. In particular 25 LMT deforms significantly (approx. 0.4%) before the stress is build up.

In Figure 6-3 the simulated stress-strain curves of 20LMT-30 with a maximum compressive load of 6, 4 and 2 MPa are reported. For this assembly 30 loading/unloading cycles have been simulated while the figure shows only the first and the last cycles. An increase of the total residual strain with increasing maximum compressive load is observed. Because of the greater perturbation provided to the system, the residual strain of the bed is more pronounced with higher loads than with smaller loads (higher contact forces are induced leading to overcome the friction between pebbles).

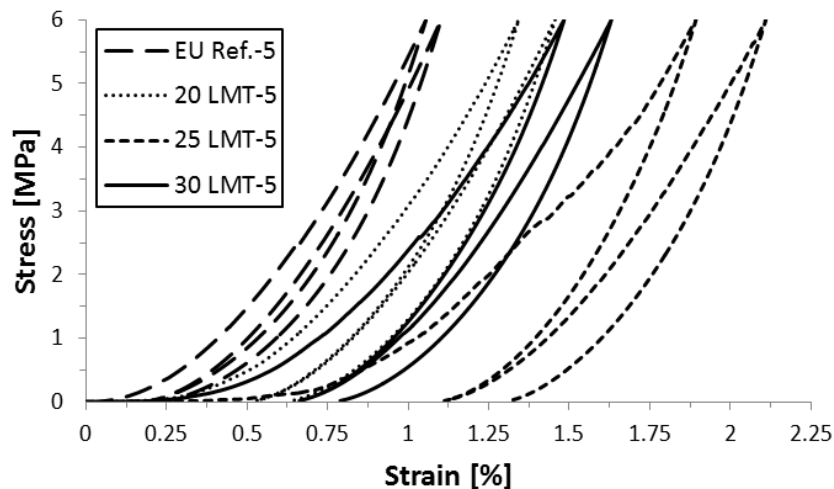


Figure 6-2: Simulated stress-strain curves of the investigated compositions for the 1st and the 5th loading/unloading cycle.

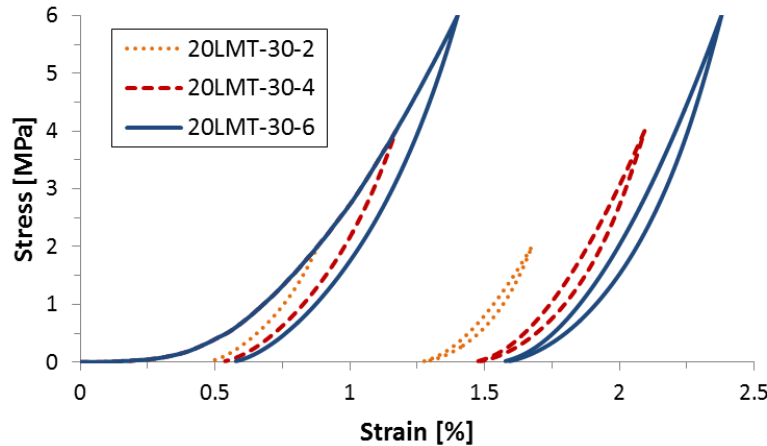


Figure 6-3: Simulated stress-strain curves for the 1st and the 30th loading/unloading cycles with different maximum compressive load.

The results of the simulations are compared with the experimental outcomes in terms of difference between residual strains of two consecutive cycles ($\Delta\epsilon_r$) and calculated oedometric modulus (E). The difference between the residual strains of two consecutive cycles represents the increment of the irreversible residual strain due to the cycling loading. The experimental and simulated stress-strain curves are not directly compared because the first loading/unloading cycle sensitively depends on the initial PF and on the first approach of the piston to the pebble bed. Previous studies [74]-[75] showed that the initial PF plays an important role for the mechanical response of an assembly in both experimental and DEM simulations. The experimental PF is an average of bulk and near wall regions PFs while the DEM assembly represents the bulk region of a pebble bed, because of the periodic boundary conditions applied to the model boundaries. Moreover, a quantitative comparison with experimental data in terms of stress-strain curves, even after the second cycle onwards, cannot be made. The experimental curves show a stiffer behaviour while a more compliant response is observed for the simulations. This is due to the differences that exist between simulations and experimental conditions. In particular to the H/D ratio adopted in the UCTs and to the friction coefficient between pebbles used in the simulations. In the present work the attention is focused on the engineering parameters needed for the design of the solid breeder blanket concept.

In Figure 6-4, the difference between the residual strains of two consecutive cycles are reported and compared to the experimental data. The residual strain after the first loading cycle is omitted. A good agreement between experiments and simulations is noticed, the maximum observed difference between the experimental and simulation values is about 0.1%. The EU Ref.

shows a smaller difference between the residual strains of two consecutive cycles, evidence of the denser structure developed in this material, which is closer to its maximum PF than in case of ACB materials.

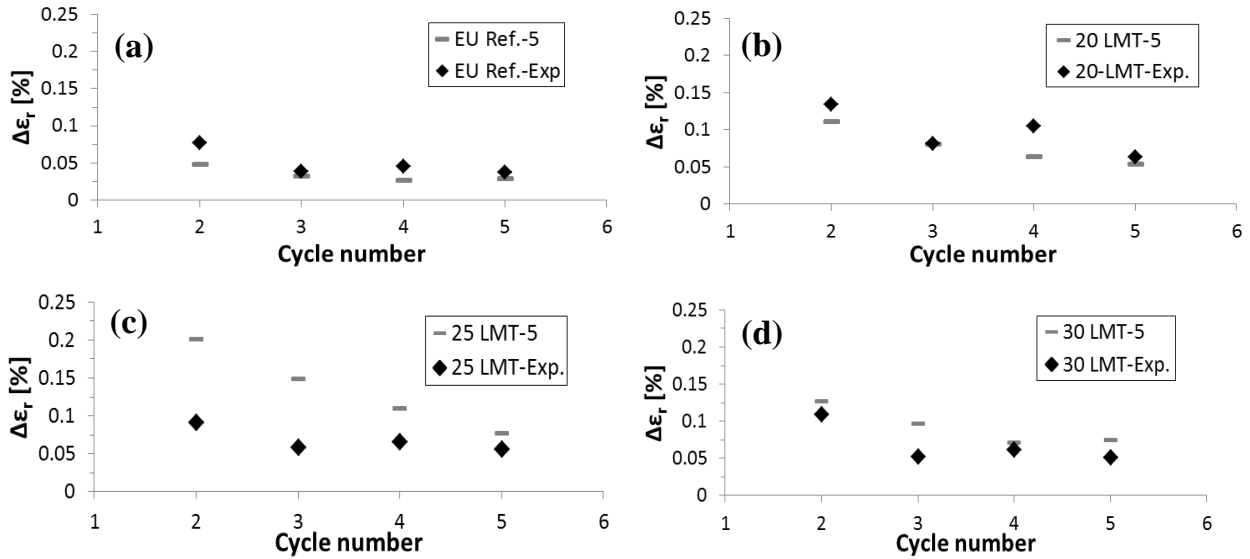


Figure 6-4: Difference between measured and computed residual strains of two consecutive cycles of EU Ref. (a), 20 LMT (b), 25 LMT (c), and 30 LMT (d).

In Figure 6-5, the residual strain and the difference between the residual strains of two consecutive cycles as a function of the cycle number of 20LMT-30 are illustrated. The largest part of the irreversible residual strain occurs during the first 15 cycles, while the compaction of the assembly is still progressing but exhibiting smaller increments as the cycling proceeds. In terms of difference between the residual strains of two consecutive cycles the maximum compressive load affects the first 5 cycles. Similar results were reported in [66] and [81]. However, quantitative comparisons cannot be made because of the different pebble size and boundary conditions used.

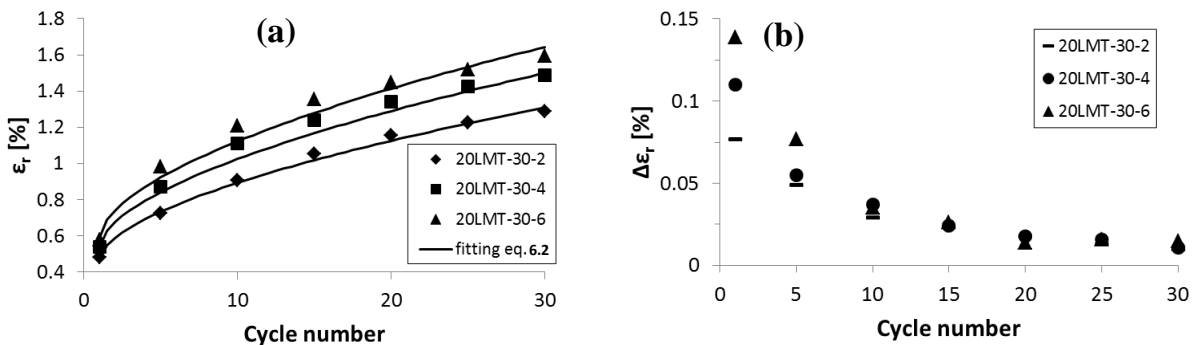


Figure 6-5: Computed residual strain (a) and difference between the residual strains of two consecutive cycles (b) of 20LMT-30 as a function of the cycle number.

Figure 6-6 exemplarily displays the calculated oedometric moduli derived from the experimental and the simulated stress-strain curves. In the figures the oedometric moduli of 30LMT are reported as a function of the compressive load. The oedometric modulus (E) is calculated according to eq. 2.4 during the unloading. Hence, $E-L1$ and $E-L5$ in the figures refer to the oedometric modulus calculated for the first and the fifth unloading, respectively.

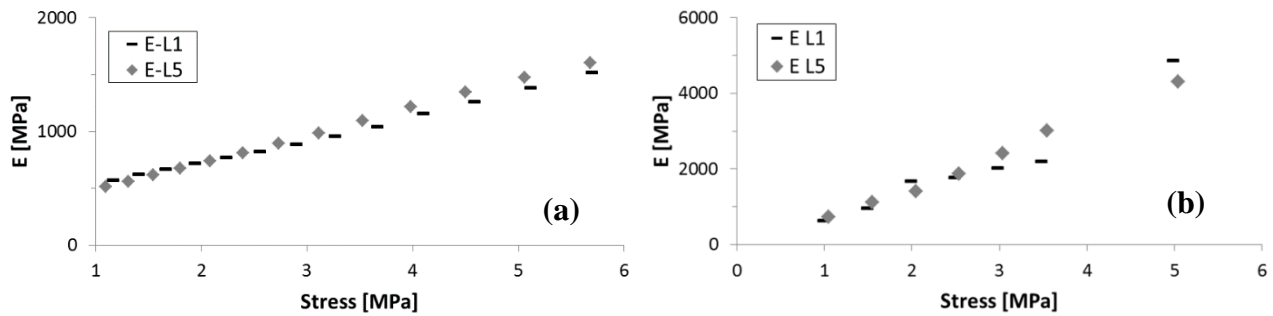


Figure 6-6: Calculated oedometric moduli as a function of the stress derived from the simulated (a) and the experimental (b) stress-strain curves.

An increase of E with the compressive load is observed for all investigated compositions in both experimental and DEM simulations, however, higher values of E are obtained from the experimental data, than in the simulation. This reflects the more compliant mechanical response observed for the simulated curves. The stress-strain behaviour obtained by the uniaxial compression test is influenced by the ratio H/D . As reported before, the experimental data refer to a 40 mm high pebble bed with a diameter of 55 mm ($H/D = 0.73$). As reported in [16] the wall friction, which is directly related to the ratio H/D , affects the steepness of the unloading curve leading to higher values of E compared to the simulations, in which the friction between the boundaries and pebbles has not been considered. Furthermore, due to the lack of experimental data, an arbitrary friction coefficient between pebbles equal to 0.1 is used. As reported in [75] the friction coefficient can have profound influence on the stress-strain response of the assembly. Therefore, a quantitative comparison between experimental and simulations results on the calculated elastic constants cannot be made.

In Figure 6-7, the oedometric moduli upon unloading of the simulated assemblies as a function of the cycle number are reported. In agreement with [81] the numerical results show an increase of E with the progressive compaction of the assemblies due to the cycling loading, the increase falls between 5% and 7%. As shown no significant influence of the pebble size

distribution of the assembly can be observed; the maximum difference between the assemblies after five cycles is about 5%.

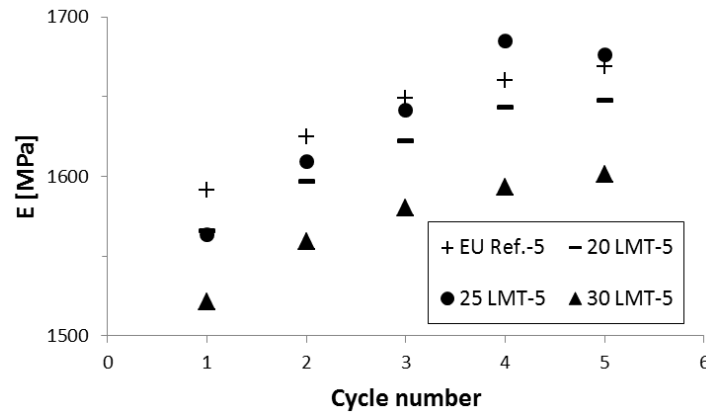


Figure 6-7: Increase of the oedometric modulus upon unloading as function of the cycle number derived from simulations.

In Figure 6-8 the calculated oedometric moduli upon unloading of 20LMT-30 are shown as a function of the cycles for compressive loads of 6, 4 and 2 MPa. An increase of E with increasing maximum compressive load is obtained. The higher compressive load leads to a higher ability of the pebbles to move in the structure, resulting in a denser packing structure of the assembly (higher PF) than in the assemblies subjected to a lower compressive load. An increase of E with the progressive compaction of the assemblies is obtained due to the cycling loading. More cycles are simulated for this assembly, and it has been observed that E is increasing rapidly during the first 10 to 15 cycles and it tends to saturate afterwards. Of a total observed increment of about 13% after 30 cycles, an increase of approx. 10% has been already obtained after 15 cycles.

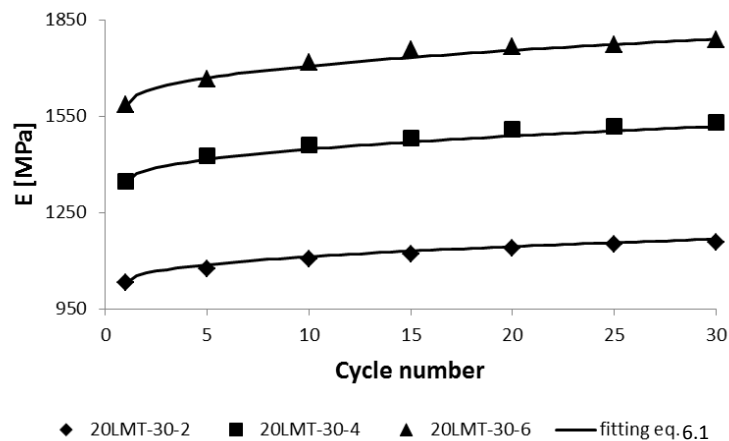


Figure 6-8: Increase of the oedometric modulus upon unloading as a function of the cycle number for 20 LMT-30 derived from simulations.

The following correlations, based on the simulations are suggested to estimate E and ε of ceramic pebble beds as a function of cycle number (N) for compressive loads of 2, 4 and 6 MPa:

$$E_N[\text{MPa}] = E_1 [0.031(N - 1)^{0.434} + 1], \quad 6.1$$

$$\varepsilon_N [\%] = \varepsilon_1 [0.25(N - 1)^{0.583} + 1]. \quad 6.2$$

Here E_1 is the oedometric modulus upon the first unloading, while ε_1 denotes the residual strain after the first unloading. Since a good qualitative agreement between experiments and simulations has been achieved in terms of difference between residual strains of consecutive cycles eq. 6.2 can reasonably represent also the experimental results. The values of E_1 and ε_1 are listed in Table 6-2 for the investigated compressive loads.

Table 6-2: Numerical coefficients

Max. load [MPa]	E_1 [MPa]	ε_1 [%]
2 MPa	1030	0.47
4 MPa	1340	0.54
6 MPa	1580	0.59

6.3 Summary

The effect of cyclic loading on the mechanical behaviour of pebble bed assemblies is studied using the in-house KIT-DEM code, for four assemblies with different pebble size distributions.

Results of numerical simulations show that the pebble size distribution affects the stress-strain behaviour of the assemblies. The assembly representing the EU reference breeding material, characterized by a narrow and peaked size distribution, shows a stiffer behaviour compared ACB material assemblies, which are characterized by a broader size distribution. The stiffer behaviour of the EU Ref. indicates a denser structure developed in this material, closer to the maximum theoretical PF than the ACB materials. In comparison, pebble beds characterized by a broader pebble size distribution can experience higher strains without building up stress at the beginning of loading.

Even if the simulated residual strain after the first unloading cannot be compared with the experimental one, mainly because of the uncertainty of the initial PF and of the first approach of

the piston to the pebble bed, a good qualitative agreement between experiment and simulation results is obtained in terms of difference between residual strains of consecutive cycles. In agreement with [66], the first 10-15 cycles are responsible for the largest part of the irreversible residual strain. Afterwards, as the cycling proceeds, the compaction of the assembly is still progressing but exhibiting smaller increments. The maximum compressive load imposed on the bed affects the first 5 cycles. This means that increasing the imposed load leads to a higher irreversible strain during the first cycles as compared to a lower load. However, for the period following the first 5 cycles, the same increasing rate is reached at a lower compressive load. The EU Ref. material shows a smaller difference between the residual strains of two consecutive cycles, this confirm the fact that this material is closer to the maximum possible PF.

Because of the influence of the wall friction and the friction coefficient between pebbles, a quantitative comparison with experimental data in terms of stress-strain curve and calculated oedometric modulus cannot be made. An increase of the oedometric modulus with the compressive load is obtained for all investigated compositions in both, the experiments and the DEM simulations. The results show no significant influence of the pebble size distributions on the oedometric modulus. However, an increase of E with increasing imposed compressive load is observed. The numerical results show an increase of E with progressive compaction of the assemblies due to the cycling loading. The simulations show that E is rapidly increasing during the first 10 to 15 cycles and tends to saturate afterwards.

From the results of the simulations correlations for the estimation of E and ε of ceramic pebble beds as a function of the cycle number for maximum compressive loads of 2, 4 and 6 MPa are derived.

Chapter 7

Experimental and numerical study of cyclic behaviour of ceramic pebble beds

This chapter extends the validation study presented in Chapter 6. The results of a dedicated experimental campaign aimed at the mechanical characterization of pebble beds are presented. UCT experiments are conducted along with DEM numerical simulations to investigate the effects of the pebble properties and the blanket operational parameters on the micro and macro mechanical response of breeder beds subjected to cyclic loading. Polydispersed breeder ceramics and monosized commercial zirconia pebbles are used to study the influence of the pebble properties, the bed height and of the bed height to pebble size ratio (H/d). The numerical experiments are carried out with the KIT-DEM code on pebble assemblies using mixed boundary conditions. Thanks to the micro scale numerical modelling the macro scale response is presented together with the micro response at pebble scale.

7.1 Experimental

The test cell for the thermal conductivity measurements has been used here as test cell for the oedometric test. Figure 7-1 shows the developed UCT facility. It consists of a cylindrical container ① of 55 mm inner diameter with a steel disk ② placed in the bottom part. The thickness of the disk can be varied to change the experimental H/D ratio.

In this study the diameter of the container has been kept constant (55 mm) while the bed height is varied to study the influence of the wall effects on cyclic behaviour of ceramic pebble beds. A diameter of 55 mm is considered to be large enough in relation to the maximum diameter of the studied pebbles $d=1.2$ mm.

Both the EU reference (EU Ref.) and advanced (ACB) tritium breeding materials are investigated. The two materials differ in chemical composition of the bulk material, the production process and the pebble size distribution. In this study the investigated ACB material

consists of about 70 mol% Li_4SiO_4 and 30 mol% Li_2TiO_3 . The pebble size distributions of the investigated materials are shown in Figure 7-2.

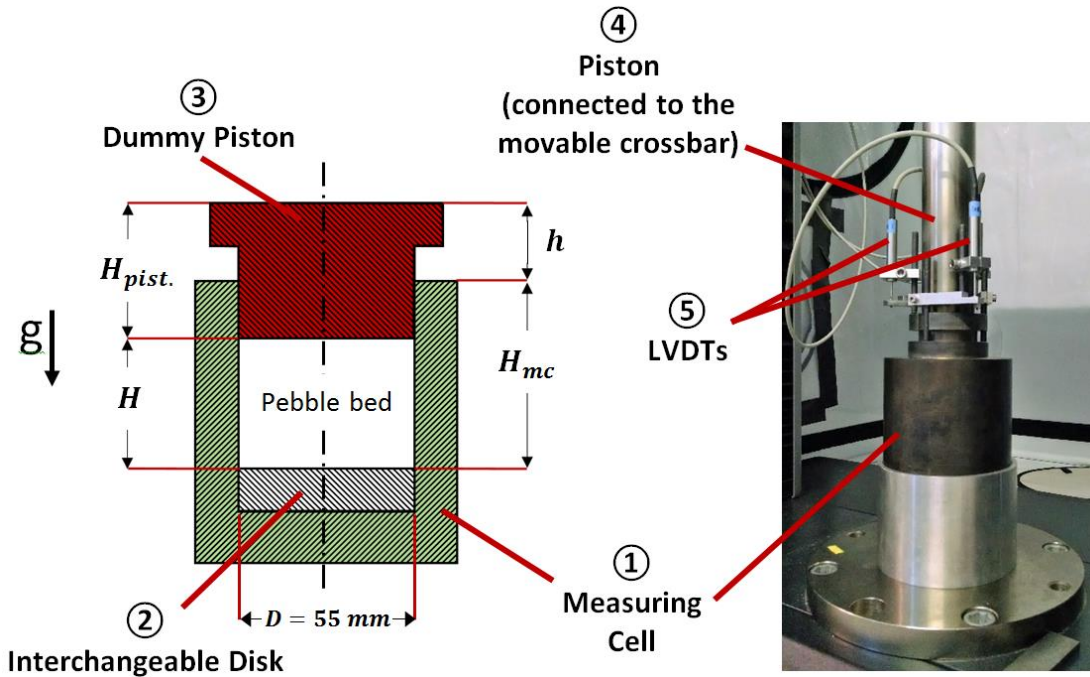


Figure 7-1: Cross-sectional cut view of the odometer test cell and dummy piston for the evaluation of the initial bed height (left), photograph of the experimental setup (right).

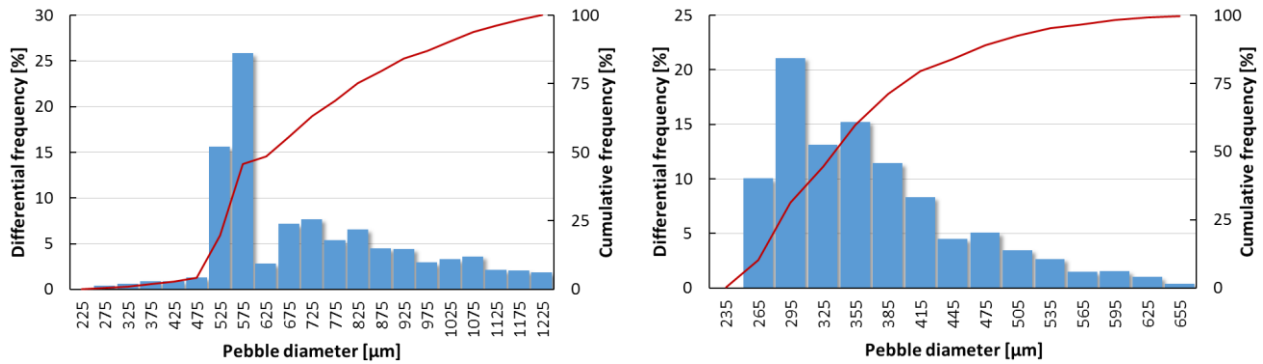


Figure 7-2: Measured size distributions of ACB (left) and EU Ref. (right) materials.

High quality commercial Ytria-stabilized Zirconia (YTZ) pebbles [113] with different sizes are also employed to investigate the influence of the bed height to pebble size ratio (H/d) on the cyclic response of packed beds. The zirconia pebbles consist of nearly monosized perfect spherical particles, with a sphericity < 1.06 and diameter variation $< 10\%$. The sphericity of the pebbles has been calculated as the ratio of the maximum over the minimum diameter obtained from optical micrographs (2D projection of the pebbles) of a representative sub sample of the selected material. Three diameters are used, namely 1, 0.65 and 0.3 mm.

The pebbles are packed in the odometer test cell following the procedure described in Sect. 4.1 while the initial PF is calculated according to eq. 4.1. For the ACB and EU Ref. materials a PF around 64%, consistent with the reference value of the actual EU breeding blanket design, has been readily achieved by mechanical vibration. The zirconia pebbles are poured and gently tapped in the measuring cell resulting in a PF of about 62.7%. The monosized zirconia pebbles are not further densified to leave a margin to study the densification induced by the cyclic compression. A breeding bed relevant PF of 64% is difficult to achieve with single size pebbles, since a packing density of 64% represents the random close packing limit for monosized particles [114].

Once that the desired PF is achieved the test cell is placed in the testing machine and the pebble bed is compressed by the piston ④ connected to the movable crossbar, Figure 7-1. The experiments are monitored and controlled by a dedicated LabVIEW program. The beds are cyclically loaded up to 6 MPa with a loading speed of 1 MPa/min. The number of applied compression cycles ranges from 200 to 400, while the investigated initial bed heights have been 40, 20 and 10 mm. The macroscopic applied stress is calculated as the ratio of the applied force, measured by a load cell, to the area of the piston, while the displacement of the piston is measured by means of LVDTs ⑤ as in the thermal conductivity experimental campaign (Sect. 4.1). The bed strain ε [%] is calculated according to eq. 4.2.

The experiments are conducted at room temperature in order to properly evaluate the bed strain ε [%]. The physical characteristics and the main experimental conditions of the investigated materials are given in Table 7-1. For the polydispersed materials the average diameter of the distribution is used to calculate the H/d ratio.

Table 7-1: Investigated materials and main experimental conditions.

ID	Material	Pebble diameter [mm]	Density [gr/cm ³]	PF [%]	H [mm]	H/d [/]
EU Ref.	Li ₄ SiO ₄ + 10 mol% Li ₂ SiO ₃	0.25-0.65	2.30	64±0.1	20; 40	≈ 54; 108
ACB	Li ₄ SiO ₄ + 30 mol% Li ₂ TiO ₃	0.25-1.25	2.44	64±0.1	10; 20; 40	≈ 14; 28; 56
YTZ - 1	95% ZrO ₂ + 5% Y ₂ O ₃	1	6.07	62.65±0.1	10; 20; 40	10; 20; 40
YTZ - 0.65	95% ZrO ₂ + 5% Y ₂ O ₃	0.65	6.07	62.7±0.05	20; 40	≈ 31; 62
YTZ - 0.3	95% ZrO ₂ + 5% Y ₂ O ₃	0.3	6.07	62.7±0.05	20; 40	≈ 67; 134

7.2 Numerical experiments

Numerical simulations of UCT have been carried out using the KIT-DEM code [74]-[75], [78]. To simulate the UCT experiments mixed boundary conditions have been applied in contrast to the simulations reported in Chapter 5. Rigid planar walls are used to simulate the top and bottom boundaries of the odometer test cell while Periodic Boundary Conditions (PBCs) are set at the lateral sides of the assemblies. In order to simulate a high number of loading cycles, with a reasonable computational time, PBCs are used to reduce the number of pebbles needed to represent bulk behaviour. While the assembly height is varied to study its influence on the mechanical response, the two lateral dimensions are determined as ten times the average diameter of the size distribution for polydispersed assemblies (weighted average on the diameter probability) or ten times of the particles' diameter for monosized assemblies.

The assemblies are subjected to cyclic loading simulating the uniaxial compression experiments. To this end, the upper wall is moved downwards (or upwards) to cyclically compress (or relax) the bed, while the lower wall is kept fixed as in the experiments. A strain controlled loading scheme is adopted. A constant strain rate is incrementally applied (or removed) to the assemblies moving downwards (or upwards) the upper wall at the beginning of each loading step. The reaction force acting on the upper wall is then obtained by the calculation of the interaction forces based on the implemented force–displacement law at the pebbles contacts. When the force acting on the upper wall reaches the maximum value ($\sigma_z = 6$ MPa) the bed is unloaded by gradually moving upwards the upper wall until the stress-free configuration, $\sigma_z \approx 0$, is reached. Then the assembly is again compressed moving downwards the upper wall in the consequent loading cycle.

Numerical simulations have been conducted with both breeder ceramics and commercial zirconia pebbles. The assemblies representing the breeder ceramics are generated with the actual pebble size distributions of the EU Ref. and ACB materials used in the experiments (Figure 7-2). To investigate the influence of the sample height four different assemblies are generated with a height of 40, 30, 20 and 10 mm for each breeder material. Regarding the Y TZ pebbles five monosized assemblies are generated with a pebble size of 2, 1, 0.65, 0.5 and 0.3 mm with a sample height of 20 mm. This is done to study the influence of the bed height to pebble size ratio (H/d) on the mechanical response of the assemblies. The sample height of 20 mm is selected

because representative of the breeder zone thickness. While the experiments are performed with 1, 0.65 and 0.3 mm pebbles in the simulations 0.5 and 2 mm particles are additionally used to broaden the H/d ratio. The material properties of the EU Ref. material used in this study are consistent with those used in earlier studies [74]-[75], [78]. Due to lack of material properties data, the same mechanical properties are used for the ACB material. The friction coefficient of glass spheres measured in [115] is taken for YTZ pebbles while the mechanical properties are taken from [116]. The same friction coefficient is applied for both the inter-particle and particle-wall friction. For each material an assembly with a PF close to the experimental value reported in Table 7-1 has been created. The parameters used to run the simulations are summarized in Table 7-2.

Table 7-2: Parameters used in the numerical simulations.

ID	PF	E	ν	Inter-particle and particle-wall friction	Pebble size d	H	Number of particles	H/d	No. Loading cycles
				μ_f [/]					
	[%]	[GPa]	[/]	[/]	[mm]	[mm]		[/]	
40-EU Ref.						40	5500	≈ 56	9
30-EU Ref.	$\approx 64\%$	90	0.25	0.1	0.25-0.65	30	4125	≈ 42	13
20-EU Ref.						20	2750	≈ 28	21
10-EU Ref.						10	1375	≈ 14	52
40-ACB						40	11400	≈ 108	22
30-ACB	$\approx 64\%$	90	0.25	0.1	0.25-1.25	30	8550	≈ 81	29
20-ACB						20	5700	≈ 54	53
10-ACB						10	2850	≈ 27	104
YTZ-2									
YTZ-1					1	2391	20	200	
YTZ-0.65	$\approx 62.6\%$	210	0.25	0.05	0.65	20	3678	≈ 31	100
YTZ-0.5					0.5	4782	40	70	
YTZ-0.3					0.3	7970	≈ 134	40	

7.3 Results and Discussion

The macro scale response of the studied assemblies is hereafter presented together with the micro response at the pebble-scale. The macro scale response is described by the evolution of macro parameters such as the stress-strain curves and residual strain accumulation. The micro mechanical response is studied in terms of axial packing factor profile, coordination number, contact force distribution and contact force evolution. Since the micro-scale response of the

granular assembly is not experimentally accessible the micro parameters presented are obtained numerically.

7.3.1 Macro scale response

Figure 7-3 exemplarily shows the experimental and the respective simulated stress-strain curves for monosized and polydispersed assemblies. Comparing the numerical and the experimental results it can be observed that DEM simulations captured the different macroscopic behaviour between monosized and polydispersed assemblies. With a residual strain around 0.1% after the first unloading, the monosized assemblies show a much stiffer response than the breeder materials (polydispersed assemblies). This reflects both the superior mechanical properties and the size distribution of the Y TZ pebbles. In particular, the residual strain is mainly influenced by the size distribution and the friction coefficient between the pebbles, while the slope of the stress strain plot is influenced mainly by the elastic constants of the pebbles.

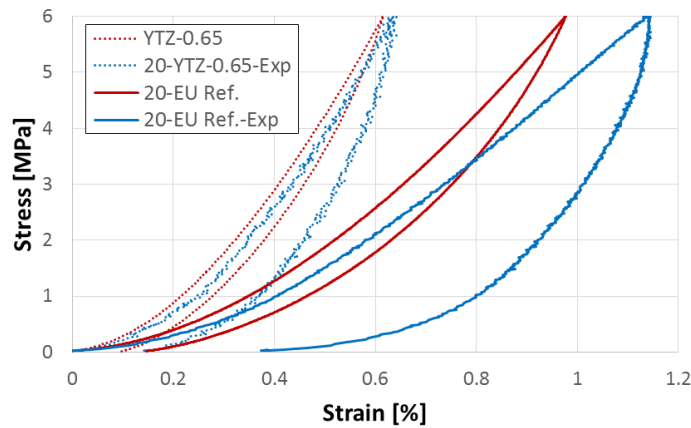


Figure 7-3: Comparison between experimental and simulated stress-strain curves for monosized and polydispersed assemblies for the 1st loading/unloading cycle.

A good quantitative agreement between experiments and simulations is obtained for monosized assemblies (Figure 7-3), for which the shape of the stress-strain curve is quite accurately reproduced with a deviation of only 0.1%. For polydispersed assemblies the shape of the stress-strain plot differs, especially during the unloading, from the experimental one. The simulated curves show a non-linear elastic unloading while the experimental curves show a pronounced ‘hook’ shaped non-linear unloading.

The difference in the unloading behaviour can perhaps lie in the differences between the simulations and the laboratory experiments. Since the performed DEM simulations are highly computationally expensive, in order to reduce the computational time, PBCs have been used to

minimize the number of pebbles composing the assemblies. However, by using PBCs the effect of the walls on both the mechanical confinement and the near-wall packing structure of the assembly are neglected. Moreover, in the simulation the pebbles are simulated as perfect spherical particles while the real breeder pebbles, even if characterized by a good sphericity, are not perfect spheres. The influence of the aspect ratio on the macroscopic and microscopic response of monosized ellipsoidal particles was addressed in [79], where the shape of the particles was found to noticeably influence the macroscopic mechanical behaviour of the assemblies. The numerical replication of the laboratory experiment in all its details, even if feasible, would be very computationally expensive because of the very high number of required pebbles. This would have precluded the possibility to simulate the multiple loading cycles. Moreover, the aim of the present work is not to reproduce the experiment with DEM simulation but instead to gain an insight about the influences of the pebble properties and the blanket operational parameters on the mechanical response of breeder beds subjected to cyclic loading. To this end, the use PBCs is unavoidable while the constraints concerning the use of PBCs are considered to be reasonable. Despite the before mentioned differences the macro as well as the micro mechanical parameters resulting from the DEM simulations represent a good approximation of the physical reality. Evidence of this is the fact that all the experimentally observed trends are also reproduced by the DEM simulations.

Whether the breeder beds experience a progressive accumulation of plastic deformation (ratcheting), or whether this process will shake down should be assessed in order to effectively control and manage the gap formation that may lead to isolated overheated zones in the breeding zone during operation. To study the influence of the pebble size on the ratcheting behaviour of granular beds monosized YTZ pebbles are used. Figure 7-4 shows the obtained experimental and numerical results in terms of strain accumulation (ϵ_r) as a function of the number of applied cycles. For all sizes the residual strain is rapidly accumulating during the first cycles. Successively the assemblies begin to accumulate a low but almost constant deformation as the cyclic loading proceeds. The experimental results indicate a lower “long term” strain accumulation for bigger particles although an almost identical strain accumulation rate is observed at the begin of the cycling for the three investigated particle sizes. The numerical simulations capture the same behaviour of the laboratory experiments predicting a lower strain accumulation for smaller particles. Moreover, for the extreme case of YTZ-2 for which the H/d is

10 the shake down is reached after 100 cycles. Experiments are also performed with 400 compressive cycles using YTZ-0.65 and YTZ-0.3 pebbles. Even after 400 cycles the assemblies do not reach the shake down condition.

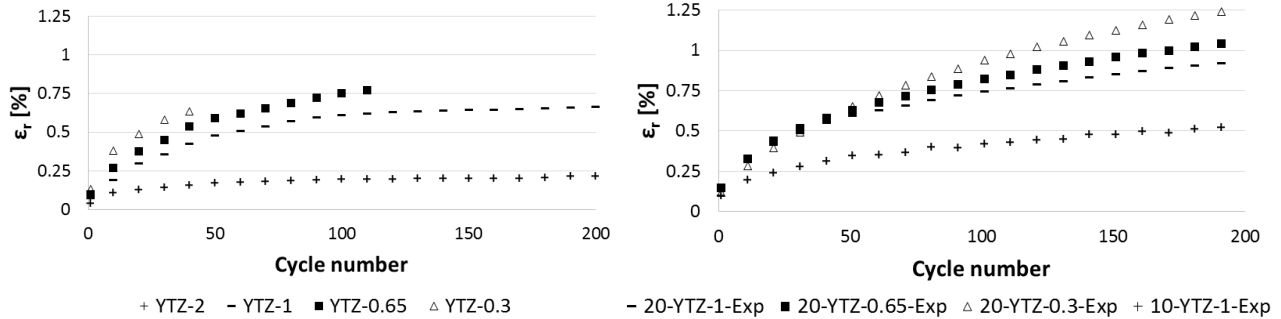


Figure 7-4: Numerical (left) and experimental (right) accumulated strain ϵ_r as a function of the number of cycles.

In Figure 7-5 the accumulated residual strain (ϵ_r) is displayed as a function of the H/d ratio at selected compressive cycles. Both experiments and simulations show an increase of the residual strain with the increase of the H/d ratio. The numerical results show a good quantitative agreement with the experimental outcomes.

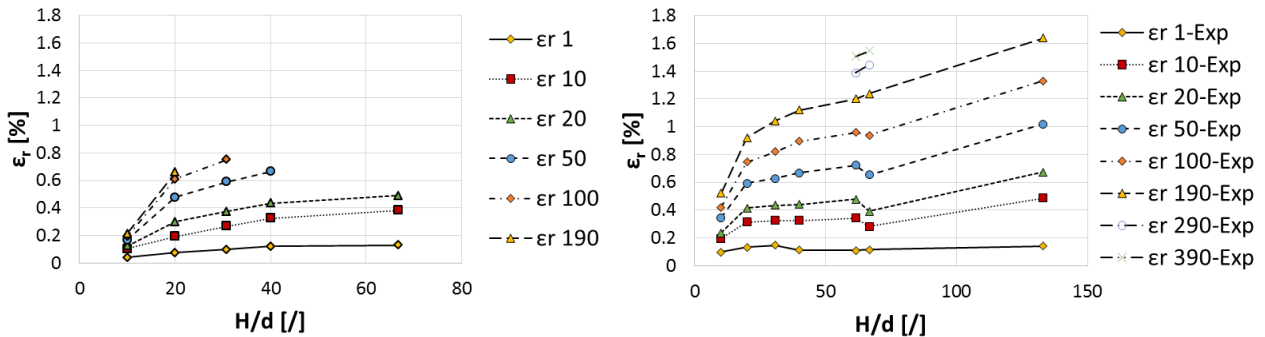


Figure 7-5: Accumulated residual strain as a function of the H/d ratio. Numerical (left) and experimental (right) values.

Figure 7-6a shows the experimental accumulated permanent strain for the breeder materials. Slight differences, in terms of residual strain, are experimentally observed between the two investigated bed heights for both materials. The EU Ref. breeder material shows a relatively higher permanent residual strain at higher number of cycles. In particular, the difference in strain between the ACB and the EU Ref. materials after 200 cycles is about 0.5%. For polydispersed assemblies beside the H/d ratio also the shape and the extension of the size distribution play a role in the compaction of the bed [79], [110]. For the ACB material the experimental results show a slight decrease of the accumulated permanent residual strain with the reduction of the

assembly's height. Figure 7-6 b and c exemplarily shows the comparison between the numerical and the experimental accumulated permanent strain for the ACB and EU Ref. materials, respectively. Even if the obtained residual strain at the end of the first unloading is greater in the experiments than in the DEM simulations, the numerical experiments predict quite accurately the permanent deformation of the bed. As in the experiments slight differences are numerically observed between the assemblies with $20 < H < 40$ mm, Figure 7-6d. However, the numerical results clearly show a much lower strain accumulation for the assembly with $H=10$ mm

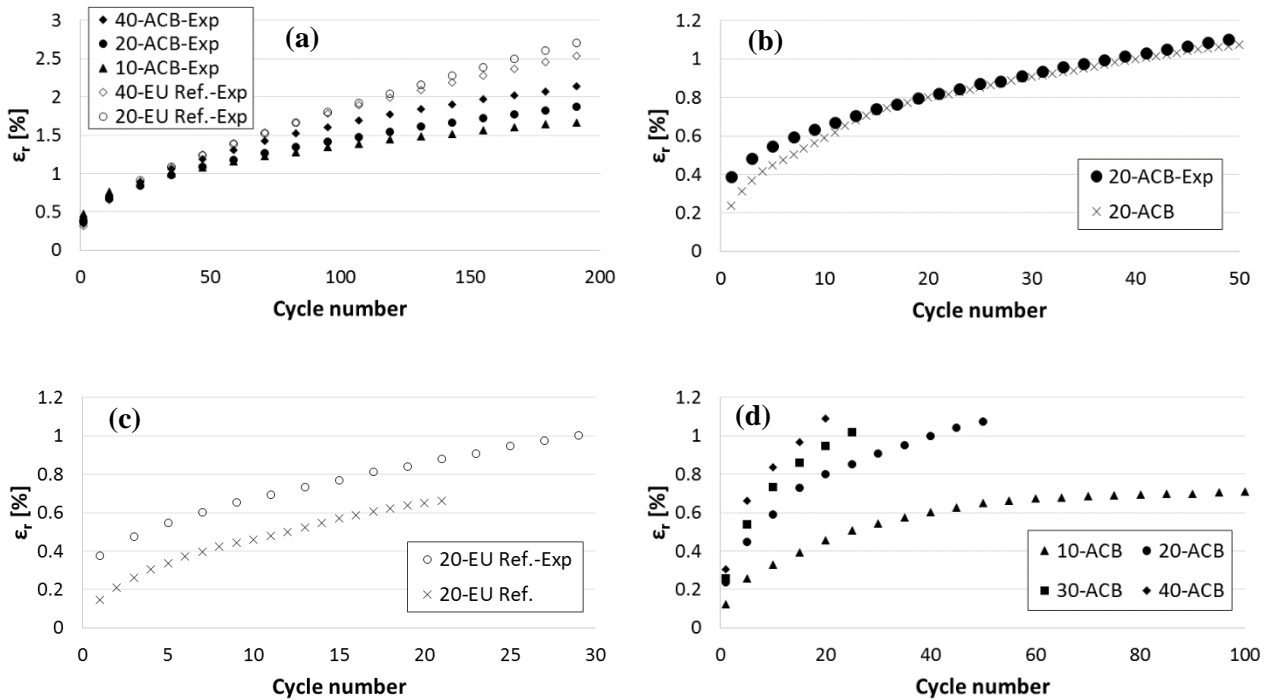


Figure 7-6: Accumulated strain ϵ_r as a function of the number of cycles experimental (a), comparison between experimental and numerical results (b)-(c), numerical results (d).

7.3.2 Particle-scale response

The study of the micro mechanical parameters can be used to better understand the macro response of the assemblies. The packing structure developed inside the assembly has a substantial influence on the overall micro and macro response of breeder beds. The heat transfer [117] as well as the mechanical response [16] of the beds is influenced by the packing structure of the particles.

Figure 7-7 shows the calculated axial packing factor profile for monosized assemblies. As in [111] and [118], the packing factor shows an oscillatory distribution next to the top and bottom walls as consequence of the presence of some regularly packed layers of pebbles induced by the

walls. The peak positions of the oscillations correspond to the particle radius. Moving away from the walls the oscillations progressively reduce to then vanish at 4-5 times the particle diameter. In this region the regular packing is progressively replaced by the random packing originating the bulk zone of the assembly. For low H/d ratio the bulk domain is not developed since the extinction length of the regular packing is comparable with the assembly height. Increasing the H/d ratio (i.e. reducing the pebble diameter) the near wall regions dimension progressively reduce while the bulk zone dominates the packing structure of the assembly. For the case $H/d = 10$ no bulk zone is observed while for $H/d = 40$ and 66.66 the bulk zone involves a large part of the assemblies height. The different ratcheting behaviour of YTZ-2, compared with the other pebble sizes, is due to the packing state consisting basically of ordered layers running through bed height. In this assembly the particles have less degree of freedom to move. Regarding the blanket applications, if monosized particles are employed, and shallow beds needed, the particle diameter should be varied accordingly in order to assure that the response of the bed is governed by the bulk response by limiting the extension of the near wall regions fluctuations. This to guarantee an isotropic and homogeneous response of the bed.

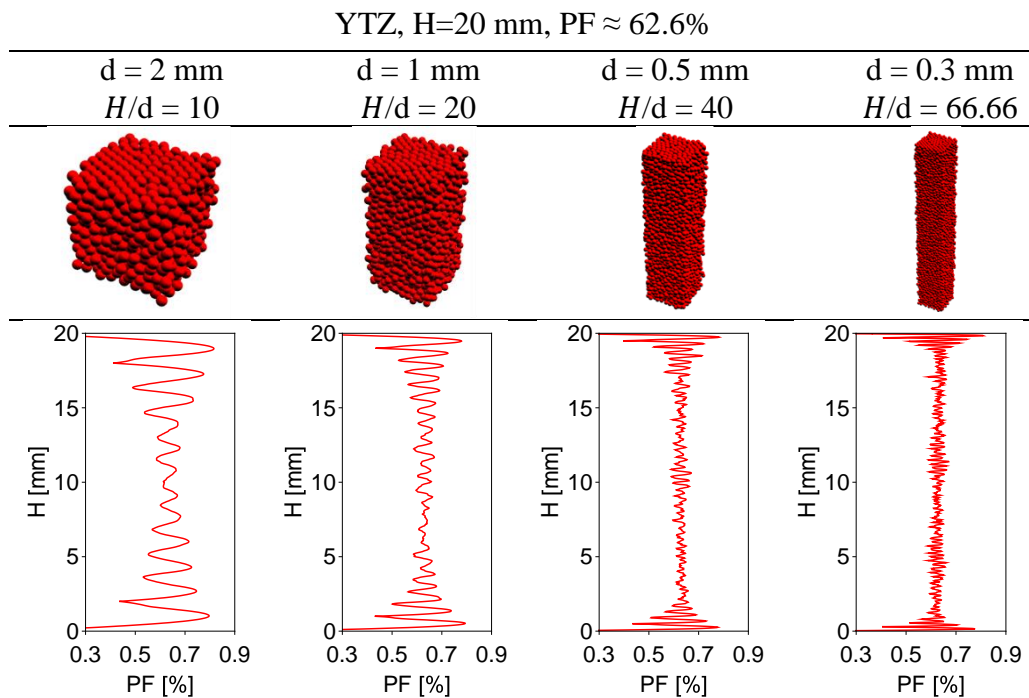


Figure 7-7: Axial packing fraction distribution for monosized assemblies.

Figure 7-8 shows the axial packing factor profile for polydispersed assemblies. In the figure the axial distribution of the ACB material is illustrated. Similar results are obtained for the EU Ref. material. For polydispersed beds the presence of the walls barely influences the packing

structure. The bulk zone dominates the packing structure of the assembly for all investigated assemblies' heights. Even for the lower investigated height ($H = 10$ mm) only one fluctuation of the packing factor profile, corresponding to the first layer of pebbles in contact with the boundary walls, can be observed. The observed similar mechanical response between the different bed heights reflects the facts that the bulk zone dominates the packing structure for all investigated assemblies' height.

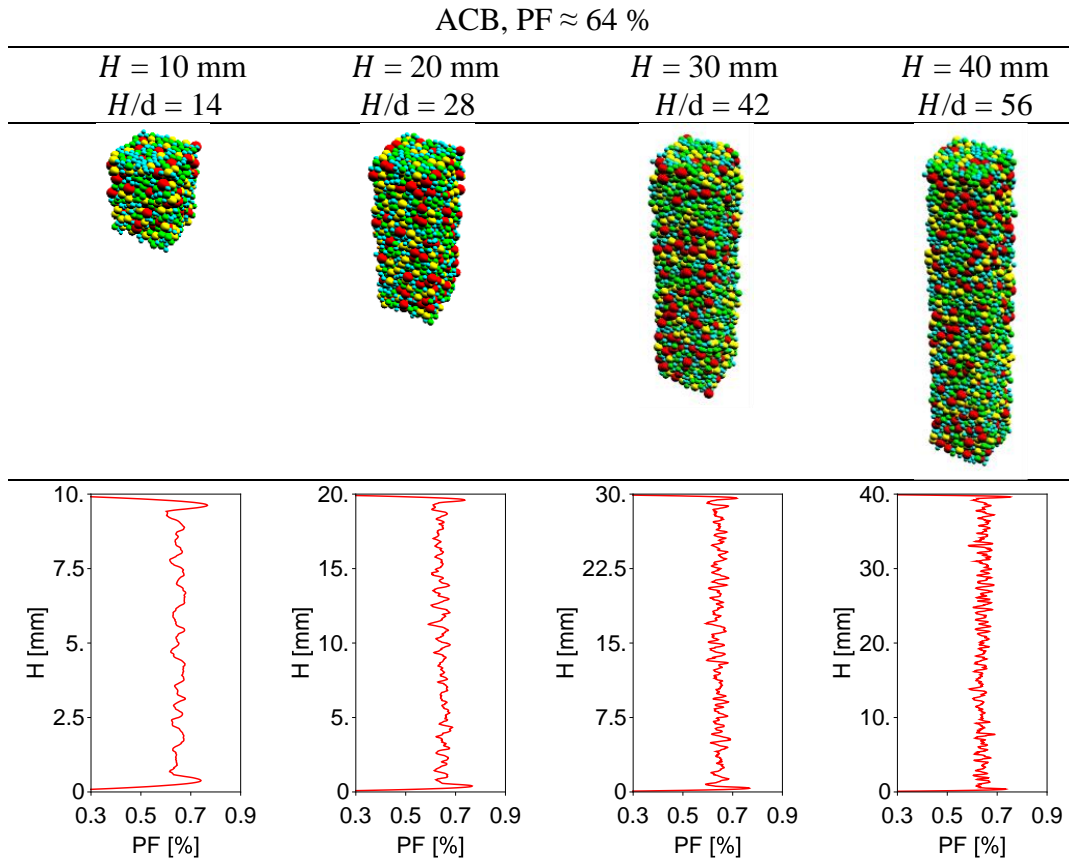


Figure 7-8: Axial packing fraction distribution for polydispersed assemblies.

The evolution of the coordination number with cycling for monosized assemblies is illustrated in Figure 7-9. The Coordination Number (CN) is calculated as $CN = N_c/N_p$, where N_c and N_p are the total number of contacts and the number of particles in the assembly, respectively. The coordination number is evaluated at the maximum load (6 MPa) and 20 KPa, representative of the unloaded state. The magnitude of the CN slightly increases with the reduction of the particle size. For all investigate sizes the CN increases during the first 10–15 cycles and it tends to saturate afterwards with some fluctuations. The increase of the CN during the initial cycles, with the subsequent stabilization, indicates a compaction of the assembly with a development of a stable network of contacts. Moreover, the evolution of the CN demonstrates that the major pebble

rearrangements occur during the initial loading cycles. New contacts are created as result of the compression resulting in a higher CN at the maximum load. In particular, at 6MPa the CN is about 10% higher than at the uncompressed state.

Figure 7-10 exemplarily shows the evolution of the CN against the cycle number for polydispersed assemblies. In the figure the CN of ACB material for the four investigated bed heights at 6 MPa and 20 KPa is reported. Compared with the monosized assemblies, the polydispersed assemblies show a similar evolution of the CN during the cyclic loading even if they show a relatively lower CN value than the monosized assemblies. The CN is found to increase slightly with the reduction of the assemblies' height.

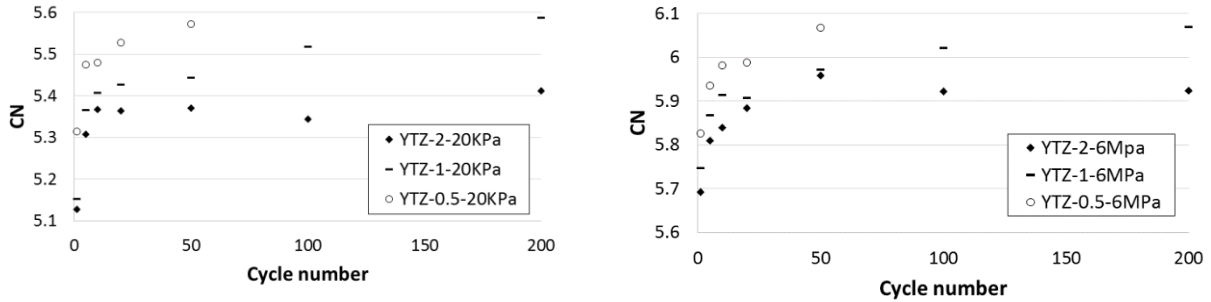


Figure 7-9: Evolution of coordination number with cycling for monosized assemblies.

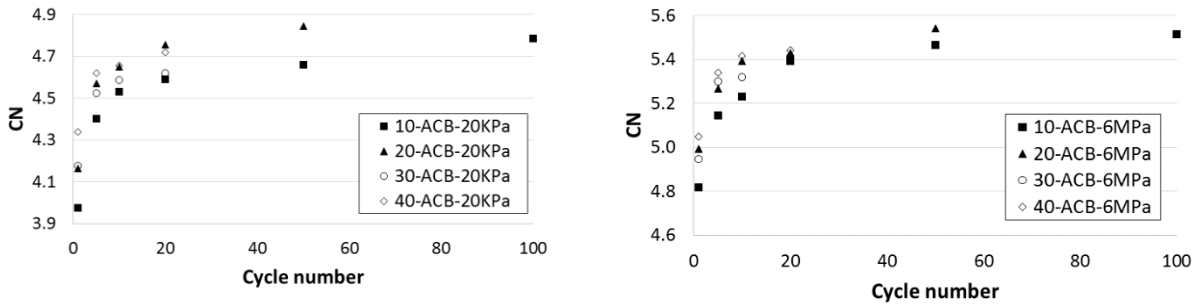


Figure 7-10: Evolution of coordination number with cycling for polydispersed assemblies.

Figure 7-11 shows the Probability Distribution Function (PDF) of the normalized normal forces ($\langle F_N \rangle = F_N^{ij}/f_{N_{ave}}$) and normalized maximum normal forces ($\langle F_{N_{max}} \rangle = F_{N_{max}}^i/f_{N_{ave}}$) for YTZ-1 at 6 MPa and 20 KPa for the first and the last loading cycles. Here F_N^{ij} is the normal force between the contacting particles i and j , $f_{N_{ave}}$ is the mean normal force inside the assembly and $F_{N_{max}}^i$ is the maximum contact force acting on the particle i . As shown, both probability distributions are substantially unaffected by the cyclic loading and by the compressive load at which the probability distributions are calculated. In agreement with previous studies [70], [74] for monosized pebbles the normalized normal forces distribution

shows a peak at $\langle F_N \rangle \approx 0.5$ indicating that most particles are subjected to a normal force lower than f_{N_ave} . On the other hand, the peak of maximum normal forces distribution is at $\langle F_{N_max} \rangle \approx 1.5$ implying that the majority of the particles experience a maximum normal force higher than f_{N_ave} . The influence of the pebble size and pebble size distribution on the probability distribution of normalized normal contact forces is exemplarily depicted in Figure 7-12. Among the monosized assemblies analogous distributions are obtained for the considered pebble sizes. However, the shape of the PDFs for the polydispersed assemblies differs from those of monosized especially for the normalized maximum normal forces distribution. The peak of $\langle F_{N_max} \rangle$ distribution is considerably changed. The distribution shows a broader peak slightly shifted to lower values while the $\langle F_N \rangle$ distribution shows a consistent shape despite the peak is slightly shifted to lower values. Among the polydispersed assemblies the probability distributions are found to be substantially unaffected by both the variation of the assembly height and size distribution.

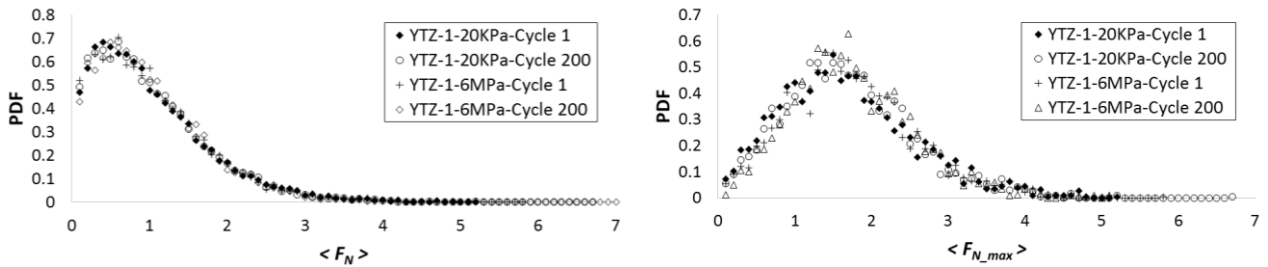


Figure 7-11: Probability density functions of normalized normal forces (left) and normalized maximum normal forces (right), influence of cycling loading.

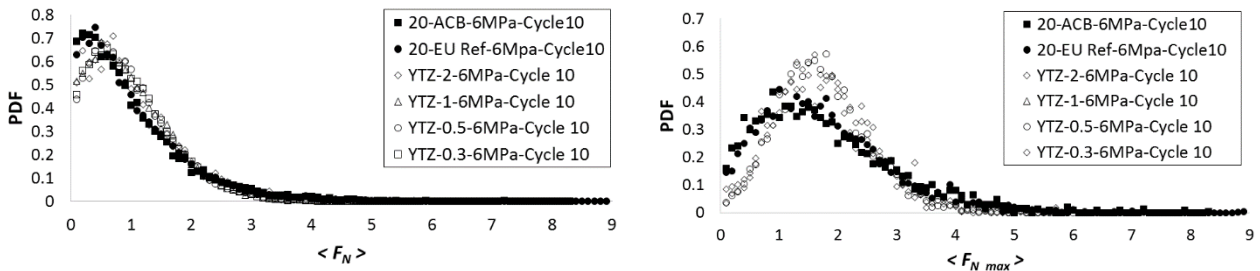


Figure 7-12: Probability density functions of normalized normal forces (left) and normalized maximum normal forces (right), influence of size distribution.

In Figure 7-13 the Cumulative Distribution Function (CDF) of the PDF of the normalized normal and maximum normal forces for monosized and polydispersed assemblies are exemplarily shown. Monosized and polydispersed assemblies show the same CDF of the $\langle F_N \rangle$. It should be noted that about the 40% of the contacts can be classified as “strong” contacts (a contact is defined strong if the normal contact force is greater than the average contact normal force

$f_{N_{ave}}$). The CDF for relative to $\langle F_{N_{max}} \rangle$ significantly differs between the monosized and polydispersed assemblies. In particular for the polydispersed assemblies about the 70% of the contacts carry a $f_{N_{max}}$ greater than $f_{N_{ave}}$, while for monosized assemblies the contacts experiencing a maximum force greater than the average rises up to about 80%. However, in polydispersed assemblies about 15% of the contacts experience a maximum force greater than three times $f_{N_{ave}}$ while this percentage reduces to 6-7% for monosized assemblies with pebble size range 0.3-1mm.

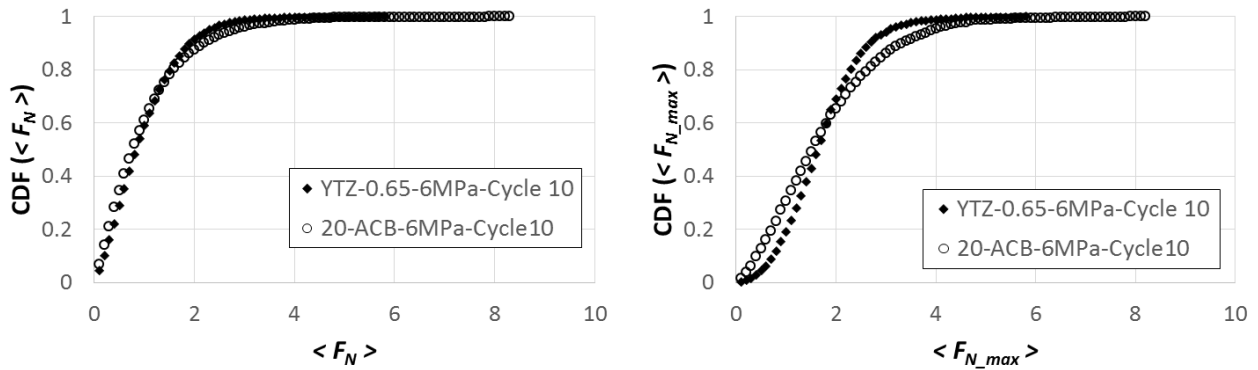


Figure 7-13: Cumulative distribution function of normalized normal forces (left) and normalized maximum normal forces (right), influence of size distribution.

Figure 7-14 exemplarily illustrates the evolution of the average and maximum normal contact forces for monosized and polydispersed assemblies at the maximum compressive load. No influence of the bed height is observed for polydispersed beds. In the graphs only the results for 10-ACB and 10-EU Ref. are shown since for these assemblies more cycles have been simulated. The magnitude of the contact forces increases with the increase of the particle size. The average diameters of the ACB (0.72 mm) and EU Ref. (0.37 mm) materials fit quite well into the respective size ranges of the YTZ. According to their average diameters the $f_{N_{ave}}$ and $f_{N_{max}}$ of ACB and EU Ref. polydispersed assemblies lie in between the values of YTZ-1;YTZ-0.65 and YTZ-0.5;YTZ-0.3, respectively. For all pebble sizes and size distributions the average and maximum normal contact forces slightly vary during the first cycles. The average normal contact force that the ceramic breeder material will experience is about 2.5 N for ACB and 0.65 N for EU Ref. however, the maximum normal contact force is about 8-9 times the average normal force in the assembly. Very few pebbles will undergo such maximum normal contact force, the majority of the pebbles experience a maximum normal contact force less than 5 times the average normal force (Figure 7-13). For monosized particles the maximum normal contact force is about 5-6 times the average normal force. However, only few monosized pebbles

experience a maximum normal contact force higher than 4 times the average normal force (Figure 7-13).

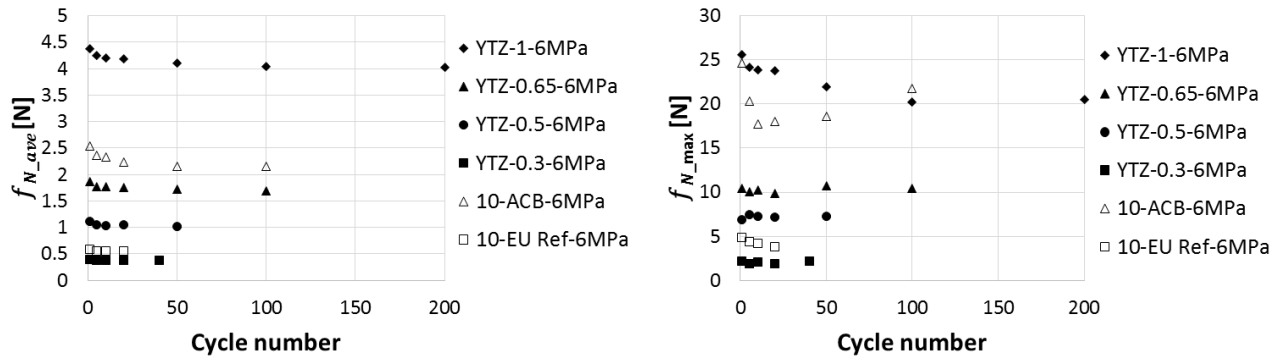


Figure 7-14: Evolution of the average (left) and maximum normal contact forces (right) for monosized and polydispersed assemblies as a function of the cycle number.

Figure 7-15 shows the dependence of the normalized mean and maximum normal forces on the compressive load. The mean and maximum normal forces are normalized with respect to d^2 , where d is the pebble diameter for the monosized assemblies and the average diameter of the distribution for polydispersed beds. In the figures the reported values refer to the 20th compressive cycle considering these values as representative for the long term behaviour of the bed (Figure 7-14). In Figure 7-15 the d^2 -normalized mean and maximum normal forces increase linearly with the compressive load (similar as in [74]-[75], [83]). The magnitude of the forces strongly reduces with the reduction of the pebble size (Figure 7-14). The reduction follows a square dependency as shown in Figure 7-15. The monosized and polydispersed assemblies show a consistent trend of the d^2 -normalized mean normal contact forces while the d^2 -normalized maximum normal forces trends slightly differ. The investigated assemblies do not show a dependency of the d^2 -normalized mean and maximum normal forces on the H/d ratio (very similar values are obtained for the investigated heights).

The mean normal force can be estimated by

$$f_{N_ave} = 0.702 d^2 \sigma \quad 7.1$$

where σ [MPa] is the uniaxial compressive load and d is the pebble diameter for the monosized assemblies or the average diameter for polydispersed beds. Equation 7.1 is plotted in Figure 7-15 as continuous line.

As already discussed above very few pebbles will undergo the maximum normal contact force reported in Figure 7-14 and Figure 7-15. Therefore, based on the study of the CDF of

$\langle F_{N_max} \rangle$ (Figure 7-13), if a very small amount of failing pebbles can be accepted, for design purposes the maximum normal force acting on the pebbles can be reasonably estimated as

$$f_{N_max} \leq 5 f_{N_ave} \quad \text{polydispersed EU. Ref and ACB pebbles,} \quad 7.2$$

$$f_{N_max} \leq 4 f_{N_ave} \quad \text{monosized pebbles.} \quad 7.3$$

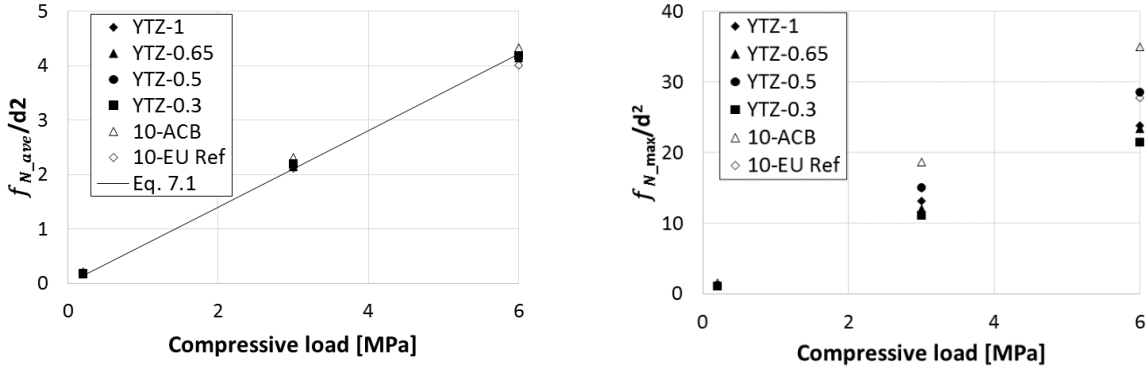


Figure 7-15: Mean (left) and maximum (right) normalized normal forces over the compressive load as a function of the compressive load.

7.4 Summary

UTC experiments and DEM simulations are aimed to investigate the effects of the pebble properties and the blanket operational parameters on the mechanical response of breeder beds subjected to cyclic loading. Polydispersed breeder ceramics and monosized commercial zirconia pebbles are used to study the influences of the pebble properties, the bed height and of the H/d ratio. In this study, the macroscale response has been presented together with the micro response at pebble scale. Good agreement is found between experiments and simulations. The KIT-DEM code is confirmed to be a reliable predictive tool for the study of the macro and micro-scale response of fusion breeder beds.

Regarding the macro scale response, the results show that monosized assemblies exhibit a stiffer response and a lower residual strain accumulation than polydispersed assemblies. Among the monosized assemblies the experimental and numerical results show a lower strain accumulation for bigger particles and thus an increase of the residual strain with the increase of the H/d ratio. For the extreme cases of YTZ-2 ($H/d=10$) numerical results reveal shake down after about 100 cycles. For polydispersed assemblies the influence of the bed height on their ratcheting behaviour is found to be modest. In particular, a slight reduction of the accumulated residual strain is observed for lower bed heights. The numerical simulations captured the

different macroscopic mechanical behaviours of monosized and polydispersed materials, consistent trends have been obtained in terms of stress-strain response and ratcheting behaviour by the two approaches.

Results for monosized assemblies show that increasing the H/d ratio (i.e. reducing the pebble diameter) the near wall regions dimension progressively reduce while the bulk zone dominates the packing structure of the assembly. However, for low H/d ratio ($H/d=10$) the bulk domain is not developed since the extinction length of the regular packing is comparable with the assembly height. On the other hand, for polydispersed beds the presence of the walls is found to barely influence the packing structure, the bulk zone dominates the packing structure of the assembly for all investigated assemblies' height. This suggest that, even for shallow breeder beds ($H=10$ mm) for the investigated size distributions, the mechanical and thermal behaviour of the assembly will be mainly governed by the bulk behaviour. On the contrary, if monosized particles are employed in breeder beds a low H/d ratio could influence the mechanical as well the thermal behaviour of the bed. For both polydispersed and monosized assemblies the CN increases during the first 10–20 cycles and it tends to saturate afterwards when a stable network of contacts is established. The evolution of the CN clearly shows that the major pebble rearrangements occur during the initial loading cycles. The magnitude of the CN slightly increases with both the reduction of the particle size and bed height. The PDF of the normalized normal forces and normalized maximum normal forces are unaffected by the mechanical cycling. While analogous distributions are obtained for the considered monosized pebbles, the shape of the PDFs for the polydispersed assemblies differs from those of monosized especially for the normalized maximum normal forces distribution. Among the polydispersed assemblies the probability distributions are found to be substantially unaffected by both the variation of the assembly height and size distributions. This results, for polydispersed assemblies, in a reduction of the number of contacts carrying a maximum normal force greater than the average. On the other hand, to keep the mechanical equilibrium, in the polydispersed assemblies more contacts will experience a maximum force greater than three times the average than in monosized assemblies. Even if subjected to a compressive load of 6MPa, the average normal contact force that the ceramic breeder material will experience is about 2.5 N for ACB and 0.65 N for EU Ref., while a realistic value of the maximum normal contact force is 4-5 times the average normal force.

Since the contact forces linearly increase with the compressive load acting on the bed, the reduction of the thermally induced stress peaks with cycling as reported in [66] is beneficial for the relaxation of the contact forces, the ratcheting of the bed and the crush probability of the breeder pebbles.

Chapter 8

Conclusions

In the frame of the design of the fusion breeder blanket component, the results obtained in this work contribute to the advancement of the breeding zone design broadening the knowledge on thermomechanical behaviour of ceramic breeder beds.

The thermal conductivity of ceramic breeder beds is investigated with a newly developed experimental facility based on the probe method. The thermal conductivity is studied under fusion relevant conditions, i.e. compressive load, high temperatures, helium gas at relevant pressures. Measurements are performed with the EU advanced and reference lithium orthosilicate material as well as with the advanced Japanese lithium metatitanate pebbles. The effective thermal conductivity is studied in the temperature range RT-700 °C. Experiments are performed in helium and air atmospheres in the pressure range 0.12-0.4 MPa at compressive load up to 6MPa with an initial packing factor of approx. 64% (consistent with the reference value of the actual EU breeding blanket design).

In agreement with previous studies the influence of the compressive load is found to be marginal. The increase of the effective thermal conductivity with the temperature is confirmed, though for all investigated pressures, a weaker temperature dependence is observed in comparison with literature values. Empirical correlations, derived from the experiments, are suggested for the calculation of the effective thermal conductivity of the studied pebble beds as a function of temperature in helium and air at 0.4, 0.2 and 0.12 MPa. The correlation proposed by Reimann [53] is currently used to estimate the thermal conductivity of breeder beds for the EU HCPB blanket design. Considering the experimental uncertainty, for temperatures above 300 °C the results in helium at 0.4 and 0.2 MPa are in good agreement with Reimann's correlation. However, the designer should validate the current blanket design with respect to the proposed correlations considering the uncertainty affecting them.

The experimental results show a clear influence of the solid material on the bed effective conductivity. The effective thermal conductivity of pure lithium metatitanate pebble beds is

observed to be approx. 20 % higher than that of the EU reference material. The thermal conductivity of the European advanced breeder material is found to be similar to that of the EU reference material. Among the investigated advanced compositions (namely 20, 25 and 30 mol % Li_2TiO_3 in Li_4SiO_4) there is no difference in terms of thermal conductivity. Hence, the selection of the optimal composition (i.e. metatitanate content) could not be based on the thermal conductivity. However, as shown by the experimental results, the solid phase in principle influences the thermal conductivity of a bed. Thus, further changes of the composition could improve the thermal performances of the breeder beds. The first indicator that reveals a possible beneficial influence of the breeder material on the bed effective conductivity is the thermal conductivity of the breeder material itself. Regarding the thermal properties, the future breeder materials should be first qualified from the thermal point of view to have an indication of the possible influence on the bed thermal conductivity.

The filling gas plays a major role in the heat transfer mechanism of a packed bed. The results show that in the accidental case of leakage in the breeding zone, associated with air ingress in the breeder beds, the effective thermal conductivity of the beds is severely reduced. Even if the reduction of the purge gas pressure is beneficial for the reduction of the tritium permeation in the coolant, it also reduces the effective thermal conductivity of the breeder beds. The breeder beds show a clear gas pressure dependence (due to the Smoluchowski effect) of the effective thermal conductivity in helium, while the pressure dependence is drastically reduced in air. The halving of the helium pressure from 0.4 to 0.2 MPa, results in a slight reduction (around 5%) of the effective thermal conductivity. While, the reduction of the helium pressure from 0.4 to 0.12 MPa leads to a reduction of the bed's effective thermal conductivity of about 10 %. The reduction of the thermal conductivity of the bed with the reduction of the gas pressure slightly increases with the temperature. For granular materials the pressure dependence of the effective thermal conductivity is intimately related to the gap between the particles which, in turn, depends on the packing factor and pebble size. A change of the pebble size or pebble size distribution can potentially modify the contribution of the gas phase on the heat transport in the breeder beds. For instance, binary beds with high packing factors could be more susceptible to the Smoluchowski effect than polydispersed beds. Thus, the gas pressure dependence should be assessed for a given size distribution/packing factor. With the current pebble size distribution, it is suggested to not reduce the purge gas pressure below 0.2 MPa to limit the Smoluchowski effect.

The mechanical response of bed assemblies subjected to cyclic compression is first investigated in a validation study and then extended with a dedicated experimental campaign. In both studies UCT experiments are conducted along with DEM numerical simulations. To provide representative results for the EU BB, blanket relevant conditions in terms of PF, pebble size and compressive load are used. These studies expand the very limited existing literature about the comparisons between DEM simulations and experiments. In both studies a good agreement is found between experiments and simulations. The KIT-DEM is confirmed to be a reliable predictive tool for the study of the macro and micro-scale response of fusion breeder beds.

Results of numerical simulations show that the pebble size distribution affects the stress-strain behaviour of the assemblies. Monosized assemblies show a stiffer response and a lower residual strain accumulation than polydispersed assemblies, while, for the same packing factor, a peaked size distribution leads to a lower residual strain after unloading in comparison with a broader size distribution. Among the investigated monosized assemblies the experimental and numerical results show an increase of the residual strain with the increase of the H/d ratio. For polydispersed assemblies the influence of the bed height on their ratcheting behaviour is marginal. The different mechanical response of the studied size distributions is ascribed to the different packing state for the same packing factor. The packing factor should be always referred to the maximum achievable packing factor relative to the size distribution. However, since the maximum achievable packing factor is not easy to identify, it is common practice to compare the results of different size distribution for the same packing factor. In the present study it is found that a peaked distribution results, for a given PF, in a denser configuration in comparison to a broader one.

The first cycles are responsible for the largest part of the irreversible residual strain. Afterwards, as the cycling proceeds, the compaction of the assembly is still progressing but with smaller increments. The maximum compressive load imposed on the bed affects the first 5 cycles. This means that increasing the imposed load leads to a higher irreversible strain during the first cycles as compared to a lower load. However, for the period following the first 5 cycles, the same rate of increase is reached for all investigated loads.

The micro mechanical results show that for monosized assemblies the increase of the H/d ratio (i.e. reducing the pebble diameter for a given bed height) leads to a reduction of the near

wall regions dimension while the bulk zone dominates the packing structure of the assembly. On the other hand, for polydispersed beds the presence of the walls barely influences the packing structure, the bulk zone dominates the packing structure of the assembly for all investigated assembly heights. This suggests that, even for shallow breeder beds ($H=10$ mm) for the investigated size distributions, the mechanical and thermal behaviour of the assembly will be mainly governed by the bulk behaviour. On the contrary, if monosized particles are employed in shallow breeder beds, the particle diameter should be varied accordingly towards a high H/d ratio to guarantee an isotropic and homogeneous response of the bed.

The study of the internal force distribution shows no influence of the mechanical cycling. Among the polydispersed assemblies the probability distributions are substantially unaffected by the both the variation of the assembly height and size distributions. The average normal contact force that the ceramic breeder material will experience is about 2.5 N for ACB and 0.65 N for EU Ref., while a realistic value of the maximum normal contact force is 4-5 times the average normal force. Correlations are proposed for the estimation of the average and maximum normal contact force as a function of the compressive load acting on the bed and of the pebble diameter.

References

- [1] <http://www.iter.org> (October 10, 2016)
- [2] G. Janeschitz, Lecture: “ITER the Way to Fusion Energy”, Austrian ITER Information Day Wien 20/05/2015.
- [3] F. Cismondi, Lecture: “Basics of breeding blanket technology”, 5th Karlsruhe International School on Fusion Technologies 2011.
- [4] <http://www.ipp.mpg.de> (October 12, 2016)
- [5] L. M. Giancarli et al., “Progress and challenges of the ITER TBM Program from the IO perspective”, *Fusion Engineering and Design* 109–111 (2016) 1491–1497.
- [6] J.G. van der Laan, A.V. Fedorov, S. van Til, J. Reimann, “Ceramic Breeder Materials”, *Reference Module in Materials Science and Materials Engineering, 2016, Current as of 28 October 2015*, <http://dx.doi.org/10.1016/B978-0-12-803581-8.00733-5>
- [7] N. Roux, S. Tanaka, C. Johnson, R. Verrall, “Ceramic breeder material development”, *Fusion Engineering and Design* 41 (1998) 31–38.
- [8] R. Knitter, P. Chaudhuri, Y.J. Feng, T. Hoshino, I.-K. Yu, “Recent developments of solid breeder fabrication”, *Journal of Nuclear Materials* 442 (2013) S420–S424.
- [9] M. Zmitko et al., “Development and qualification of functional materials for the EU Test Blanket Modules: Strategy and R&D activities”, *Journal of Nuclear Materials* 417 (2011) 678–683.
- [10] R. Knitter, B. Löbbecke, “Reprocessing of Lithium Orthosilicate Breeder Material by Remelting”, *Journal of Nuclear Materials* 361 (2007) 104–111.
- [11] O. Leys, T. Bergfeldt, M. H. H. Kolb, R. Knitter, A. A. Goraieb, “The reprocessing of advanced mixed lithium orthosilicate/metatitanate tritium breeder pebbles”, *Fusion Engineering and Design* 107 (2016) 70–74.
- [12] W. Pannhorst, V. Geiler, G. Rake, B. Speit, D. Sprenger, “Production Process of Lithium Orthosilicate Pebbles”, *Fusion Tech. 1998, Proceedings of 20th Symposium on Fusion Technology, Sept. 7-11, 1998, Marseille, France*, B. Beaumont, P. Libeyre, B. de Gentile, G. Tonon (Eds.), Vol. 2, 1441–1444.
- [13] R. Knitter, B. Alm, G. Roth, “Crystallisation and Microstructure of Lithium Orthosilicate Pebbles”, *Journal of Nuclear Materials* 367–370 (2007) 1387–1392.
- [14] M. Kolb, R. Knitter, U. Kaufmann, D. Mundt, “Enhanced fabrication process for lithium orthosilicate pebbles as breeding material”, *Fusion Engineering and Design* 86 (2011) 2148–2151.
- [15] R. Knitter, M.H.H. Kolb, U. Kaufmann, A. A. Goraieb, “Fabrication of modified lithium orthosilicate pebbles by additions of titania”, *Journal of Nuclear Materials* 442 (2013) 433–436.

- [16] J. Reimann, D. Ericher, G. Wörner, “Influence of pebble bed dimensions and filling factor on mechanical pebble bed properties’, *Fusion Engineering and Design* 69 (1–4) (2003) 241–244.
- [17] A. Abou Sena, A. Ying, M. Abdou, “Effective thermal conductivity of lithium ceramic pebble beds for fusion blankets: a review”, *Fusion Tech.* 47(2005) 1094–1100.
- [18] M. Smoluchowski, "Über den Temperatursprung bei Wärmeleitung in Gasen" *Pisma Mariana Smoluchowskiego* 1.1 (1924) 113-138.
- [19] K. Raed, “Investigation of Knudsen and gas-atmosphere effects on effective thermal conductivity of porous media”, Ph.D. thesis, Faculty of Mechanical, Process and Energy Engineering, Technische Universität Bergakademie Freiberg, 2013.
- [20] M. G. Kaganer, “Thermal insulation in cryogenic engineering”, Israel Program for Scientific Translations, Jerusalem, 1969.
- [21] B. Baule, “Theoretische behandlung der erscheinungen in verduennten gasen”, *Annalen der Physik*, 44, 145-176, 1914.
- [22] F. O. Goodman, “Thermal accommodation coefficients”, *The Journal of Physical Chemistry*, 84, 1431-1445, 1980.
- [23] N. Wakao and S. Kagnei, “Heat and mass transfer in packed beds”, Gordon and Breach, New York, 1982.
- [24] Fourier, J. B. J., *Théorie Analytique de la Chaleur*, F. Didot, Paris, 1822.
- [25] *ASTM Standard*, Standard Test Method for Thermal Conductivity of Solids Using the Guarded- Comparative-Longitudinal Heat Flow Technique, Designation: E1225 – 13.
- [26] *ASTM Standard*, Standard Test Method for Evaluating the Resistance to Thermal Transmission of Materials by the Guarded Heat Flow Meter Technique, Designation: E1530 – 11.
- [27] *ASTM Standard*, Standard Test Method for Steady-State Heat Flux Measurements and Thermal Transmission Properties by Means of the Guarded-Hot-Plate Apparatus, Designation: C177 – 13.
- [28] *ASTM Standard*, Standard Practice for Using a Guarded-Hot-Plate Apparatus or Thin-Heater Apparatus in the Single-Sided Mode, Designation: C1044 – 12.
- [29] K. D. Maglic, A. Cezairliyan & V. Peletsky, *Compendium of Thermophysical Property Measurement Methods*, Vol 1, Plenum Press, New York, 1984, pp.61-122.
- [30] Hot Disk AB, <http://www.hotdiskinstruments.com/> (November 10, 2016)
- [31] C-Therm Technologies Ltd, <http://ctherm.com/> (November 10, 2016)
- [32] Hukseflux Thermal Sensors B.V, <http://www.hukseflux.com/> (November 10, 2016)
- [33] Decagon Devices Inc., <http://www.decagon.com/> (November 10, 2016)
- [34] *ASTM Standard*, Standard Test Method for Thermal Diffusivity by the Flash Method, Designation: E1461 – 13.
- [35] H. S Carslaw and J. C. Jaeger, “Conduction Of Heat In Solids”, 2nd ed. Oxford U.P., Oxford (1959), pp. 256-261.
- [36] B. W. Jones, “Thermal conductivity probe: development of method and application to a coarse granular medium”, *J. Phys. E: Sci. Instrum.* 21 (1988) 832-839.

- [37] J. H Blackwell, "The axial flow error in the thermal conductivity probe", *Can. J. Phys.* 34, (1956), 412.
- [38] A. A. Clifford, J. Kestin, W. A. Wakeham, "A Further Contribution To The Theory Of The Transient Hot-Wire Technique For Thermal Conductivity Measurements", *Physica* 100A (1980) 370-374.
- [39] E. G. Murakami, V. E. Sweat, S. K. Sastry, E. Kolbe, "Analysis Of Various Design And Operating Parameters Of The Thermal Conductivity Probe", *Journal of Food Engineering* 30 (1996) 209-225.
- [40] J. W. Haarman, "A Contribution to the Theory of the Transient Hot-Wire Method", *Physica* 52 (1971) 605-6Fbl19.
- [41] J. J. Healy, J. J. De Groot, J. Kestin, "The Theory of the Transient Hot-Wire Method for Measuring Thermal Conductivity", *Physica* 82C (1976) 392-408.
- [42] P. G. Knibbe, "The end-effect error in the determination of thermal conductivity using a hot-wire apparatus", *Int. J. Heat Mass Transfer*. Vol. 29, No. 3, pp. 463-473, 1986.
- [43] M. Dalle Donne, G. Sordon, "Heat Transfer in Pebble Beds For Fusion Blankets", *Fusion Tech.*, 17, (1990).
- [44] J. Sullivan, C.L. Brayman, R.A. Verrall, J.M. Miller, P.J. Gierszewski, F. Londry, A. Slavin, "Canadian ceramic breeder sphere technology-capability and recent results", *Fusion Engineering and Design* 17 (1991) 79-85.
- [45] R. O. A. Hall, D. G. Martin, "The thermal conductivity of powder beds. a model, some measurements on UO₂, vibro-compacted microspheres, and their correlation", *Journal of Nuclear Materials* 101 (1981) 172-183.
- [46] M. Enoda, S. Satoh, T. Kurasawa, H. Takatsu, "Measurement of Effective Conductivity of Lithium Oxide & Beryllium Packed Bed", *IEEE*, 282, (1994).
- [47] M. Dalle Donne, A. Goraieb, R. Huber, B. Schmitt, G. Schumacher, G. Sordon, A. Weisenburger, "Heat Transfer and Technological Investigations on Mixed Beds of Beryllium and Li₄SiO₄ pebbles", *Journal of Nuclear Materials* 212, (1994).
- [48] P. Gierszewski, H. Hamilton, J. Miller, J. Sullivan, R. Verrall, J. Earnshaw, D. Ruth, R. Macauley-Newcombe, G. Williams, "Canadian ceramic breeder technology: recent results", *Fusion Engineering and Design* 27 (1995) 297-306.
- [49] J. Earnshaw, F. Londry, P. Gierszewski, "The Effective Thermal Conductivity of Bed of 1.2mm Lithium Zirconate Spheres in Helium", *Fusion Tech.*, 33, (1998).
- [50] M. Dalle Donne, A. Goraieb, G. Piazza, G. Sordon, "Measurements of the effective thermal conductivity of Li₄SiO₄ pebble bed", *Fusion Engineering and Design* 49 (2000).
- [51] M. Enoda, Y. Ohara, N. Roux, A. Ying, G. Piazza, S. Malang, "Effective Thermal Conductivity Measurement of the Candidate Ceramic Breeder Pebble Beds by the Hot Wire Method", *Fusion Tech.*, 39, 612, (2001).
- [52] R. Bauer, E. U. Schlunder, "Effective Radial Thermal Conductivity of Packings in Gas Flow. Part II. Thermal Conductivity of the Packing Fraction without Gas Flow", *Int. Chem. Eng.*, **18**, 189(1978)

- [53] J. Reimann, S. Hermsmeyer, “Thermal conductivity of compressed ceramic breeder pebble beds”, *Fusion Engineering and Design* 61-62 (2002) 345-351
- [54] T. Hatano, M. Enoeda, S. Suzuki, Y. Kosaku, M. Akiba, “Effective Thermal Conductivity of a Li_2TiO_3 Pebble Bed for a Demo Blanket”, *Fusion Tech.* vol. 44 (2003).
- [55] H. Tanigawa, T. Hatano, M. Enoeda, M. Akiba, “Effective thermal conductivity of a compressed Li_2TiO_3 pebble bed”, *Fusion Engineering and Design* 75-79 (2005) 801–805.
- [56] A. Abou Sena, A. Ying, M. Abdou, “Experimental measurements of the effective thermal conductivity of a lithium titanate (Li_2TiO_3) pebbles-packed bed”, *Journal of Materials Processing Technology* 181 (2007) 206–212.
- [57] Y. Feng, K. Feng, Y. Liu, B. Gong, Y. Cheng, “Experimental Investigation of Thermal Properties of the Li_4SiO_4 Pebble Beds”, *J. Plasma Fusion Res. SERIES*, Vol. 11 (2015)
- [58] Alice Ying et al., “Status of ceramic breeder pebble bed thermomechanics R&D and impact on breeder material mechanical strength”, *Fusion Engineering and Design* 87 (2012) 1130–1137.
- [59] A. Ying, Z. Lu, M. Abdou, “Mechanical behavior and design database of packed beds for blanket designs”, *Fusion Engineering and Design* 39–40 (1998) 759–764.
- [60] Z. Lu, A. Ying, M. Abdou, “Numerical and experimental prediction of the thermomechanical performance of pebble beds for solid breeder blanket”, *Fusion Engineering and Design* 49–50 (2000) 605–611.
- [61] J. Reimann, G. Wörner, “Thermal creep of Li_4SiO_4 pebble beds”, *Fusion Engineering and Design* 58 (59) (2001) 647–651.
- [62] G. Piazza, J. Reimann, E. Günther, R. Knitter, N. Roux, J.D. Lulewicz, “Characterisation of ceramic breeder materials for the helium cooled pebble bed blanket”, *Journal of Nuclear Materials* 307–311 (Part 1(0)) (2002) 811–816.
- [63] J. Reimann, L. Boccaccini, M. Enoeda, A. Ying, “Thermomechanics of solid breeder and be pebble bed materials”, *Fusion Engineering and Design* 61–62 (2002) 319–331.
- [64] L. Bühler, J. Reimann, “Thermal creep of granular breeder materials in fusion blankets”, *Journal of Nuclear Materials* 307–311 (2002) 807–810.
- [65] J. Reimann, H. Harsch, “Thermal creep of beryllium pebble beds”, *Fusion Engineering and Design* 75–79 (2005) 1043–1047.
- [66] C. S. Zhang, A. Ying, M. A. Abdou, Y. Park, “Ceramic breeder pebble bed packing stability under cyclic loads”, *Fusion Engineering and Design* (2016), <http://dx.doi.org/10.1016/j.fusengdes.2016.03.014>
- [67] G. Dell’Orco, P.A. Di Maio, R. Giammusso, A. Malavasi, L. Sansone, A. Tincani, G. Vella, “Progress in the benchmark exercise for analyzing the lithiate breeder pebble bed thermo-mechanical behaviour”, *Fusion Engineering and Design* 81 (2006) 169–174.
- [68] P. A. Cundall, O. D. L. Strack, “A discrete numerical model for granular assemblies”, *Geotechnique*, 29(1):47–65, 1979.
- [69] A. Ying, H. Huang, M. A. Abdou, “Numerical simulation of ceramic breeder pebble bed thermal creep behavior”, *Journal of Nuclear Materials* 307–311 (2002) 827–831.

- [70] Z. An, A. Ying, M. Abdou, “Application of discrete element method to study mechanical behaviors of ceramic breeder pebble beds”, *Fusion Engineering and Design* 82 (2007) 2233–2238.
- [71] Z. An, A. Ying, M. Abdou, “Numerical characterization of thermo-mechanical performance of breeder pebble beds”, *Journal of Nuclear Materials* 367–370 (2007) 1393–1397.
- [72] J. T. Van Lew, Y. Park, A. Ying, M. Abdou, “Modifying Young’s modulus in DEM simulations based on distributions of experimental measurements”, *Fusion Engineering and Design* 98–99 (2015) 1893–1897.
- [73] J.T. Van Lew, A. Ying, M. Abdou, “A discrete element method study on the evolution of thermomechanics of a pebble bed experiencing pebble failure”, *Fusion Engineering and Design* 89 (2014) 1151–1157.
- [74] Y. Gan, M. Kamlah, “Discrete element modelling of pebble beds: With application to uniaxial compression tests of ceramic breeder pebble beds”, *J. Mech. Phys. Solids* 58 (2010) 129–144.
- [75] R. K. Annabattula, Y. Gan, M. Kamlah, “Mechanics of binary and polydispersed spherical pebble assembly”, *Fusion Engineering and Design* 87 (2012) 853–858.
- [76] S. Zhao, Y. Gan, M. Kamlah, T. Kennerknecht, R. Rolli, “Influence of plate material on the contact strength of Li_4SiO_4 pebbles in crush tests and evaluation of the contact strength in pebble–pebble contact”, *Engineering Fracture Mechanics* 100 (2013) 28–37.
- [77] S. Zhao, Y. Gan, M. Kamlah, “Failure initiation and propagation of Li_4SiO_4 pebbles in fusion blankets”, *Fusion Engineering and Design* 88 (2013) 8–16.
- [78] R. K. Annabattula, Y. Gan, S. Zhao, M. Kamlah, “Mechanics of a crushable pebble assembly using discrete element method”, *Journal of Nuclear Materials* 430 (2012) 90–95.
- [79] M. Moscardini, Y. Gan, R. K. Annabattula, M. Kamlah, “A Discrete Element Method to simulate the mechanical behavior of ellipsoidal particles for a fusion breeding blanket”, *Fusion Engineering and Design* 121 (2017) 22–31.
- [80] W. S. Jodrey, E. M. Tory, “Computer simulation of close random packing of equal spheres”, *Phys. Rev. A* 32 (4) (1985) 2347–2351.
- [81] X. Wang, M. Ye, H. Chen, “Computational study on the behaviors of granular materials under mechanical cycling”, *J. Appl. Phys.* 118, 174901 (2015).
- [82] H. Zhang, H. Guo, M. Ye, Z. Li, H. Huang, “Investigation on the packing behaviors and mechanics of Li_4SiO_4 pebble beds by discrete element method”, *Fusion Engineering and Design* (2017), <http://dx.doi.org/10.1016/j.fusengdes.2017.04.049>
- [83] H. Zhang, H. Guo, T. Shi, M. Ye, H. Huang, Z. Li, “Cyclic loading tests on ceramic breeder pebble bed by discrete element modelling”, *Fusion Engineering and Design* 118 (2017) 40–44.
- [84] M. Panchal, P. Chaudhuri, J. T. Van Lew, A. Ying, “Numerical modelling for the effective thermal conductivity of lithium meta titanate pebble bed with different packing structures”, *Fusion Engineering and Design* 112 (2016) 303–310.

- [85] L. Chen, Y. Chen, K. Huang, S. Liu, “Investigation of effective thermal conductivity for pebble beds by one-way coupled CFD-DEM method for CFETR WCCB”, *Fusion Engineering and Design* 106 (2016) 1–8.
- [86] J. T. Van Lew, A. Ying, M. Abdou, “Numerical study on influences of bed resettling, breeding zone orientation, and purge gas on temperatures in solid breeders”, *Fusion Engineering and Design* 109–111 (2016) 539–544.
- [87] J. T. Van Lew, A. Ying, M. Abdou, “A discrete element method study on the evolution of thermomechanics of a pebble bed experiencing pebble failure”, *Fusion Engineering and Design* 89 (2014) 1151–1157.
- [88] Y. Gan, F. Hernandez, D. Hanaor, R. Annabattula, M. Kamlah, P. Pereslavitsev, “A thermal discrete element analysis of EU solid breeder blanket subjected to neutron irradiation”, *Fusion Science and Technology*, DOI: 10.13182/FST13-727.
- [89] S. Papeschi, R. Knitter, M. Kamlah, “Effective thermal conductivity of advanced ceramic breeder pebble beds”, *Fusion Engineering and Design* 116 (2017) 73–80.
- [90] Corning Incorporated, <http://www.corning.com> (February 20, 2014)
- [91] J. H. Blackwell, “A Transient-Flow Method for Determination of Thermal Constants of Insulating Materials in Bulk Part I—Theory”, *J. of Appl. Phys.* 25, 137 (1954); doi: 10.1063/1.1721592.
- [92] P. Andersson, G. Bäckström, “Thermal conductivity of solids under pressure by the transient hot wire method”, *Review of Scientific Instruments* 47, 205 (1976); doi: 10.1063/1.1134581.
- [93] J. Fokkens, “Thermo-Mechanical Finite Element Analyses for the HCPB In-Pile Test Element”, NRG Report 21477/02.50560/I; Jan. 2003.
- [94] J. Reimann, R. Knitter, G. Piazza, New Compilation of the Material Data Base and the Material Assessment Report, EFDA reference: TW5-TTBB-006-D2 (2005)
- [95] <http://www.specialmetals.com/assets/smc/documents/alloys/inconel/inconel-alloy-600.pdf> (September 3, 2014)
- [96] <http://www-ferp.ucsd.edu/LIB/PROPS/PANOS/al2o3.html> (September 3, 2014)
- [97] <http://kanthal.com/en/products/material-datasheets/wire/resistance-heating-wire-and-resistance-wire/kanthal-a-1/> (September 3, 2014)
- [98] https://www.corning.com/media/worldwide/csm/documents/71759a443535431395eb34eb_ead091cb.pdf (September 3, 2014)
- [99] JCGM 100-2008, “Evaluation of measurement data – Guide to the expression of uncertainty in measurement”.
- [100] ASTM Standard, “Standard Test Method for Determination of Thermal Conductivity of Soil and Soft Rock by Thermal Needle Probe Procedure” Designation: D 5334 – 08.
- [101] J. G. Hust, D. R. Smith, “Interlaboratory Comparison of Two Types of Line-Source Thermal Conductivity Apparatus Measuring Five Insulating Materials,” NISTIR, 89-3908, 1989.

- [102] T. Hoshino, Y. Edao, Y. Kawamura, K. Ochiai, “Pebble fabrication and tritium release properties of an advanced tritium breeder”, *Fusion Engineering and Design* 109–111 (2016) 1114–1118.
- [103] T. Hoshino, M. Nakamichi, “Development of fabrication technologies for advanced breeding functional materials For DEMO reactors”, *Fusion Engineering and Design* 87 (2012) 486–492.
- [104] B. Löbbecke, R. Knitter, M. Rohde, J. Reimann, “Thermal conductivity of sintered lithium orthosilicate compacts”, *Journal of Nuclear Materials* 386–388 (2009) 1068–1070.
- [105] P. Gierszewski, “Review of properties of lithium metatitanate”, *Fusion Engineering and Design* 39–40 (1998) 739–743.
- [106] S. Saito, K. Tsuchiya, H. Kawamura, T. Terai, S. Tanaka, “Density Dependence on Thermal Properties of Li₂TiO₃ Pellets”, *Journal of Nuclear Materials* **253**, 213, (1998).
- [107] T. Hoshino, M. Dokiya, T. Terai, Y. Takahashi, M. Yamawaki, “Non-stoichiometry and its effect on thermal properties of Li₂TiO₃”, *Fusion Engineering and Design* 61_ 62 (2002) 353-360.
- [108] P. Jain, S. Saxena, “Transport Properties of Helium in Temperature 400-2300K”, *Chem. Phy. Letters*, 36, (1975).
- [109] The Engineering ToolBox, http://www.engineeringtoolbox.com/dry-air-properties-d_973.html (March 22, 2016)
- [110] S. Pupeschi, R. Knitter, M. Kamlah, Y. Gan, “Numerical and experimental characterization of ceramic pebble beds under cycling mechanical loading”, *Fusion Engineering and Design* 112 (2016) 162–168.
- [111] Y. Gan, M. Kamlah, J. Reimann, “Computer simulation of packing structure in pebble beds”, *Fusion Engineering and Design* 85 (2010) 1782–1787.
- [112] C. T. David, R. García-Rojo, H. J. Herrmann, S. Luding, “Hysteresis and creep in powders and grains”, proceeding of the 5th international conference on micromechanics of granular media, Stuttgart, Germany, 18-22 July, 2005.
- [113] <http://www.tosoh.com/> (December 8, 2016)
- [114] T. Aste, “Variations around disordered close packing”, *J. Phys.: Condens. Matter* 17 (2005) S2361–S2390
- [115] A. Lorenz, C. Tuozzolo, M.Y. Louge, “Measurements of impact properties of small, nearly spherical particles,” *Experimental Mechanics* Vol. 37, No. 3, (1997), pp. 292 – 298.
- [116] <http://www.tosoh.com/our-products/advanced-materials/zirconia-grinding-dispersion-media> (December 8, 2016)
- [117] Y.X. Gan, M. Kamlah, “Thermo-mechanical modelling of pebble bed–wall interfaces”, *Fusion Engineering and Design* 85 (1) (2010) 24–32.
- [118] J. Reimann, R. A. Pieritz, C. Ferrero, M. Di Michiel, R. Rolli, “X-ray tomography investigations on pebble bed structures”, *Fusion Engineering and Design* 83 (7–9) (2008) 1326–1330.

- [119] David R. Lide, CRC Handbook of Chemistry and Physics, 95th Edition, CRC Press, June 29, 2004.

Appendix A

Properties of helium and air

	Helium	Air	Li ₄ SiO ₄
m_g [amu]	4	28.96	/
m_s [amu]	/	/	119.85
d_m [m] [119]	$2.15 \cdot 10^{-10}$	$3.66 \cdot 10^{-10}$	/
$k_0(27^\circ\text{C})$ [W/(m K)]	0.15 [108]	0.026 [109]	2.56 [104] - 4.14 [43]

Thermal conductivity of unconfined air [109]:

T [°C]	k air [W/(m K)]
27	0.02624
52	0.02816
77	0.03003
102	0.03186
127	0.03365
177	0.0371
227	0.04041
277	0.04357
327	0.04661
377	0.04954
427	0.05236
477	0.05509
527	0.05774
577	0.0603
627	0.06276
677	0.0652

Thermal conductivity of unconfined helium [108]:

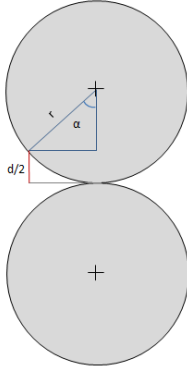
$$K = 0.55 + 3.353 \cdot 10^{-3} T(K) - 2.117 \cdot 10^{-7} T^2 - 6.626 \cdot 10^{-11} T^3 \text{ [mW/(cm K)] with } T(K)$$

Appendix B

Estimation of the gap size

The evaluation of the mean gap size \bar{d} based on the some basic contact schemes is reported hereafter. Some representative values are listed at the end of this appendix.

CASE 1: Two particles of equal radius (r)

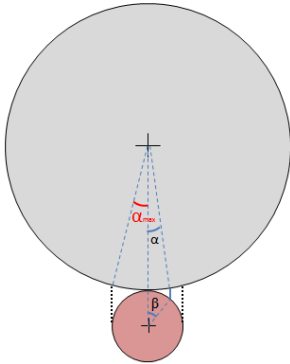


$$d = 2 r (1 - \cos \alpha)$$

$$0 < \alpha < \pi/2$$

$$\bar{d} = 2 \frac{\int_0^{\pi/2} r (1 - \cos \alpha) d\alpha}{\int_0^{\pi/2} d\alpha}$$

CASE 2: Two particles of different radii (r_b, r_s) $r_b > r_s$



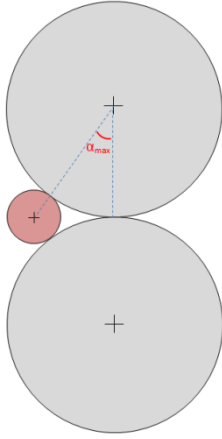
$$d = r_b (1 - \cos \alpha) + r_s (1 - \cos \beta)$$

$$0 < \alpha < \alpha_{max}; 0 < \beta < \pi/2$$

$$\alpha_{max} = \sin^{-1}(r_s/r_b)$$

$$\bar{d} = \frac{\int_0^{\alpha_{max}} r_b (1 - \cos \alpha) d\alpha}{\int_0^{\alpha_{max}} d\alpha} + \frac{\int_0^{\pi/2} r_s (1 - \cos \beta) d\beta}{\int_0^{\pi/2} d\beta}$$

CASE 3: Two contacting particles of equal radius (r_b) in contact with a third particle of smaller radius (r_s)



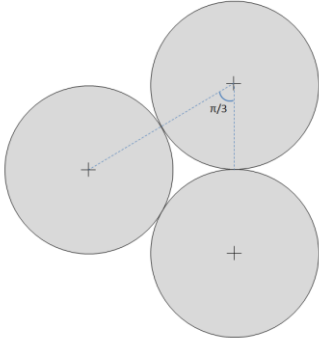
$$d = 2 r_b (1 - \cos \alpha)$$

$$0 < \alpha < \alpha_{max}$$

$$\alpha_{max} = \cos^{-1} \left(\frac{r_b}{r_b + r_s} \right)$$

$$\bar{d} = 2 \frac{\int_0^{\alpha_{max}} r_b (1 - \cos \alpha) d\alpha}{\int_0^{\alpha_{max}} d\alpha}$$

CASE 4: Three contacting particles of equal radius (r_b)

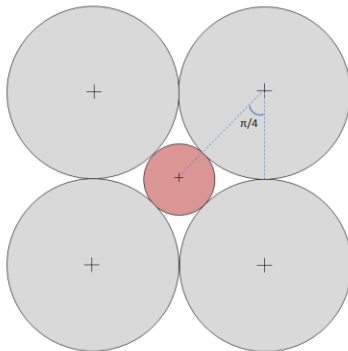


$$d = 2 r_b (1 - \cos \alpha)$$

$$0 < \alpha < \pi/3$$

$$\bar{d} = 2 \frac{\int_0^{\pi/3} r_b (1 - \cos \alpha) d\alpha}{\int_0^{\pi/3} d\alpha}$$

CASE 5: Four contacting particles of equal radius (r_b) in contact with a fifth particle of smaller radius (r_s) in between

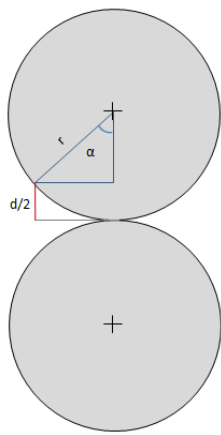
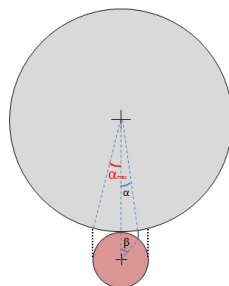
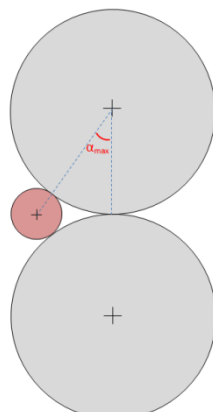


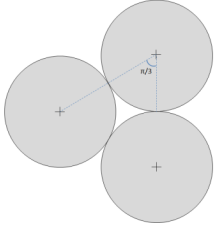
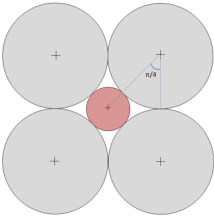
$$d = 2 r_b (1 - \cos \alpha)$$

$$0 < \alpha < \pi/4$$

$$r_s = \sqrt{2 r_b^2} - r_b$$

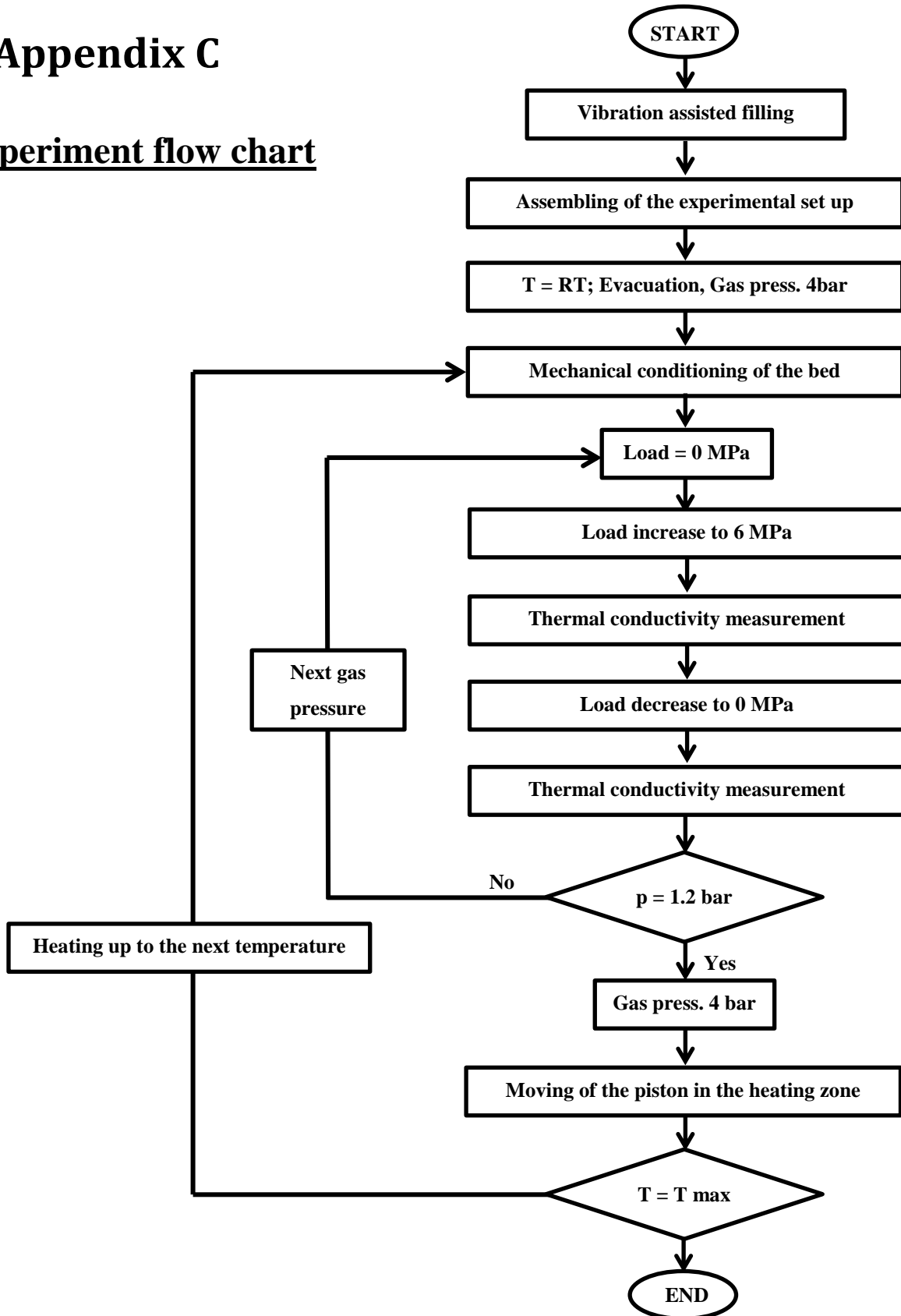
$$\bar{d} = 2 \frac{\int_0^{\pi/4} r_b (1 - \cos \alpha) d\alpha}{\int_0^{\pi/4} d\alpha}$$

Case	r_b [mm]	r_s [mm]	d_b [mm]	d_s [mm]	\bar{d} [μm]
	0.625		1.25		454
	0.325		0.65		236
	0.125		0.25		91
	0.175	0.125	0.35	0.25	63
	0.25		0.5		57
	0.325		0.65		54
	0.4		0.8		52
	0.475		0.95		51
	0.55		1.1		50
	0.625	0.125	1.25	0.25	50
		0.25		0.5	108
		0.375		0.75	179
		0.5		1	267
	0.625	0.125	1.25	0.25	70
		0.25		0.5	121
		0.375		0.75	161
		0.5		1	191
	0.5	0.125	1	0.25	68
	0.375		0.75		64
	0.25		0.5		57

Case	r_b	r_s	d_b	d_s	\bar{d}
	[mm]	[mm]	[mm]	[mm]	[μm]
	0.125		0.25		43
	0.25		0.5		87
	0.375		0.75		130
	0.5		1		173
	0.625		1.25		216
	0.325	0.13	0.65	0.26	65
	0.4	0.17	0.8	0.34	80
	0.475	0.20	0.95	0.4	95
	0.55	0.23	1.1	0.46	110
	0.625	0.26	1.25	0.52	125

Appendix C

Experiment flow chart



Appendix D

Properties of Li_4SiO_4

The simulations have been conducted with a bed density of 1500 $[\text{Kg}/\text{m}^3]$. The material properties of lithium orthosilicate, hereafter reported, are taken from [93].

T [°C]	<i>k</i> [W/(m °C)]	C_p [J/(Kg °C)]
0	0.768	1392.38
50	0.793	1450.02
100	0.818	1513.4
150	0.842	1579.99
200	0.867	1648.5
250	0.892	1718.24
300	0.917	1788.79
350	0.941	1859.91
400	0.966	1931.43
450	0.991	2003.25
500	1.016	2075.29
550	1.041	2147.5
600	1.065	2219.84
650	1.09	2292.29
700	1.115	2364.82
750	1.14	2437.41
800	1.165	2510.06
850	1.189	2582.76
900	1.214	2655.49
950	1.239	2728.26
1000	1.264	2801.05

Appendix E

Thermal probe properties

The probe is simulated as one body having the averaged thermal properties according to the volume fraction of the constituent components. For the property P , this means

$$\bar{P} = \frac{\sum_{i=1}^n w_i P_i}{\sum_{i=1}^n w_i},$$

where \bar{P} is the average thermal property and w_i is the weight factor. The weight factors are obtained by dividing the total volume by the volume occupied by the single component. The weight factors and the thermal properties [95]-[97] are listed hereafter.

	Clad	Aluminium Oxide	Thermocouple / heating element
Weight factor	0.56	0.40	0.04

Thermal probe averaged properties

T [°C]	k [W/m °C]	T [°C]	C_p [J/Kg °C]	T [°C]	ρ [Kg/m ³]
20	23.97	20	579.07	20	6567
83	21.37	133	645.26	800	6567
200	18.71	200	703.60		
300	17.49	333	747.76		
400	16.82	400	779.30		
500	16.68	533	808.49		
600	17.80	600	842.24		
800	19.13	800	873.64		

Acknowledgements

First of all I would like to express my sincere gratitude to my advisors Prof. Marc Kamlah and Dr. Regina Knitter for their valuable support, motivation and guidance through my PhD. I am gratefully indebted to them for their continued trust and for the freedom they afforded me to conduct the research.

Besides my advisors, I would like to gratefully acknowledge Prof. Robert Stieglitz for his careful revision of the thesis that greatly improved the manuscript.

I am also really grateful to my colleagues Julia Heuser, Matthias Kolb, Oliver Leys, Keisuke Mukai and Christina Odemer for their feedback, stimulating discussions, cooperation and of course friendship. Moreover, I would like to thank Dr. Fabio Cismondi, Dr. Francisco Alberto Hernández González and Dr. Jörg Reimann for their valuable help and suggestions. In addition, I would like to express my gratitude to all the staff of the IAM-KWT. I count myself lucky working in a department where employees care so much for one another; I really appreciate all the good times we shared together.

I want to express my gratitude to Dr. Yixiang Gan who provided me the opportunity to join his research group at School of Civil Engineering of the University of Sydney. I am thankful to Yixiang for his patience and the countless insightful discussion we had.

I would like to also thank the KIT-TEC and the INR workshop, in the persons of Mr. Joachim Konrad, Mr. Daniel Kuntz, Mr. Oliver Albrecht and Mr. Lukas Sic for their excellent work in the construction of the experimental apparatus.

I am deeply thankful to my wife, Marigrazia Moscardini, the role you have been playing in my life is immense. Thank you for caring me wholeheartedly, thanks for your patience and unconditional support along the way. Thanks for the fruitful technical discussions and to encouraging me to pursue this doctoral work.

Thanks to my friends for all the fun we have had in the last years. Finally, a special thank goes to my family, my parents and my sister, for their continuous support and love.